Universitat Autònoma de Barcelona

High-quality CVD graphene for spintronic applications

Zewdu Messele Gebeyehu

High-quality CVD graphene

for spintronic applications

Doctoral thesis in chemistry

Zewdu Messele Gebeyehu

Supervised by: Sergio O. Valenzuela

Maria J. Esplandiu

Marius V. Costache

Tutor: Josep R. Badosa

Catalan Institute of Nanoscience and Nanotechnology (ICN2)

December, 2019

Preface

This thesis has been written as a partial fulfillment of the requirements for obtaining the Ph.D. degree in chemistry in the period from March 2015 to November 2019 at the Catalan Institute of Nanoscience and Nanotechnology (ICN2) , Universitat Autonoma de Bercelona (UAB), Barcelona, Spain. The project has been carried out in the Physics and Engineering of Nanodevice group and has been supervised by the following people: ICREA Professor Ph.D. Sergio O. Valenzuela, CSIC Tenured Scientist Ph.D. Maria Jose Esplandiu and Senior Researcher Ph.D. Marius V. Costache.

This thesis encompasses optimization of growth conditions for CVD graphene, nucleation density reduction using a photocatalysis-assisted annealing, and characterization of graphene using microscopic, spectroscopic, electrical and spintronic techniques. The results are mostly based on the published papers and some other unpublished preliminary results.

Abstract

This thesis has focused on tuning the synthesis and processing of graphene to achieve optimized spintronic applications. Thus the thesis is framed in two cut-edging topics: the graphene world with its richness of unique properties and the field of spintronics which explores the spin degree of freedom of the electrons for novel applications in information and communication technology (e.g. information storage and logic devices). Under this context graphene is a very promising spin channel material to transport spin with long spin diffusion lengths. To accomplish that, a high quality-graphene with minimum electron scattering centers is a key parameter and must be ensured from the moment of its production and during its processing. Accordingly, in this thesis, a lot of efforts have been invested to fine-tune the growth parameters of graphene by chemical vapor deposition (CVD). Several relevant contributions in the field have been achieved:

- THE DEMONSTRATION of the importance of the graphene etching backreaction during growth which begins to dominate at long growth times due to an in-situ increase of hydrogen concentration. That is a phenomenon that has been previously ignored but very important to consider since it impacts on the graphene domain reshaping. A thorough characterization of the graphene domain shape evolution has been accomplished by tuning the growth time, the flow of gas precursors and the catalyst confinement which allows better identifying the onset of the etching process. Controlling this effect is very

relevant to minimize structural defects induced by etching which can impact the electron/spin transport.

- THE INTRODUCTION of a novel pretreatment of the copper catalyst to reduce nucleation sites for graphene growth. The suppression of nucleation sites is very important to promote a more single-crystalline growth of graphene and thus minimize electron scattering at the domain boundaries of the graphene crystal grains. The procedure is based on a photocatalyst-assisted thermal annealing process that efficiently removes carbonaceous contaminants which are active sites for graphene nucleation.
- THE DEMONESTRATION of record-long propagation of spins over 30 micrometers at the graphene channel. Such output was achieved using high-quality CVD graphene grown on platinum foil and a newly developed device fabrication technique which minimizes contamination/structural defects during graphene processing. The spin lifetimes and relaxation lengths were the highest values reported at room temperature in CVD grown graphene on a standard substrate, SiO_2/Si.

Resumen

Esta tesis se ha basado en ajustar la síntesis y el procesamiento de grafeno para el desarrollo de dispositivos espintrónicos optimizados. La tesis está enmarcada en dos temáticas punteras: el mundo del grafeno con su riqueza de propiedades únicas y el campo de la espintrónica que explora el grado de libertad del espín de los electrones para nuevas aplicaciones en tecnología de la información y la comunicación (por ejemplo, dispositivos de lógica y almacenamiento de información). En este contexto, el grafeno es un material muy prometedor para transportar el espín con longitud de difusión alta. Para lograr esto, un grafeno de alta calidad con mínimos centros de dispersión de electrones es un parámetro clave y debe asegurarse estas propiedades desde el momento de su crecimiento y durante su procesamiento. Por lo tanto, en esta tesis, se han invertido muchos esfuerzos para ajustar los parámetros de crecimiento del grafeno mediante la deposición química por vapor (CVD). Se han logrado varias contribuciones relevantes en el campo:

- Se ha demostrado la importancia de la reacción inversa del grafeno ("etching") durante el crecimiento, la cual comienza a dominar a tiempos largos de crecimiento debido a un aumento in-situ de la concentración de hidrógeno. Este es un fenómeno que se ha ignorado anteriormente pero que es muy importante a tener en cuenta ya que afecta la estructura y morfologia del grafeno. Se ha logrado una caracterización completa de la evolución de la forma de los dominios del grafeno ajustando el tiempo de crecimiento, el flujo de precursores de gases

y el confinamiento del catalizador lo cual permite identificar mejor el inicio del proceso de “etching”. Controlar este efecto es muy relevante para minimizar los defectos estructurales inducidos por la reacción inversa ya que pueden afectar el transporte de electrones / espines.

- Se ha introducido un nuevo pretratamiento del catalizador de cobre para reducir los sitios de nucleación para el crecimiento de grafeno. La supresión de los sitios de nucleación es muy importante para promover un crecimiento más monocristalino de grafeno y minimizar así la dispersión de electrones en las fronteras de los granos de cristal de grafeno. El procedimiento se basa en un proceso de curado térmico asistido por fotocatalisis que elimina eficientemente los contaminantes carbono que son sitios activos para la nucleación de grafeno.
- Se ha demostrado una propagación récord de espín de más de 30 micrómetros en el canal de grafeno. Dicho resultado se logró utilizando grafeno CVD de alta calidad crecido sobre platino y una técnica de fabricación de dispositivos recientemente desarrollada que minimiza la contaminación/defectos estructurales durante el procesamiento de grafeno. La vida útil del espín y las longitudes de relajación resultaron ser los valores más altos en contrados a temperatura ambiente en comparación a resultados previos obtenidos en condiciones similares, es decir grafeno CVD sobre sustrato estándar de SiO2 / Si.

Resum

Aquesta tesi s'ha basat en la síntesi i el processament del grafè per tal d'obtenir les condicions òptimes per a la seva utilització en aplicacions d'espintrònica. La tesi està emmarcada en dos camps de recerca punters: el món del grafè amb la seva riquesa de propietats úniques i el camp de l'espintrònica que explora el grau de llibertat de l'espí de l'electró de cara a noves aplicacions en informàtica i tecnologia de comunicacions (com és ara els dispositius de lògica i d'emmagatzematge d'informació). En aquest context, el grafè és un material prometedor de cara a transportar l'espí amb grans longituds de difusió. Per aconseguir-ho, és clau que el grafè sigui d'alta qualitat amb el mínim de centres de dispersió, tant en el moment de la seva producció com en el processat. Per tant, en aquesta tesi s'ha fet un gran esforç per optimitzar els paràmetres de creixement pel mètode de deposició química per vapor (CVD). S'han aconseguit vàries contribucions rellevants en aquest camp:

- S'ha demostrat la importància de la reacció inversa del grafè ("gravat") durant el creixement, la qual comença a dominar per a temps llarg de creixement, degut a un augment de la concentració d'hidrogen in-situ. Aquest és un fenomen que ha estat ignorat anteriorment però que és de gran rellevància degut al seu efecte sobre l'estructura i la morfologia del grafè. S'ha aconseguit una caracterització completa de l'evolució de la forma dels dominis de grafè ajustant el temps de creixement, el flux dels gasos precursors i el confinament del catalitzador, fet que permet identificar millor l'inici del procés de "gravat". Controlar aquest efecte és molt important per minimitzar els defectes estructurals induïts per la reacció inversa ja que poden afectar el transport d'electrons/spins.
- S'ha introduït un nou tractament previ del catalitzador de coure per reduir els punts de nucleació per al creixement del grafè. La supressió dels punts de nucleació és molt important per tal de promoure un creixement més monocristal·lí del grafè i així minimitzar la dispersió dels electrons en la frontera dels grans de cristall del grafè. El procediment es basa en un procés de curat

tèrmic assistit per fotocatàlisi, que elimina eficaçment els contaminants de carboni que són punts actius per a la nucleació del grafè.

- S'ha demostrat una distància de propagació d'espí rècord, superior als 30 micròmetres, en el canal de grafè. Aquest resultat s'ha obtingut utilitzant grafè CVD d'alta qualitat crescut sobre platí i una tècnica de fabricació de dispositius recentment desenvolupada que minimitza la contaminació/ els defectes estructurals durant el processament del grafè. La vida útil de l'espí i les longituds de relaxació obtingudes han resultat ser els valors més alts aconseguits a temperatura ambient en comparació amb previs resultats obtinguts en condicions similars, és a dir, amb grafè CVD sobre substrat estàndard de SiO_2/Si.

Acknowledgment

I would like to thank Prof. Sergio Valenzuela, Dr Maria Jose Esplandiu and Dr. Marius V. Costache for their supervision, assistance, encouragement, personal guidance and valuable suggestions enabling me to accomplish my thesis work effectively.

I would also like to acknowledge Dr. Juan Sierra; for the training on device fabrication and transport measurement, Aloïs Arrighi for Raman characterization, Dr. Adriana Isabel Figueroa and Dr. Regina Galceran for their kind comment on the thesis writing, Dr. Matias Timmermans for developing program for data analysis, Dr. Frederic Bonell, Dr. Williams Savero, Antonio Benitez, Iván Fernández, Lorenzo Camosi and all my colleagues for their kind help, all the fun we shared. *Muchisimo gracias!!*

Special appreciation goes to Dr. Guillaume Sauthier for the XPS measurement and Dr. José Manuel Caicedo Roque for the help in the installation of the CVD set up. I would also thank the advanced microscope and nanofabrication division for the training in the microscope and nanofabrication.

I would like to thank Joshua Robinson for allowing me to carry out my research stay in his lab at Penn State University, United States. A word of thanks should be expressed to Natalie Brigs, Brian Bersch, Shruti Subramanian, and Alexandar Vera for their help and training to local instruments.

My special appreciation and gratitude go to my wife, Tirhas Kahsay, for her support, encouragement, affection and most importantly taking care of our little, Barok. This enables me to focus on the thesis work. I also appreciate my parents, sisters, and brothers for their love and kindness.

I would like to thank the Spanish Ministry of Economy and Competitiveness (MINECO) for granting my Ph.D. thesis. I would also like to thank Bahir Dar University, Ethiopia for the study leave to pursue my Ph.D. study.

Table of contents

Motivation and outline of the thesis

The quality of graphene is a key parameter and must be ensured from the moment of its synthesis and during the device fabrication process. Among the different growth methodologies, chemical vapor deposition is a promising technique for the production of high-quality graphene in a scalable and controllable manner. However, the synthesis of a high-quality graphene monolayer with a more monocrystalline character comparable to the one obtained by mechanical exfoliation is a very arduous task and still has many challenges to overcome. Moreover, it is also difficult to preserve the high quality of graphene in terms of contaminants and structural defects during its transfer processes as well as in its processing using nanofabrication tools.

Accordingly, the main objectives of this thesis are:

i) to fine-tune the growth parameters of the CVD process to achieve high-quality graphene and

ii) to further adjust the graphene processing to guarantee high performance electronic/spintronic devices.

The content of the thesis is organized in five chapters including introduction (chapter 1), experimental and methodologies (chapter 2), and three chapters based

on our result regarding growth (chapters 3 and 4) and high-performance spintronic devices fabrication (chapter 5).

In chapter 2, we show the experimental procedures and instruments/equipment used during the entire work.

In chapter 3, we demonstrate the importance of the graphene etching (reverse reaction) during growth which begins to dominate under certain circumstances. That is a phenomenon that has been previously ignored but impacts on the graphene domain reshaping. A thorough characterization of the graphene domain shape evolution has been accomplished by tuning the growth time, the flow of gas precursors and the Cu foil confinement which allows us to better identify the onset of the etching process. Controlling this effect is very relevant to minimize structural defects induced by etching which can impact on electron transport. Graphene grown at optimum conditions has shown a better quality and we have used such graphene to fabricate electronic/spintronic devices.

Under the context of achieving a more monocrystalline characteristic in the CVD grown graphene, we have also introduced a novel procedure to clean Cu foil and to reduce the nucleation density of graphene during CVD growth process. We studied the effect of photo-assisted cleaning by comparing the nucleation density inside and outside the photo-assisted annealed region and by studying the surface chemistry of the two Cu foil regions with X-ray photoelectron spectroscopy (XPS). We found

evidence of lower nucleation sites in the photo-assisted annealed region. We proposed a possible mechanism for these results based on a photocatalyst-assisted cleaning process. These results are presented in chapter 4.

Motivated by the promising application of graphene for spintronic applications, we demonstrated spin transport over a long (~30 μm) CVD graphene channel. We achieved this result using high-quality CVD graphene grown on platinum foil and a newly developed device fabrication technique which minimizes contamination/structural defects during graphene processing. Our devices show the highest values of spin parameters in CVD grown graphene on a standard substrate, SiO_2/Si. This part of the work is resumed in chapter 5.

Chapter 1: Introduction and background

Carbon is a group 14 element in the periodic table with four electrons available to form a covalent bond and it has exceptional ability to form σ and π bonds with itself or with other elements using its four valence electrons. Due to such an ability, carbon is capable of forming different allotropic forms including diamond, graphite, graphene, buckyball and carbon nanotubes. Diamond and graphite are well-known 3D allotropic forms of carbon. Graphene is a 2D allotrope of carbon with a hexagonal lattice formed by *sp2* hybridization. Graphene is considered as the basis of all graphitic materials, as it can be wrapped up to form fullerenes (0D), rolled to form carbon nanotubes (1D) or stacked to form graphite (3D) **Figure** 1.1 [1].

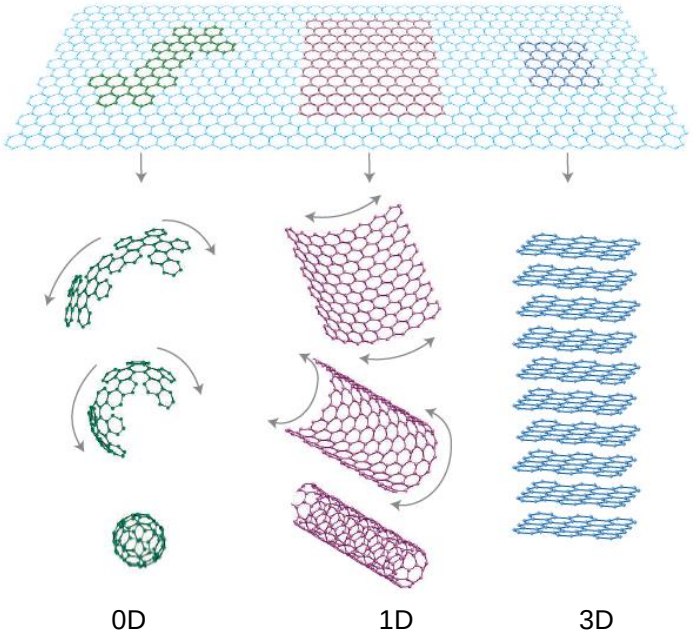

Figure 1.1. Transformation of graphene to other carbon allotropes: wrapped up to fullerenes (0D), rolled to carbon nanotubes (1D) or stacked to graphite (3D) [1].

Graphene has been studied theoretically as 2D graphite for more than sixty years [2]–[4] to explain the properties of various carbon materials [1]. The name graphene was given by Hanns-Peter Boehm and colleagues in 1986 [5] and then the International Union of Pure and Applied Chemistry (IUPAC) decide to include “graphene” as an official name for one atom thick carbon layer [6]. In 2004, Prof. Konstantin Novoselov and Prof. Andre Geim isolated monolayer graphene by scratching highly ordered pyrolytic graphite (HOPG) surface with scotch tape [7]. Since then a tremendous effort has been made to synthesize graphene and to study its properties. It has been shown that graphene has unique electrical, optical, mechanical and thermal properties that could bring about innovative applications.

Electrically, graphene is a zero-gap semiconductor [7]. The conduction band and valence band meet at Dirac point where there is a zero density of states (DOS) at Fermi energy (E_F) (**Figure** 1.2). Dirac points are six points in momentum space, consisting of two nonequivalent sets of three points (K and K' points) at the corner of the hexagonal Brillouin zone. In graphene, electrons and holes behave as relativistic Dirac fermions (zero effective mass) with extremely high electron/hole mobilities at room temperature (up to 200,000 cm^2/Vs with carrier densities of $n = 10^{12}$ cm^{-2}) [8]. In addition, graphene has the ability to transport spin current over a long distance because of its weak intrinsic spin-orbit coupling and negligible hyperfine interaction. This makes graphene an excellent candidate to transport spin information as will be discussed in section 1.5.

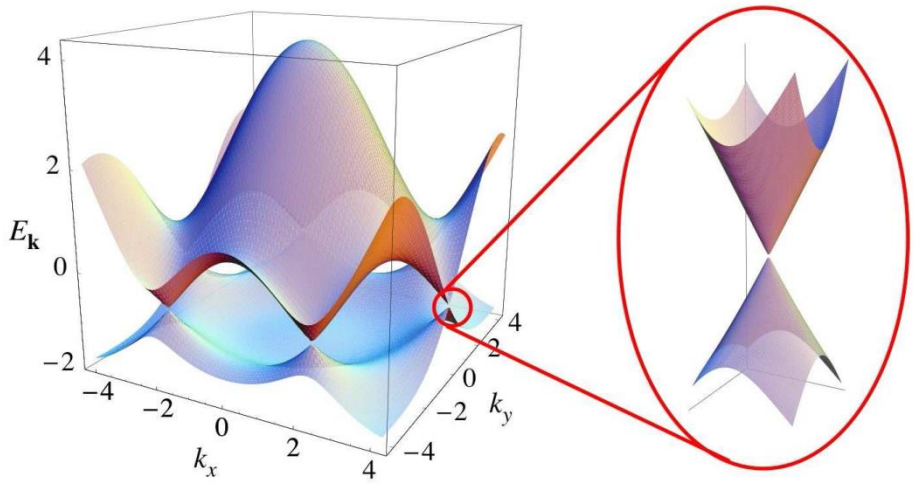

Figure 1.2. Band structure of graphene [9]. There is no gap between the valence band and conduction band; it is a gap-less semiconductor.

Another outstanding property of graphene is its mechanical property. Graphene is one of the strongest materials on earth and it possesses Young's modulus of 1 TPa and

intrinsic strength of 130 GPa [10], [11]. Graphene is a highly flexible material with high surface area to volume ratio (2630 m^2g^{-1}) [12] which makes it a potentially revolutionary material for sensors and flexible electronics.

Optically, monolayer graphene is transparent to incident white light (2.3% absorption) [13]. This makes graphene a promising candidate for exciting applications such as transparent electrodes in solar cells and touch screens [14]. Additionally, the opening of a band-gap with confinement also makes it a promising material for photovoltaic cells and transistors.

Chemically, graphene is a very inert material compared with nanotubes and buckyballs due to the consequence of the pure in-plane *sp2* bonds in its structure. In nanotubes and buckyballs, structures are built by out-of-plane *sp2* bonds as a consequence of the curvatures which make the bond to be more in tension, increasing reactivity.

The room temperature thermal conductivity of graphene is among the highest of any known material with values of up to 5,000 W/mK [12]. As it is well-known, heat is often a limiting factor for smaller and more efficient electronic in microprocessors.

These unique properties of graphene together with its potential applications have triggered immense interest from the research community. Therefore, mastering the synthesis and characterization techniques of graphene are needed in order to optimize its quality and to exploit its potential.

1.1 Introduction to synthesis techniques

Graphene can be obtained by numerous techniques including mechanical exfoliation, epitaxial growth from silicon carbide (SiC) [15], chemical exfoliation [16], chemical vapor deposition (CVD) [14] (**Figure** 1.3) and other potential methods [17]. Among these, chemical vapor deposition (CVD) is the most promising, cost-effective, and readily accessible approach for the growth of large-area high-quality graphene. Below we compare the different approaches. The advantages and drawbacks of some of the synthesis techniques are presented in table 1.

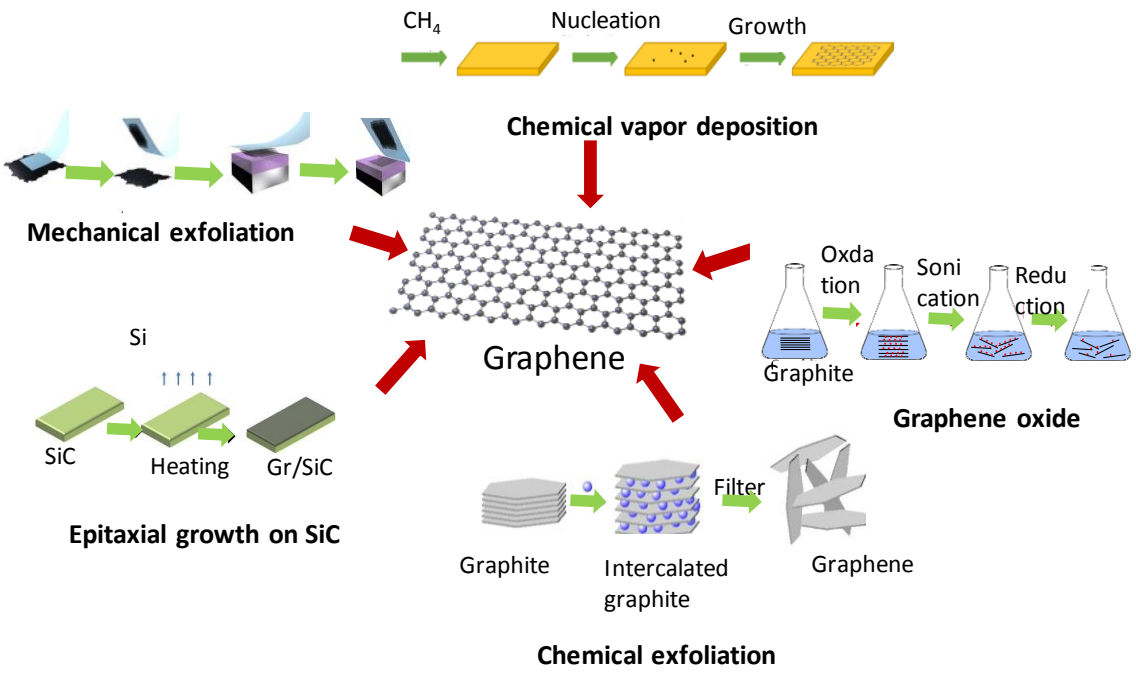

Figure 1.3. Chart showing selected graphene synthesis routes.

Table 1. Summary of the graphene synthesis processes with advantages and drawbacks

Synthesis techniques	Advantage	Drawbacks
• **Mechanical exfoliation (Scotch Tape)**	Very high-quality graphene Low defect Simple to prepare	• Non-scalable • Only for fundamental study
• **SiC epitaxial growth**	High-quality epitaxial graphene Few defects Device can be fabricated on the growth substrate.	• Substrate preparation • Difficult to transfer • Expensive substrate
• **Chemical exfoliation**	High throughput Low cost	• Small flake • Low purity
• **CVD graphene**	Large area graphene Scalable to industrial level High quality	• Needs transfer • Lack of homogeneity at large scale • Need high temperature to grow

Mechanical cleavage

Synthesis of graphene by mechanical cleavage is achieved by applying a force that overcomes the van der Waals interaction between the adjacent graphene layers of graphite. There are several exfoliation techniques including scotch tape method, sonication, ball milling, etc [7]. Amongst them, mechanical exfoliation by Scotch tape was the technique used by A. K. Geim and K. Novoselov in their seminal experiments to isolate graphene on a SiO_2 substrate [7]. This process is a promising technique for the production of high-quality graphene with the best device performance [18]. However, graphene obtained in this technique is only applicable to fundamental studies at a very small scale and is not practical for industrial applications.

Chemical exfoliation

The basic idea of chemical exfoliation is to break the forces among the layers of graphite using an appropriate solvent. For example, ultra-sonication of graphite powder in solvents with high surface tension such as N,N-Dimethylacetamide (DMA), γ-butyrolactone (GBL) and 1,3-dimethyl-2-imidazolidinone (DMEU) produces graphene flakes [16]. Exfoliation with these solvents takes place by overcoming the van der Waals force between the adjacent layers of graphite because of the strong interaction between graphitic basal planes and the appropriate organic solvents [16], [19].

Graphene can also be obtained from graphite through an oxidation/reduction process. Firstly, graphite is oxidized to facilitate the graphite exfoliation in aqueous

solution by sonication because graphene oxide is more hydrophilic than graphene due to the oxygenated functional groups. Then the dispersed oxidized graphene flakes are chemically reduced to provide graphene flakes [20].

Even though chemical exfoliation is a scalable and cost-effective technique, it is not suitable to obtain graphene with high electronic performance. This is due to the lack of control in shapes and number of layers and the inability to completely eliminate the adsorbed solvent or functional groups from the graphene surface.

Thermal decomposition of SiC

One reliable method for fabricating large-area single-crystalline graphene domains is the epitaxial growth of graphene from thermal decomposition of SiC. Annealing commercial SiC samples at high temperatures (>1650 ^{0}C) in an argon environment yields morphologically superior graphene layers on the SiC surface [15] [21]. Because of its higher vapor pressure, silicon atoms first desorb from the SiC substrate leaving behind carbon atoms to form a graphene layer. It is a promising route to obtain highly reproducible and homogenously large-area graphene for electronic applications [22]. Epitaxial growth of graphene has many advantages including the ability to produce monolayer graphene in a controllable manner and fabrication of devices directly on the growth substrate. Device fabrication is possible without the need of transferring it onto another substrate because SiC is a semiconducting substrate (SiC energy gap of 3.0 -3.23 eV). However, there are several limitations of this method, such

as the preparation of atomically flat SiC surfaces to be covered by a single layer of graphene, which requires advances in SiC substrate preparation [23]. In addition, there is an incomplete graphitized layer, a “buffer layer” (zero layer), between the monolayer and the SiC substrate, which degrades the electrical properties of graphene.

Chemical vapor deposition (CVD)

Chemical vapor deposition (CVD) is another technique for large-scale production of high-quality graphene. At this moment, CVD synthesis of graphene on transition metal substrates is the most promising approach as will be explained below. Since the focus of this thesis is on the synthesis of graphene using the CVD technique, in the next section we present a detailed description of the growth process.

1.2 Growth of graphene by chemical vapor deposition

Chemical vapor deposition (CVD) is a process whereby a solid material is deposited from a vapor state by a chemical reaction occurring on the surface of a heated substrate. There are varieties of CVD techniques including low pressure CVD (LPCVD), atmospheric pressure CVD (APCVD), plasma-enhanced CVD (PECVD) and laser enhanced CVD (LECVD). The CVD technique was implemented to grow monolayer graphene film in 2009 [24]. Since then, CVD has become a widely used technique to grow high-quality wafer-scale graphene films to supply the large demand in the realization of next-generation electronics [18]. LPCVD growth of graphene on top of transition metal catalyst is a favored approach over the other techniques due to its capability to grow high-quality, large-area graphene film with a controlled number of layers. It is a tunable, scalable and easy accessible technique that meets the desired requirements for both fundamental studies and scalable technological advances [18], [24]. Beyond this point, CVD is used indistinctly to refer to LPCVD.

1.2.1 CVD graphene growth mechanism

Chemical vapor deposition of graphene involves the injection of carbon sources such as hydrocarbons [24], polymers [25], organic solvents [26] or dry carbon source [27] into a reaction chamber to form new carbon-carbon bonds with the aid of heat, and

hydrogen and metal catalysts. Decomposition of precursor material and synthesis of new bonds are carried out at an elevated temperature ranging from several hundred degrees Celsius up to the melting point of the metal catalyst.

The growth of graphene on Cu foil substrates by CVD technique was first reported by Li, X. *et al* [24]. Later on, other transition metals like Ir [28], Ru [28], Ni [29] and Pt [30] have been used. Cu and Ni foils are currently the two most commonly used catalysts owing to their low cost, etchability and large grain size.

The mechanism of CVD graphene growth is substrate-dependent, so it has to be understood and tuned for each substrate. For example, the growth mechanisms on Ni and Cu foil are different. Growth on Ni foil takes place by carbon segregation [31] or precipitation [32] and thus it is not a surface controlled process **Figure** 1.4). The high solubility of carbon in Ni at high temperatures results in the formation of multilayer graphene sheets [33], [34]. On the other hand, graphene growth on Cu is by a surface controlled process because of the very low solubility of carbon in Cu, leading mostly to the growth of single-layer graphene [35]. Thus, unlike growth on Ni foil, which involves carbon dissolution, segregation, and precipitation, growth on Cu foil involves only surface adsorption [35], [36]–[38]**.**

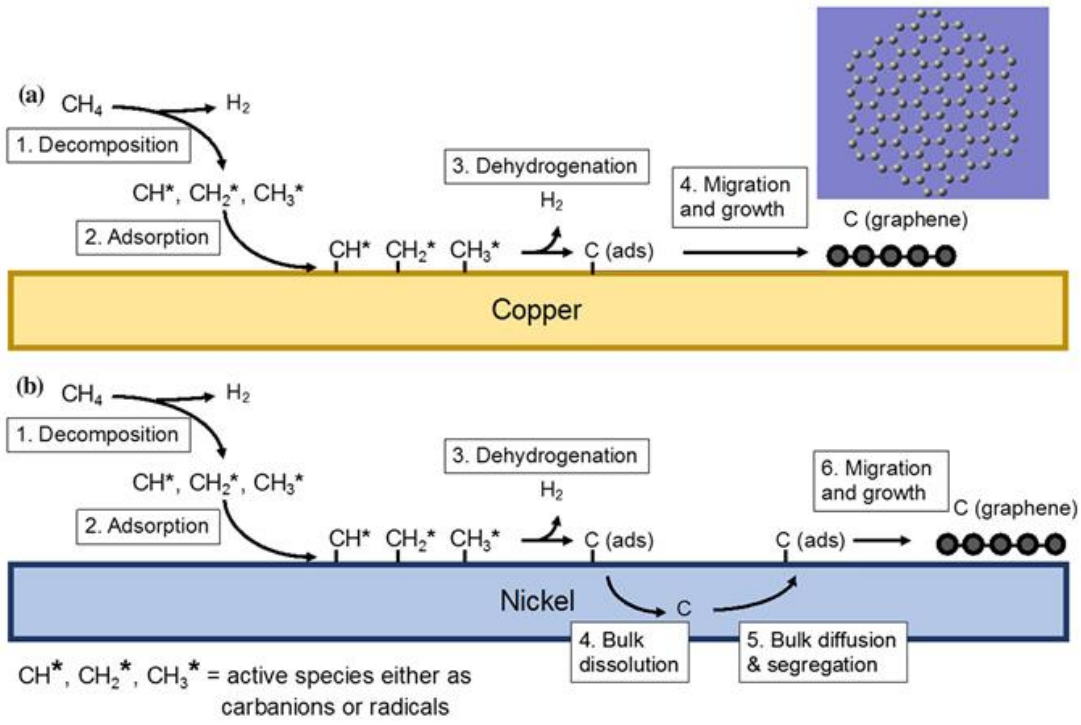

Figure 1.4. Mechanism of CVD graphene growth on Cu foil and Ni foil. For Ni foil, the carbon is dissolved inside the bulk of the Ni foil whereas, in the case of Cu foil, all the reactions take place on the surface [38].

The reaction mechanism on Cu foil has a sequence of steps including [38], [39] (**Figure** 1.4).

1. Adsorption of active H atoms to the Cu surface
2. Adsorption of CH_4
3. hydrogen catalyzed dehydrogenation of CH_4 into active carbon species (CH_3), (CH_2), (CH) or (C)
4. Surface migration
5. Graphene nucleation and carbon incorporation into the growing graphene layer

The kinetic of graphene growth on Cu foil follows the conventional kinetic model for the thin-film deposition in a CVD reaction. It involves the mass-transport (diffusion) of reactants from the gas phase to the surface and the surface-reaction process which includes the reactant adsorption, decomposition, migration to the attachment sites for incorporation. The rate of the mass-transport process in the gas phase (J_g) is controlled by the difference of the reactant concentration in the gas and at the surface (Cg-Cs) and the gas transport parameter (h_g) according to the equation $J_g = h_g(Cg - Cs)$. The mass transport coefficient expression ($h_g = D_g/\delta$) depends on the gas diffusion coefficient (D_g) and the boundary layer thickness (δ). The boundary layer thickness is distance-dependent from the gas inlet and is mathematically expressed as $\delta(x) = (\mu x/\rho U)^{1/2}$ where μ represents the gas viscosity, ρ the gas density, U is the gas reactant's flow velocity and x is the distance between initial gas flow point and the substrate (**Figure** 1.5) [40]. Therefore, a low gas flow rate induces a thicker boundary layer, δ and reduces the mass transport rate h_g.

The surface-reaction process is proportional to the reaction constant (k_s), which increases exponentially with the reaction temperature. When $h_g << k_s$ the growth process is limited by the mass transport from the gas phase, in contrast when $k_s << h_g$ the growth process is limited by the surface reaction. It has been demonstrated that processes controlled by the surface reaction yield more uniform CVD growth. Low pressure CVD is more likely to be surface reaction limited since the gas flow velocity is very high due to the pumping process, resulting in a high value of the mass transport

parameter h_g. Therefore, for an improved film thickness uniformity of graphene, low pressure CVD is desirable.

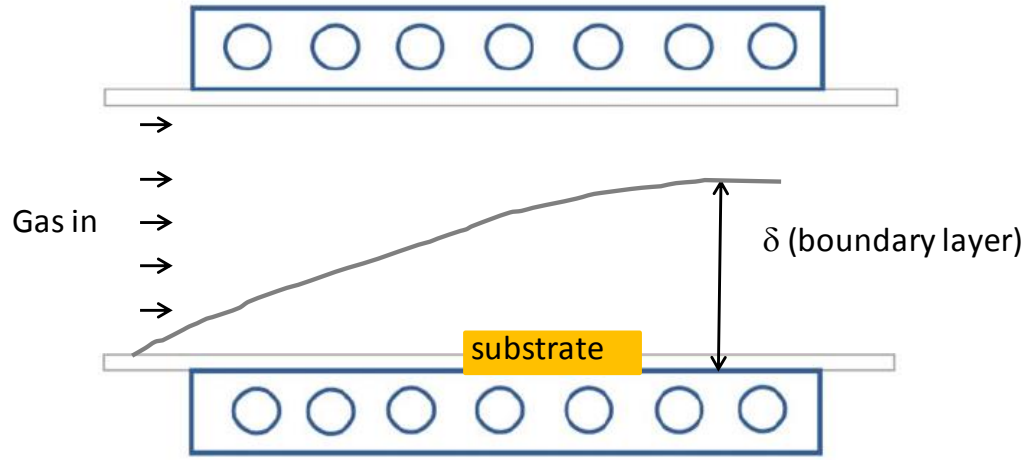

Figure 1.5 A schematic of boundary layer above the substrate. The thickness of boundary layer increases when the distance from the gas inlet increases.

Next, we detail some of the most important parameters to control the growth of graphene.

Metal catalyst: As mentioned before depending on the metal catalyst the resulting graphene can be a single layer or multilayer. Growth on Cu foil is surface-mediated and self-limiting which leads to the formation of large-area graphene films with uniform thickness. Whereas growth on Ni foil shows graphene with the coexistence of a wide variation in thicknesses over the metal surface, from a monolayer to many layers.

Hydrogen: Hydrogen is a widely used gas both in annealing and growth processes. During the annealing step, hydrogen plays a role in the cleaning of the Cu

surface by reducing the surface oxide and reconstructing the Cu foil, leading to a smoother surface.

In the growth stage, hydrogen controls the area of coverage and the quality of graphene [41]–[44]. Hydrogen acts as a catalyst for the decomposition of CH_4 into active carbon species (CH_3, CH_2, CH or C). In the presence of hydrogen, the physisorption of CH_4 on the Cu foil is promoted to form surface-bound (CH_3) radicals and other carbon species. The dehydrogenation of methane on the Cu foil surface to (CH_3) radical without hydrogen catalysts is unfavorable since it requires a high activation barrier [45]. It also activates the surface-bound carbon to facilitate nucleation for monolayer growth. Hydrogen acts as etchant (graphene + $(H)_s \rightarrow$ graphene-C + CH_4) which helps to control the size and morphology of the resulting graphene domains [41], [46].

Methane: The methane to hydrogen ratio plays a critical role in controlling the nature of graphene such as the number of layers and nucleation density. At low methane to hydrogen ratio, the carbon species are diluted in hydrogen gas and favor the growth of large-size single-crystal graphene flakes [47].

Argon: It is also used as buffer gas in order to maintain the uniformity of flow rates and to dilute the methane for homogeneous distribution of gases at the growth zone [41]. The argon flow can modify that boundary layer thickness and hence the reaction process. The boundary layer is also affected by the total pressure and the velocity of the gas as discussed before.

1.2.2 Towards the growth of large-size single-crystal graphene on Cu foil

Usually, the graphene grown on a standard Cu foil has polycrystalline nature and the grain boundaries significantly lower the electron transport performance of the resulting graphene devices [45], [48]. Tremendous efforts have been devoted to finding a way for the growth of large-size single-crystal graphene domains on Cu foil, which can be summarized into two main approaches: (i) reducing the nucleation density and (ii) merging epitaxially grown domains.

(i) Single crystal graphene by reducing the nucleation density

To achieve a large single-crystal graphene domain by this approach the nucleation density of graphene should be minimized by decreasing, for instance, the active sites for nucleation (such as contaminants, domain boundaries, structural defects, etc.). Nucleation density can be reduced by manipulating the Cu foil using different techniques such as Cu foil pre-treatment, oxygen-assisted passivation [49], growth inside Cu foil pocket [50], and tuning the carbon precursor feeding [51].

Cu foil pre-treatment

Nucleation density can be reduced by pre-cleaning the Cu foil with different procedures. It is well known that Cu foil with purity level 99.98- 99.999% has a range of impurities that promotes nucleation centers leading to a higher nucleation density [52]. Various precleaning procedures such as electrochemical polishing and etching with

acidic solutions have been implemented to minimize the level of impurity from the surface and bulk of the Cu foil.

Electrochemical polishing is an electrochemical process that removes material from a metallic surface. It is a widely used precleaning procedure to remove surface contamination and to improve the surface smoothness [53], [54]. It is a critical step to obtain a homogeneous graphene film as well as to control the nucleation density. **Figure** 1.6 presents a typical electropolishing setup scheme composed of two electrodes (anode and cathode) which are immersed in an electrolyte solution and they are electrically connected to a DC power source. In the setup, the working piece of the Cu foil is connected to the anode (where the oxidation takes place) and another Cu foil is connected to the cathode (where the reduction takes place). The electrolytes for electropolishing are mainly concentrated acid electrolytes with high viscosity (typically phosphoric acid-based) [55].

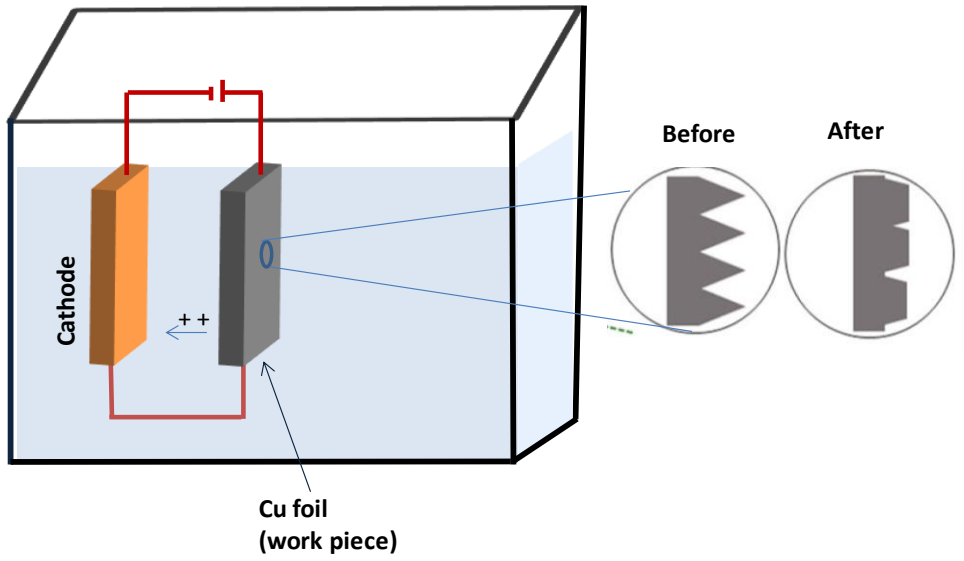

Figure 1.6. A typical electrochemical polishing setup.

Chemical treatment: dipping Cu foil inside chemicals such as **acetic acid and nitric acid** [56], [57] has been reported to remove inorganic impurities from the surface of the Cu foil. For instance, the removal of native oxides from Cu foil by acetic acid follows the reactions mechanisms below:

$CuO + 2CH_3COOH \rightarrow CH_3COO\text{-}Cu\text{-}OOCCH_3 + H_2O + H_2$

$Cu_2O + 4CH_3COOH \rightarrow 2CH_3COO\text{-}Cu\text{-}OOCCH_3 + H_2O$

Since the Cu acetate ($CH_3COO\text{-}Cu\text{-}OOCCH_3$) is soluble in water, the acetate part is cleaned with excess water leading to a metallic Cu.

Oxygen passivation: After Ruoff's group [49] reported the use of oxygen in reducing the nucleation density, many growth results included the use of molecular oxygen for few minutes at the end of annealing (right before the CH_4 flow). The role of surface oxygen on reducing the nucleation density of graphene by passivating the surface of Cu foil has been investigated thoroughly and it could [49]:

- Reduce nucleation density and foster the growth of large single-crystal graphene domains
- Lower the C species edge attachment barrier and shift the graphene domain shapes from compact to dendritic for the growth of large size single-crystal graphene (**Figure** 1.7).

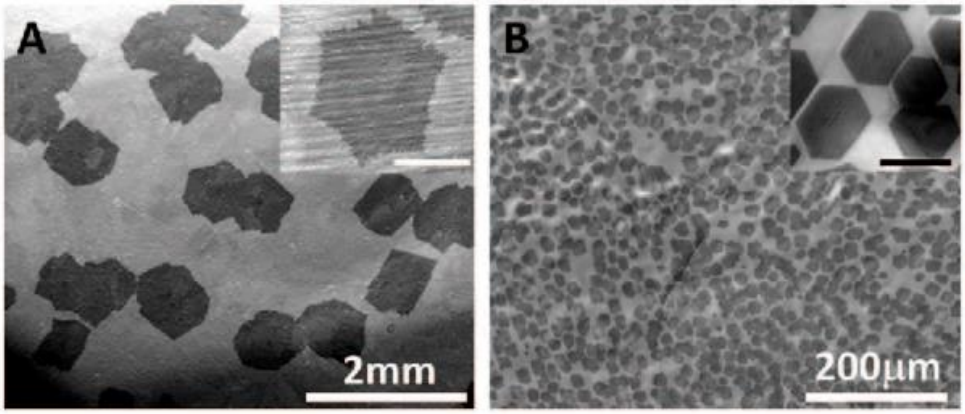

Figure 1.7. The effect of oxygen on graphene nucleation density and domain shapes on Cu foil. Typical SEM images of graphene domains grown on **a**) with oxygen, **b**) without oxygen [49].

Control feeding of methane to the substrate: the nucleation density of graphene has also been reduced by locally feeding the carbon precursors to the desired position of a substrate composed of an optimized Cu–Ni alloy. According to the report, the local feeding allows the growth of a single nucleus due to the isothermal segregation mechanism mediated by the nickel. The nickel-mediated isothermal segregation involves abundant carbon atoms dissolved in the alloy, boosting the growth rate of the graphene [51] (**Figure** 1.8**a**)**.**

(ii) Large single-crystal graphene by merging epitaxially grown domains

This is the second strategy to grow single-crystal graphene from epitaxially grown graphene domains that are merged into one single-crystal graphene domain. This can be achieved by changing the polycrystalline Cu foil into a monocrystalline structure using high-temperature annealing. The growth of graphene on a single crystal Cu foil follows an epitaxial growth mechanism.

Recently, a 5 x 50 cm^2 single-crystal graphene has been grown on commercially available Cu foil by merging epitaxially grown graphene domains [58] (**Figure** 1.8**b)**. In this work, the polycrystalline Cu foil is annealed to form a single crystal Cu[111] foil. Growth on a single crystal Cu foil is epitaxial and merging of the epitaxially grown graphene provides large single-crystal graphene film [58].

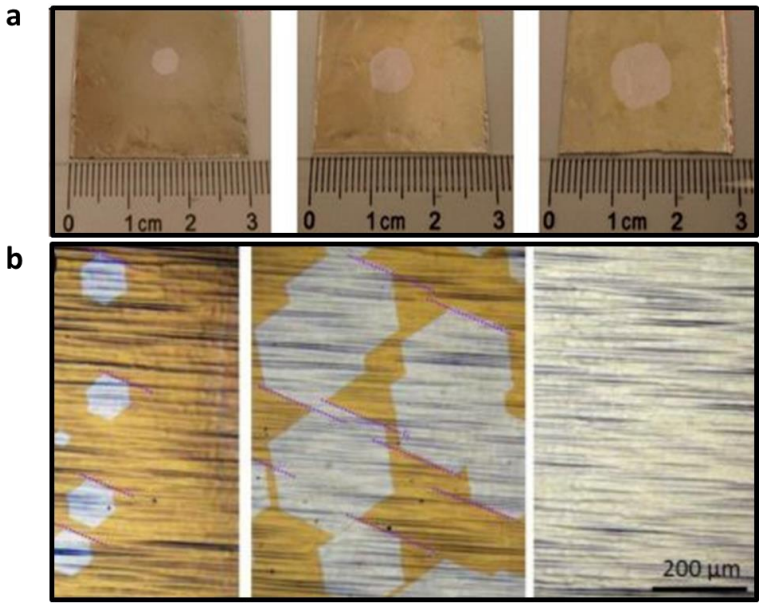

Figure 1.8. Optical microscopy image showing: **a**) the evolution of graphene domain from a single nucleus to large size graphene (following the first approach) [51]. **b**) The evolution of epitaxially grown graphene domain to form large-single crystal graphene (following the second approach) [58].

1.3 Transfer of CVD-grown graphene

Generally, to use CVD-grown graphene for practical applications such as electronic and optoelectronic devices, a transfer process is needed to move the as-grown graphene from the growth substrate to the desired substrates; otherwise, graphene should be grown directly on the desired substrate. Graphene obtained by direct growth on a dielectric substrate (such as sapphire, quartz, mica, Si, glass) avoids the transfer-induced contamination [59], [60]. However, the growth process is not efficient because it is limited by the low activation energy; as a result of this low energy, the graphene formation reactions are slow and the control of the quality and sizes of graphene film is rather troublesome.

Therefore, the transfer of CVD graphene from the metal substrate to the desired dielectric substrate is a popular way to make devices. Several graphene transfer techniques have been developed, such as wet transfer, electrochemical delaminating, dry transfer using PDMS or thermal release tape [61].

1.3.1 Wet transfer

The wet chemical transfer process is a widely used process that involves the use of polymers such as polymethyl methacrylate (PMMA) as temporary support and substrate etchants such as iron chloride ($FeCl_3$), hydrochloric acid (HCl) or ammonium persulfate $(NH_4)_2S_2O_8$ [62], [63]. This transfer technique involves the following steps:

1. Spin coating of the PMMA on one side of the graphene/Cu foil stack
2. Removal of the graphene on the other side of the Cu foil using chemical or O_2 plasma,
3. Etching of Cu foil followed by a thorough cleaning with deionized water
4. "Fishing out" the PMMA/graphene stack with the desired substrate and subsequent drying
5. Removal of PMMA by dipping in acetone and cleaning with isopropanol alcohol

The drawback of this technique is the trapping of ionic species between graphene and substrate interface during fishing. It also leaves polymer residue on the surface of graphene which might act as scattering centers.

Electrochemical delamination using electrolyte solutions such as sodium hydroxide (NaOH) and tetraethylammonium hydroxide ($N(CH_2CH_3)_4OH$) [64] is another promising transfer technique. It is based on the intercalation of hydrogen bubbles between the interface of graphene and metal substrate as a consequence of the cathodic polarization of metal/graphene in such electrolytes. The H_2 bubbles lead to the decoupling of the graphene film as illustrated in **Figure** 1.9**.** This technique has a number of advantages, for example, it is non-destructive for graphene grown on both sides of the metal substrate, the metal substrate can be reused, and it can be used in less reactive (non-etchable) and expensive growth substrates such as Pt and Au.

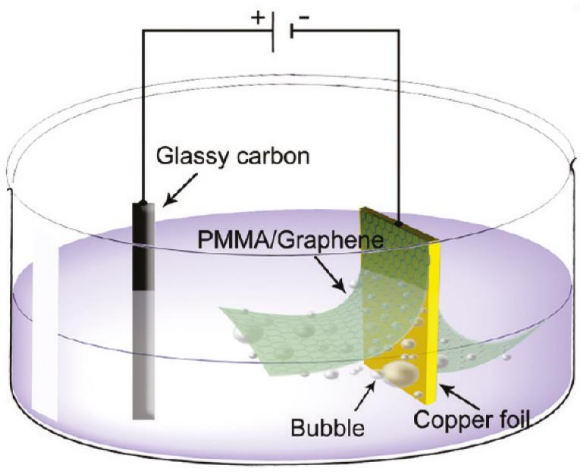

Figure 1.9**.** Schematic illustration for the electrochemical delamination of graphene from the Cu foil [64].

Transfer by intercalation of hot water has also been reported [65]. According to this method, water molecule enters between the graphene and Cu interface to decouple the graphene film from Cu foil. The growth substrate can also be reused. The limitation of this process is that water bubbles can create defects in graphene film.

1.3.2 Dry transfer

In the dry transfer technique, the transfer of graphene onto the target substrate does not involve any chemical etchant solution. Polymer support like PDMS [66] and thermal released tape (TRT) [67] are often used for the dry transfer process and then removed by thermal treatment. A typical dry transfer technique has been reported using polymer/hBN stamps (PDMS/PMMA/PVA/hBN) to mechanically pick-up the CVD-grown graphene flakes from the Cu foil and to deposit them onto arbitrary substrates

[68]. Then the PDMS/PMMA/PVA is removed by dipping in a DI water leaving a hBN (hexagonal boron nitride) protected graphene flake. This method uses the advantage of the weak van der Waals interaction between graphene and Cu foil compared to the interaction between graphene and hBN. The dry transfer avoids the interference of water molecules in the graphene-substrate interface. However, in this technique, the size of the transferred graphene is not scalable because it is limited by the dimensions of the hBN flakes.

1.4 Characterization of graphene

Structural characterization involves measurements based on various microscopic and spectroscopic techniques. They allow determining the number of graphene layers, their purity, and density of defects. In this section, we will focus on the most effective and widely implemented microscopic and spectroscopic techniques available to characterize graphene, which is also used in this thesis.

1.4.1 Microscopic characterization

Optical and electron microscopes

Optical microscopy is a non-destructive technique for fast visualization of graphene film on an appropriate substrate with the illumination of white light. Monolayer graphene is almost transparent (2.3% absorption) (**Figure** 1.10**b**) [13] and it is not always straightforward to visualize the single-layer graphene using an optical microscope. However, by choosing an appropriate substrate and wavelength, graphene can be visualized easily due to the different color contrast coming from the light interference effect on the substrate. **Figure** 1.10**a** shows a color plot for the expected contrast as a function of SiO_2 thickness and wavelength [69]. **Figure** 1.10**c** is typical images of patterned graphene visualized on 90 nm of SiO_2/Si substrate.

Scanning electron microscope (SEM) is a widely available technique for detail imaging of a sample by scanning the surface of the sample with an energetic electron beam to obtain information about surface details, homogeneity and elemental composition of the sample. **Figure** 1.10**d** shows a typical SEM image of hexagonal graphene with etched edges.

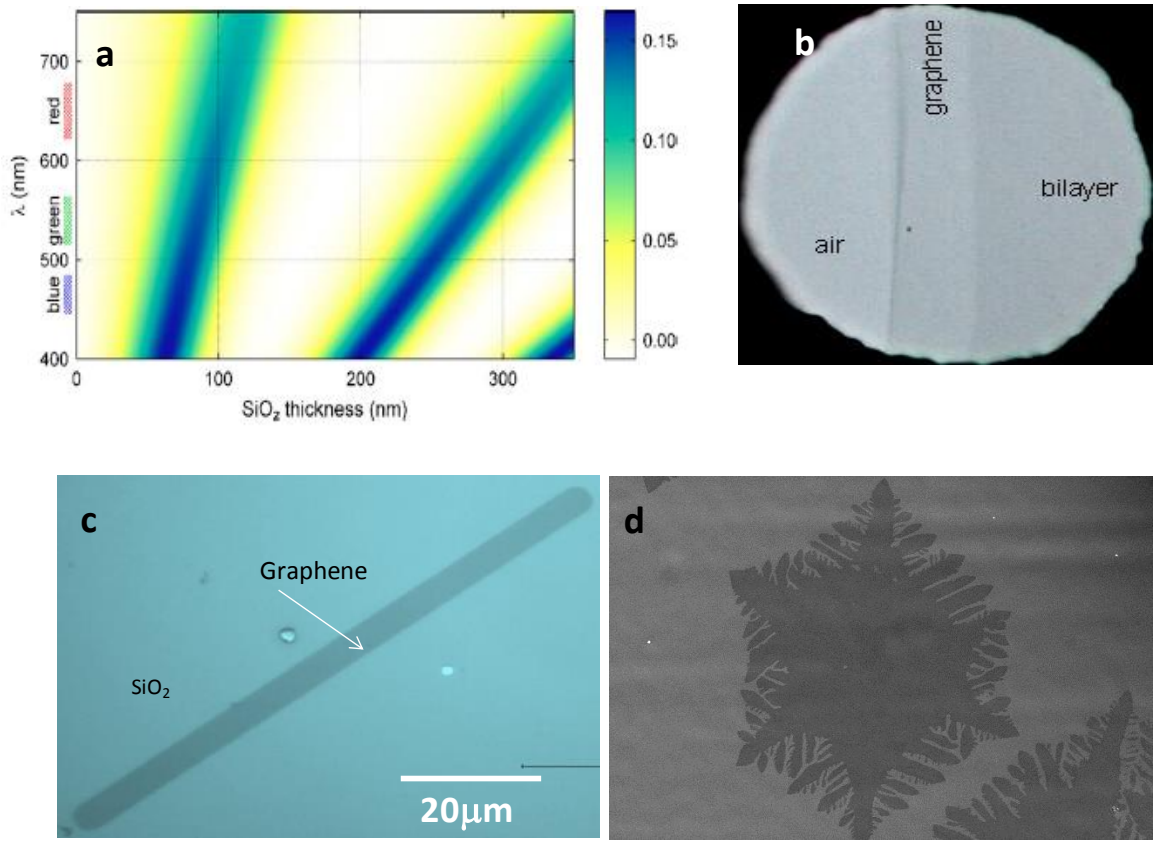

Figure 1.10. **a**) A color plot of the contrast as a function of wavelength and SiO_2 thickness color expected contrast on the right [69]. **b**) Photograph of free-standing single-layer and bilayer graphene [13]. **c**) Typical optical microscope image of lithographically patterned Graphene on 90 nm SiO_2/Si, **d**) SEM image of graphene on Cu foil substrate.

Transmission electron microscopy (TEM) is also a technique that uses a focused electron beam to obtain information about the sample at the nano- or microscale. However, unlike SEM, which uses emitted electrons from the sample, TEM uses electrons transmitted through the thin (about 100 nm thick) sample to get information about the sample. In combination with selected area electron diffraction (SAED), TEM can also provide information about the crystalline nature of graphene film.

Atomic force microscopy (AFM) is a powerful technique to characterize graphene film morphology, roughness and uniformity with reasonably high (sub-angstrom) resolution [70]. The number of layers is determined by considering the thickness of monolayer graphene, which is 0.35 nm. However, different thickness values of single-layer graphene (0.4 to 1.8 nm) have been reported in the literature [71]. These values vary widely compared to the interlayer distance between two layers of graphene sheets (0.335 nm) in a graphite structure [72]. This deviation in the measurement values is believed to be caused by substrate-graphene interaction, AFM probe-graphene interaction, or sample preparation which can induce water layer trapping in between the substrate and graphene [73]–[75].

1.4.2 Spectroscopic characterizations

Raman spectroscopy is the widely used characterization technique for the investigation of carbon allotropes depending on the difference in the geometric structure and bonding within molecules [76]. In graphene, there are three main characteristic Raman peaks: the primary in-plane vibrational mode, G (1580 cm-1), a second-order overtone of a different in-plane vibration, 2D (2690 cm^{-1}) and the disorder D (1350 cm^{-1}) peaks [77]. The number of graphene layers can be distinguished from individual peaks or from the combination of the two main bands, G and 2D.

G band

The G band is an in-plane vibrational mode involving the *sp2* hybridized carbon atoms that comprise the graphene sheet. The number of layers of graphene can be determined from the position and intensity of the G band. As the number of layers of graphene increases, the position of the G band shifts to lower energy (redshifted). This indicates that the bond energy is softened with the addition of bonds. However, sometimes the shift in the position of G band position might be related to impurity-induced doping of graphene [78]. The intensity of the G band follows a linear trend as the number of layers of graphene increases from single to multilayer graphene.

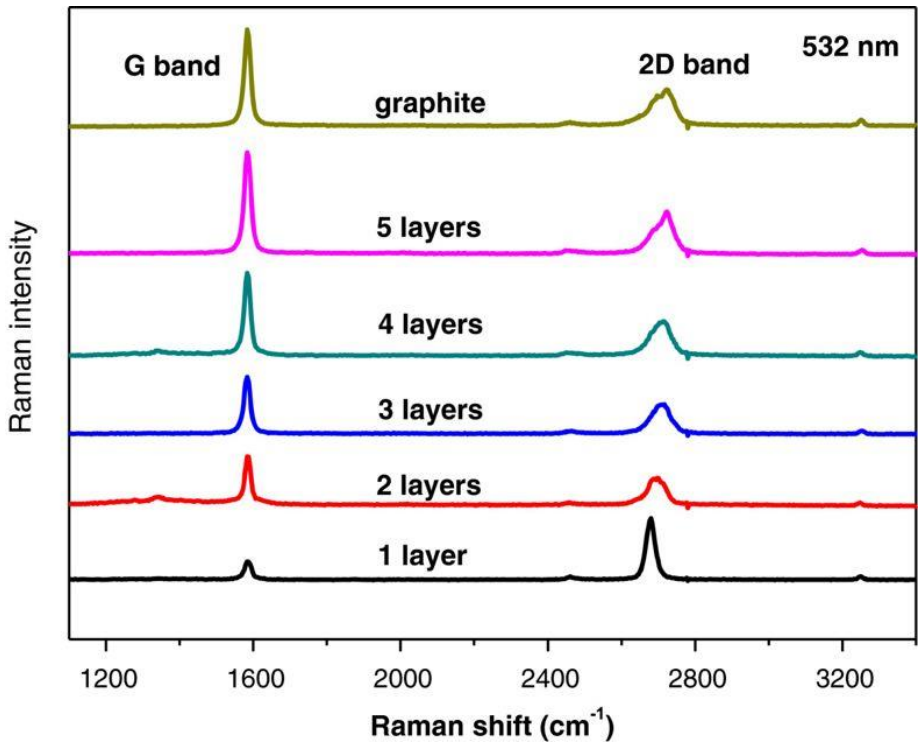

Figure 1.11. The two principal Raman peaks of few-layer graphene with the position of G peak and the spectral features of the 2D band [79].

2D band

In a 2D band or second-over-tone band, the number of layers can also be determined from spectra position and shape. Single-layer graphene has a symmetrical peak with a Full Width at Half Maximum (FWHM) of 30 cm^{-1}. As the number of layers increases, peak splitting occurs and the FWHM value increases. The ratio of the band intensity of G/2D also gives information about the number of layers of graphene. Single-layer graphene has a G/2D intensity ratio of about 0.5. **Figure** 1.11 shows a comparison of Raman spectra at 532 nm laser for the number of graphene layers based on the position of G peak and the spectral features of the 2D band [79]. As shown in the **Figure**, the intensity of the G peak increases as the number of layers increases.

D band

The D or the disorder/defect band is the main indicator of graphene defects and its intensity is directly proportional to the defect level of the graphene sample. For best quality graphene the D peak is negligible.

Another promising spectroscopic characterization is X-ray Photoelectron Spectroscopy (XPS). It is a widely used surface analysis technique that provides quantitative information and the nature of the chemical state of the sample. In the XPS technique, the sample is irradiated with mono-energetic Al kα X-rays causing the emission of photoelectrons from atoms in the near-surface. Then the emitted photoelectrons are collected by an energy analyzer so that the intensity of the

photoelectron peak is plotted as a function of binding energy of the electrons. From this, the elemental identity, chemical state, and quantity of specific elements can be determined. XPS is a powerful technique for the analysis of graphene with a characteristic *sp2* carbon peak at 284 eV. Graphene also has a distinctive signal, the π–π* (HOMO–LUMO) transition that is a characteristic shake-up line (satellite peak) for aromatic carbon at higher binding energies above 290 eV.

1.5 Charge and spin transport in graphene

In addition to the structural analysis, charge and spin transport characterization are essential to determine the quality of graphene. In charge transport experiments, carrier mobility and conductivity of graphene are extracted at different carrier densities using the field-effect transistor configuration. In spin transport measurements, the spin diffusion length and the spin relaxation time are obtained. Throughout this section, we shortly present the fundamental aspects of a graphene field-effect transistor and spin transport measurements, which will help to understand the experimental results presented in chapters 3 and 5.

1.5.1 Graphene field-effect transistor

Graphene is a zero-overlap semimetal with both holes and electrons acting as charge carriers. The number of charge carriers (holes or electrons) per given area of the graphene sample is known as the charge carrier concentration, *n* of graphene. The

charge carrier concentration of graphene devices can be controlled with an external voltage (back gate voltage, V_g) typically applied to the supporting (highly doped) substrate. The change in the charge carrier concentration tunes the conductivity of graphene.

SiO_2 on *p*-doped silicon (SiO_2/Si) is one of the most commonly used substrates for graphene devices. Together with the graphene, it forms a single-dielectric capacitance in which graphene and *p*-doped Si are the two plates separated by SiO_2 (**Figure** 1.12**a**). Therefore, the graphene's carrier density *n* is given by:

$$n = \frac{\varepsilon_0 \varepsilon_r}{de} V_g \quad \text{or} \quad n = aV_g, \qquad \text{where} \quad a = \frac{\varepsilon_0 \varepsilon_r}{de}$$

where ε_0 is the permittivity of free space ($\varepsilon_0 \sim= 8.854\times10^{-12}$ F/m), ε_r is the dielectric constant of SiO_2 (ε_r = 3.9), *d* is the thickness of SiO_2 layer (in our case d = 90, or 440 nm) and *e* is the electron charge (e = 1.602×10^{-19}C). In the case of 90 nm and 440 nm thickness of SiO_2, the corresponding α values are 239 x 10^9 and 49 x 10^9 $V^{-1}cm^{-2}$, respectively. When the population of holes and electrons are equal, the net charge carriers available for conduction is close to zero and, at this point, the resistance becomes high. This point is known as the charge neutrality point (CNP). In the case of pristine graphene (free from any impurity or doping), the CNP appears at 0 V. **Figure** 1.12**b** shows a typical graphene resistance as a function of the back-gate voltage. In this case, the CNP (V_{CNP}) is shifted towards positive gates, indicating that graphene is *p*-doped and that the Fermi level is lowered. Here, *n* should be calculated after subtracting the voltage at CNP (V_{CNP}) from the back-gate voltage V_g.

$$n = a(V_g - V_{CNP})$$

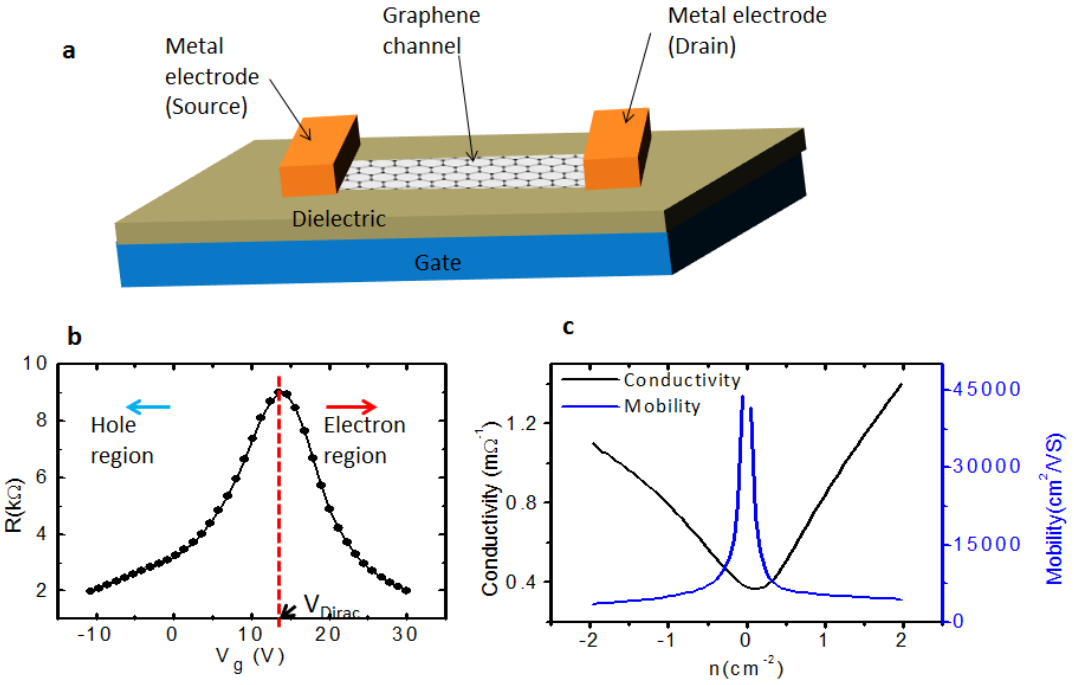

Figure 1.12**. a**) Schematics for graphene field-effect transistor, **b**) a typical plot for graphene resistance as a function of the back-gate voltage V_g. **c**) A typical plot for the conductivity and mobility of graphene as a function of carrier concentration.

The charge carrier transport in a material is limited by the strength of the scattering events. Due to the weak scattering in graphene and suppressed backscattering, charge carriers move easily. In the ballistic regime, the scattering events are absent and graphene charge carriers move with the Fermi velocity v_f = ~ 10^6 cms^{-1} [80] but in the diffusive transport regime, scattering event occurs which could arise from:

- Coulomb scattering by charge impurities (primary trapped charges in the underlying substrate),
- short-range scattering (defects, adsorbates) in or on graphene, surface roughness or graphene ripples [80], [81].

The scattering strength is determined by measuring the charge carriers transport which is quantified by the mobility μ [82]. Mobility is a measure of how well the charge carrier moves in a given material and has become the most commonly used metric for the electronic quality of graphene. It is obtained from the ratio between the carrier drift velocity to the electric field *E*,

$$\mu \equiv \upsilon/E \; \sigma = \sigma /en$$

Where υ *is* Drude carrier drift velocity, *E* is applied electrical field, σ is conductivity and *e* is electron charge. The conductivity in graphene is calculated by:

$$\sigma = L/WR$$

Where *L* is the channel length, *W* width of the graphene and *R* is the measured resistance. **Figure** 1.12**c** shows a typical plot of conductivity and mobility as a function of carrier density calculated from a typical gate dependent resistance of a graphene device. The reported room temperature mobility of graphene vary from 1,000 up to 70,000 cm^2/Vs on SiO_2 [83], 200,000 cm^2/Vs for suspended graphene [8] and exceeds 350,000 cm^2/Vs for heterostructures formed by tungsten diselenide (WSe2), graphene and hBN[84].

1.5.2 Towards high mobility graphene devices

Ideally, to get high carrier mobility, the graphene device should be free from defects, grain boundaries and potential residues. The graphene should also lie on an ultra-flat and lattice-matched substrate. In reality, graphene devices suffer from various sources of charge scattering. There are several approaches to reduce scattering centers and to increase carrier mobility in graphene devices.

Annealing: Transfer and device fabrication processes are potential sources of polymeric residues such as PMMA and other photolithography or electron beam lithography resist polymer residues. After chemical cleaning, exposing the graphene surface to thermal annealing has been shown to remove some of the thin layers of residue from the surface of graphene [85]. Thermal annealing can be carried out under Ar/H_2 atmosphere or under vacuum. Current-induced annealing also removes contaminants and the cleaning process takes place inside the measurement set-up *(in-situ*) [86].

Substrate engineering: Substrate-induced scattering can be minimized by using a substrate with few or no charge impurities, flat surface, and no interfacial polar phonon modes. SiO_2/Si is the commonly used substrate, which has been shown to exhibit lower carrier mobilities than the theoretical prediction because of the possible scattering from charged surface states, impurities and surface roughness [87], [88]. Covering SiO_2 substrate with hydrophobic chemicals such as hexamethyldisilazane (HDMS) diminishes the SiO_2-induced scattering effect. Hexagonal boron nitride (hBN) substrate has also

been shown to dramatically improve carrier mobility. In particular, Dean *et al*. have reported that the use of such a substrate leads to an enhancement of graphene's carrier mobility up to 60,000 cm^2/Vs [89]. The reason for the mobility improvement is that the hBN substrate is ultra-flat, inert, free of charge traps, free from dangling bonds and with small (1.7%) lattice mismatch with graphene [90], [91].

Elimination of defects or grain boundaries: Avoiding the grain boundaries by growing large single-crystal graphene has been shown to improve the mobility of graphene [92]. Minimizing the formation of defects during device fabrication processes could also improve the charge carrier mobility of graphene devices.

1.5.3 Spin transport

Spin-electronics or spintronics is the use of electron's spin degree of freedom to process, transfer and manipulate information. Spintronics helps to build micro and nanotechnology devices with enhanced performances or novel functionalities [93], [94]. Enormous effort has been given to the field of spintronic especially in injecting, transporting, detecting, and manipulating spin-polarized electrons in metals and semiconductors [95]–[97]. However, one major challenge is to find a suitable spin transport channel with long spin lifetime and long-spin diffusion length. Graphene is an ideal platform to host spin transport [9], [98], [99]. First-principle calculations have yielded spin relaxation times of up to 1 μs and spin diffusion length exceeding 100 μm [100], [101]. Most recent estimations, using full quantum simulations, suggest much

shorter spin lifetimes [99]. However, in high-quality graphene, it would be still possible to achieve spin transport over distances approaching 100 μm.

Spin transport in graphene

Spin injection into graphene: Spin injection is the transfer of spin-polarized charge carriers from ferromagnetic materials (FM) to non-magnetic materials (NM), in this case, graphene, to create a non-equilibrium spin density in NM. There are different approaches to inject spin-polarized electrons to graphene. Depending on the nature of the interface between graphene and the FM electrodes, they can be grouped into three major classes [98].

i) Injection through pinhole barriers in which injection takes place through tiny holes in an insulating barrier [102],
ii) Direct injection from FM materials to graphene without a barrier in the case of transparent contacts [103] and
iii) Injection through a tunnel barrier in which injection takes place through the thin layer of insulators.

Amongst them, injection using a FM in combination with a tunnel barrier (iii) shows the highest spin injection efficiency (up to 35%) [104]. In particular, it provides high spin-dependent resistance by avoiding the conductivity mismatch problem between the contacts and the graphene sheet, preventing the injected spins to diffuse back to the injector FM.

After the spin-polarized electron is injected to graphene (by one of the above injection techniques), the spin diffuses across the graphene channel and reaches the detector. In order to detect a pure spin signal, electrodes are arranged in what is called a "nonlocal geometry". That means that the charge current loop does not overlap with the detector (**Figure** 1.13**a**). As shown in **Figure** 1.13**a**, electrical current is injected through FM electrode, E2, and current under E2 diffuses to E1 (both spin current and charge current) and through graphene channel to the detector FM electrode, E3 (spin current only). Then the spin current is measured as a "nonlocal voltage" (V_{NL}) on E3. V_{NL} is positive or negative depending on the magnetization configuration of E2 and E3, parallel or antiparallel to each other. Parallel and antiparallel magnetization of two FM electrodes, with a different coercive field, occurs when an in-plane magnetic field (B) sweeps along the axis of the electrodes. For instance, sweeping the magnetic field from negative to positive results in switching first one electrode (E2 or E3) magnetization direction. If the initial magnetization configuration is parallel, it then switches to antiparallel (↑↑→↓↑). If the magnetic field keeps increasing, the second electrode switches and the parallel configuration is recovered (↓↑→↓↓). The difference between the negative and the positive voltages is called nonlocal (magneto)resistance, defined as $\Delta R_{NL} = V_{NL}/I$, where (I) is the injected current (**Figure** 1.13**b**) [98]. Usually, a small nonlocal baseline resistance is observed in experiments which could be due to leakage current and artifacts associated with a finite common-mode rejection of the voltage detector.

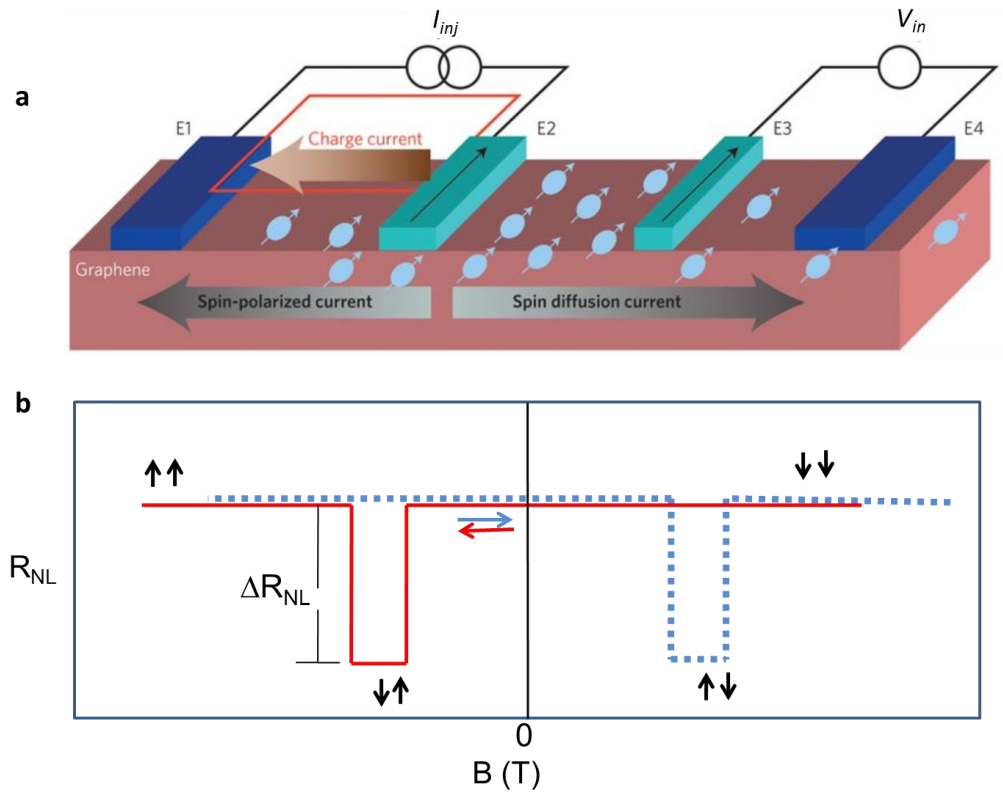

Figure 1.13. Spin injection, transport, and detection in graphene devices. **a**) Schematics showing the spin transport measurement for nonlocal geometry. Light blue symbols indicate spin-polarized electrons propagating across the graphene channel. E2 and E3 are ferromagnetic electrodes [98]. **b**) Schematics showing a nonlocal spin valve for different magnetization orientations as represented by arrows as the magnetic field is swept from negative to positive (blue) or positive to negative (red) values.

The other important characteristic of spin transport is the manipulation of the spin population in the channel, between injector and detector. Hanle precession is the commonly used technique to manipulate the spin precession as discussed below.

Spin precession experiments

Spin precession or Hanle effect is the measurement of spin precession in the presence of a magnetic field transversal to the initial spin direction. Spin precessing and dephasing occur in the transport channel around the applied out-of-plane external magnetic field (**Figure** 1.14**a**). The measured nonlocal resistance plotted as a function of an out-of-plane magnetic field is called the Hanle curve (**Figure** 1.14**b**). The spin lifetime τ_s, the spin diffusion constant D_s or the spin relaxation length λ_s are extracted by fitting the Hanle spin precession data to the solution of Bloch diffusion equation a follows:

$$\Delta R_{NL} \propto \int_0^{\infty} \frac{1}{\sqrt{4\pi D_s t}} e^{-\frac{L^2}{4D_s t}} \cos(\omega_L t)\, e^{-\frac{t}{\tau_s}} dt$$

$$\lambda_s = \sqrt{\tau_s D_s}$$

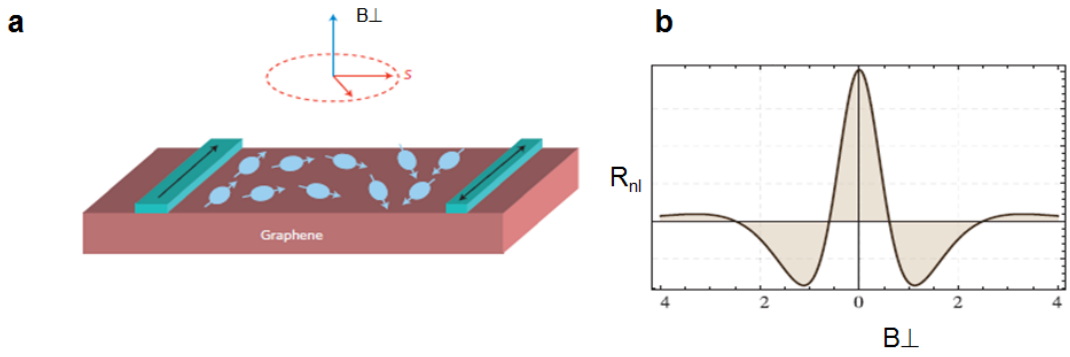

Figure 1.14. Hanle measurements: **a**) Schematics showing spin relaxation in graphene channel in the presence of an out-of-plane magnetic field [105], **b**) a Hanle curve plotted with nonlocal resistance as a function of a perpendicular magnetic field.

Spin relaxation

The lifetime of spin in any material is limited to a finite value due to spin scattering or spin relaxation. Common scattering mechanisms include the spin-orbit (SO) coupling and hyperfine interaction. Hyperfine interaction occurs due to the coupling between magnetic moments of the electrons and the nuclei and it is negligible in materials of zero magnetic moment such as (^{28}Si) and graphene (sue to the abundance of ^{12}C). SO occurs due to the coupling between orbital angular momentum and magnetic moment and its effect is highest for massive elements.

In conventional materials, there are two main mechanisms that have been commonly used to explain spin relaxation: Elliott-Yafet (EY) [106] and D'yakonov-Perel (DP) [107]. In the EY mechanism, the coupling of up and down spin state occurs in the presence of scattering centers such as impurities grain boundaries or photons. This mechanism is dominant mostly in metallic systems (with inversion symmetry of the crystal lattice). The spin dephasing probability increases as the number of scattering centers increases (or the momentum scattering time decreases). The D'yakonov-Perel mechanism illustrates that the spin dephasing occurs due to an effective magnetic field coming from systems that lack inversion symmetry in their crystal lattice. Therefore, the individual moving electron's spin precesses in the effective magnetic field until a momentum scattering occurs and after such scattering event the magnitude and precession angle change. Unlike EY mechanism in which spin relaxation occurs at the scattering event (spin scattering rate is directly proportional to momentum scattering),

in DP mechanism the spin relaxation occurs in between scattering events (the spin scattering rate is inversely proportional to the momentum scattering rate).

Chapter 2: Experimental and methodologies

In this chapter, all the experimental parts carried out in this thesis work are presented. The main experimental procedures include:

- Procedures for the growth of graphene on Cu foil using CVD techniques
- Procedures for the transfer technique of the grown graphene to the desired substrate
- Microscopic and spectroscopic characterization techniques for graphene characterization
- Procedures to fabricate graphene-based spin transport devices

2.1 General procedures for CVD growth of graphene

CVD growth of graphene involves a series of steps such as Cu foil preparation, preheating, annealing, growth and cooling steps as it was discussed in the introduction part. In this section, we present detail procedures for each of the steps that were used in this thesis.

2.1.1 Cu foil preparation/pre-cleaning

Cu foil preparation plays a key role to minimize the level of impurities and to smoothen the metal surface. In this thesis, we have used electropolishing techniques to remove the contamination from the surface of the Cu foil and to decrease the surface

roughness of the Cu foil. A Cu foil of 25 μm thick (99.8%, Alfa Aesar, stock #13382) was used for the experiments.

Cu foil was cleaned in acetone and isopropyl alcohol (IPA) for 10 min each to remove any oil, grease, dust, fingerprints or other potential impurities left after the manufacturing.

In order to remove surface oxides and other inorganic contaminants, the Cu oxide species were removed using acetic acid/water (1⁄3) and then thoroughly rinsed with DI water followed by blow-drying with nitrogen gas.

Finally, to make the surface smoother electropolishing procedures were applied using a phosphoric acid electrolyte. In detail, the workpiece of Cu foil was attached to the anode and another Cu plate to the cathode. The electrolyte was a combination of 150 ml of water, 75 ml of orthophosphoric acid, 75 ml of ethanol, 15 ml of isopropyl alcohol, and 1.5 g of urea. A 5 V was applied for 100s using a DC power supply. After electropolishing, the Cu foil was rinsed with deionized water and ethanol followed by blow-drying with nitrogen. Then the Cu foil was loaded into the growth setup.

2.1.2 Growth of graphene

Growth was performed using a (Lindberg/Blue M, Asheville, NC, USA) furnace and 1-meter long 1-inch diameter quartz tube. Two types of flow meters for methane gas were used; one for low flow rate and the other for a high flow rate of gases. Red-Y mass flow meters were used for the high flow of gases during the study of nucleation

density. For small gas flow, we used another flow meter (BRONKHORST HI-TEC, F-200CV-002-RGD-22-V) to grow more single-crystal graphene domains.

After placing the pre-cleaned Cu foil into the growth tube, the tube was purged for about 10 min in a vacuum before heating-up. The Cu foil was annealed in Ar (99.9992% purity) 450 sccm and H_2 (99.999% purity) 50 sccm at 1000 ^{0}C for 30 min. In some cases, O_2 was allowed to flow with 1 sccm for 2 min in the presence of Ar (450 sccm) and 0 sccm of hydrogen for oxidative passivation of the Cu foil.

Then graphene was grown in Ar 450 sccm, H_2 50 sccm and CH_4 1 sccm (99.995 %) at 1000 ^{0}C for various growth times depending on the objective of the experiment. After growth, the CH_4 was turned off and the system was fast cooled down to room temperature under Ar/H_2 atmosphere by taking the quartz tube out of the furnace. This helps to minimize the formation of multi-layer graphene patches under the first layer in the temperature range between 900-1000ºC range [108]. Unless specified, these were the standard growth conditions selected throughout the text. Specific procedures associated with different growth techniques were included in the respective chapters.

Flow meters

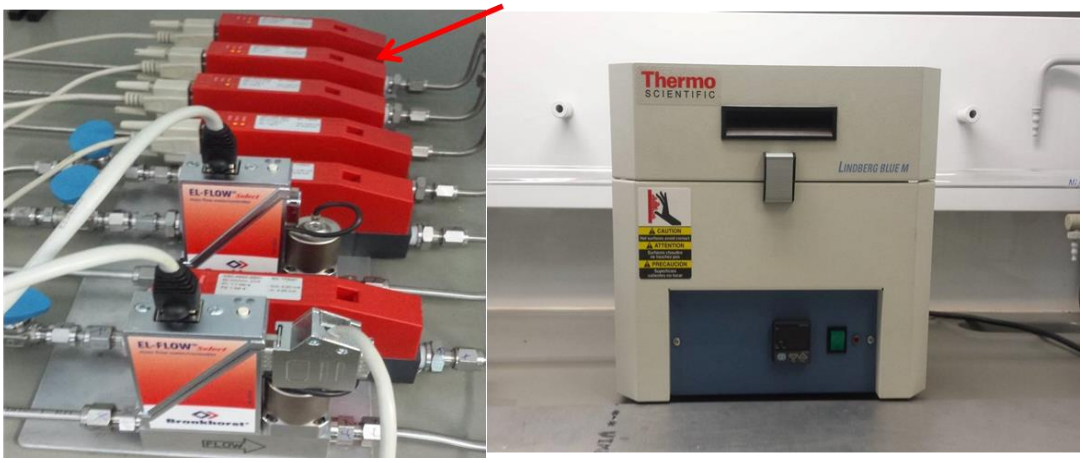

Figure 2.1. Growth system: The flow meters (right panel) and the growth furnace (left panel).

2.2 Transfer of graphene onto SiO_2/Si and TEM grid

Graphene transfer to the desired substrate is a crucial step towards the development of electronic devices. The most commonly used transfer method relies on the use of polymethyl-methacrylate (PMMA) as on-top support which prevents the graphene film from folding and breaking during the transfer process. In this thesis, we used PMMA support transfer techniques to achieve clean graphene for high-performance spintronic devices.

The PMMA support transfer is schematized in **Figure** 2.2 PMMA (A4 950 K) was spin-coated on Cu/graphene layer at 4000 rpm for 40 seconds (3x) followed by air-drying overnight. Graphene on the PMMA uncoated sides of the Cu foil was removed by floating it on 20% nitric acid solution for about 2.5 min followed by rinsing with

deionized water. Then the Cu was etched using a 0.25 M $(NH_4)S_2O_8$ solution and rinsing with deionized water (3x), 10 % HCl and then again with deionized water (2x). The PMMA/graphene was fished out from deionized water using the desired substrate (e.g. SiO_2/Si or TEM grid), dried and cured at 85 ^{0}C for 30 min. The PMMA is removed by dipping the PMMA/graphene stack inside hot acetone at 50 ^{0}C for 30 min and rinsed with isopropanol alcohol followed by nitrogen blow-drying.

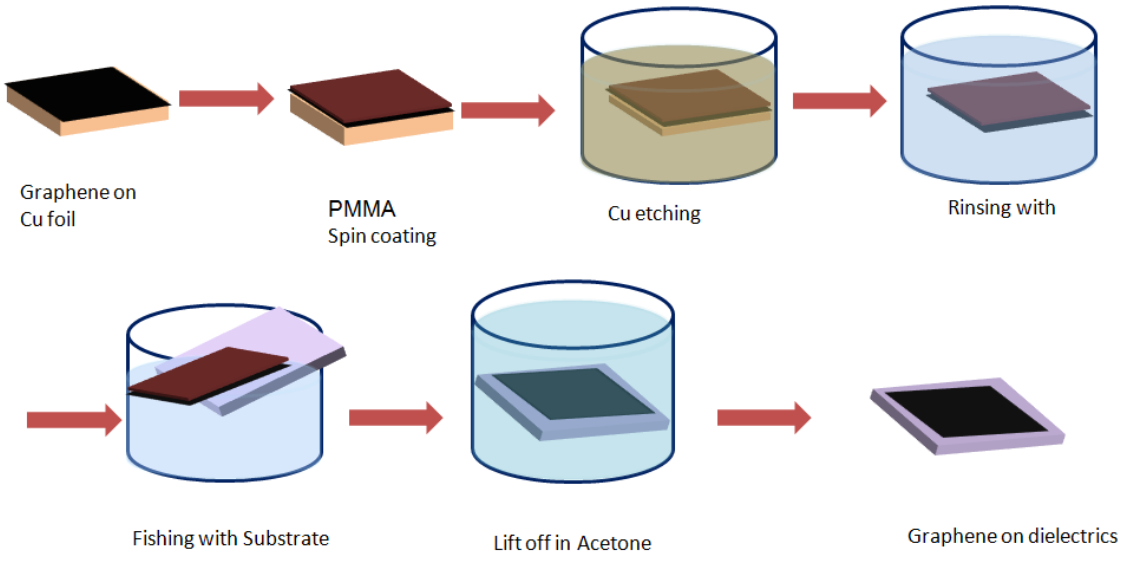

Figure 2.2. Schematics illustrations of the main steps involved in the PMMA-assisted transfer of graphene onto a dielectric substrate.

2.3 Characterization of graphene

Graphene quality determination involves both structural and electrical characterization, which help us to determine the cleanliness, number of layers, crystallinity and electrical properties of the graphene film. There are several structural characterization techniques for the as-grown and transferred graphene.

In this thesis, as described in chapter 1, structural characterization of graphene was carried out using optical microscopy, scanning electron microscopy (SEM), transmission electron microscopy (TEM), atomic force microscopy (AFM), Raman spectroscopy and X-ray photoelectron spectroscopy (XPS). The electrical characterization was carried out using a DC reversal technique with a Keithley 2182 nano voltmeter and a 6221 current source.

2.3.1 Structural characterization

Optical microscope: Optical microscope imaging was carried out both on as-grown graphene on Cu foil and after transferred to a 440 nm SiO_2/Si substrate. Optical microscopy can roughly determine the quality and the number of layers of the graphene film. The later is determined by considering the contrast difference between the layers of graphene on SiO_2 substrate.

An optical microscope (Nikon Eclipse LV100ND) (**Figure** 2.3**a**) was used to observe the domain size and shape, and degree of coverage when the Cu foil was not fully covered by graphene. The graphene/Cu foil was heated on a hot plate at 180-200 ^{0}C to identify the graphene on the Cu foil. The Cu surface free from graphene changes color due to oxidation while the graphene covered Cu foil remains unchanged which helps to identify graphene flakes by color contrast (**Figure** 2.3**b**). The quality, level of residue left and number of layers of our CVD grown graphene were also determined after transferring onto SiO_2 substrate (**Figure** 2.3**c**). During device fabrication, optical

microscopy was used to select clean regions and to observe the quality of graphene at each device fabrication step.

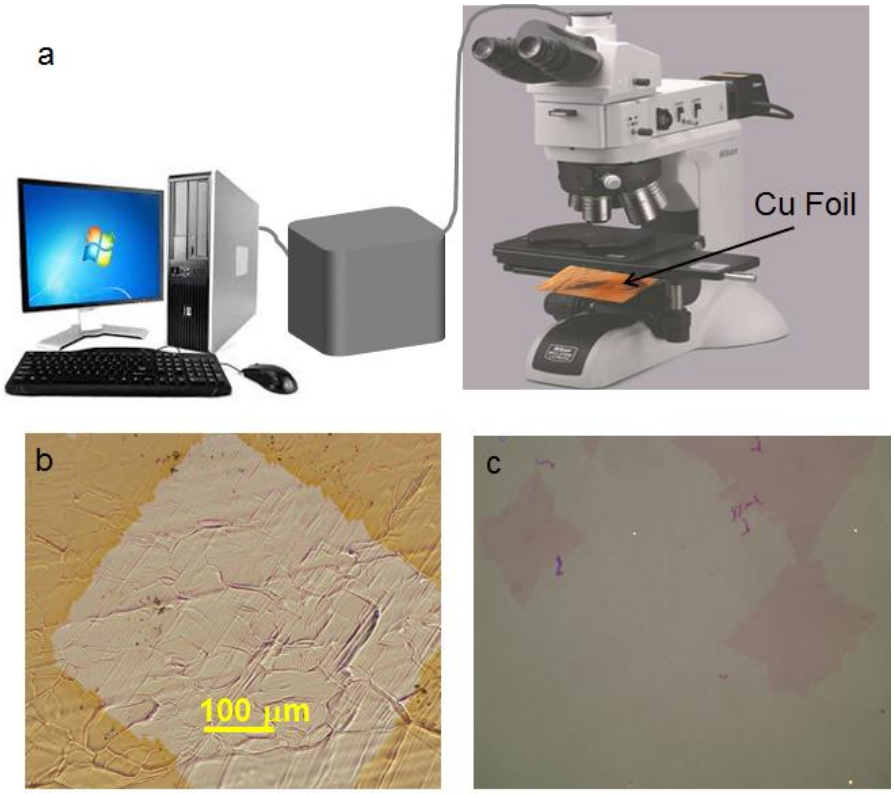

Figure 2.3. Optical microscope characterization. **a**) Optical microscopy set-up, **b**) optical image of as-grown graphene on a Cu foil and **c**) optical image of graphene transferred onto 440 nm SiO_2/Si.

Scanning electron microscope (SEM): In this thesis, we used a high-resolution SEM (Magellan 400L XHR) to characterize graphene domain morphology (**Figure** 2.4**a**). The SEM was operated at an acceleration voltage of 5 kV to image graphene domains. Device fabrication was carried out using a SEM (Inspect) connected to a lithography pattern generator controlled by a Raith ELPHY Quantum interface.

Transmission electron microscope (TEM): In this work, we used a high-resolution TEM (HRTEM FEi Tecnai G2 F20) operated at 200 kV to image graphene on a TEM grid (**Figure** 2.4**b)** and determine the crystallinity of the CVD grown graphene flakes (**Figure** 2.4**c)**. The graphene was transferred onto TEM grid with the same procedure reported in reference [109].

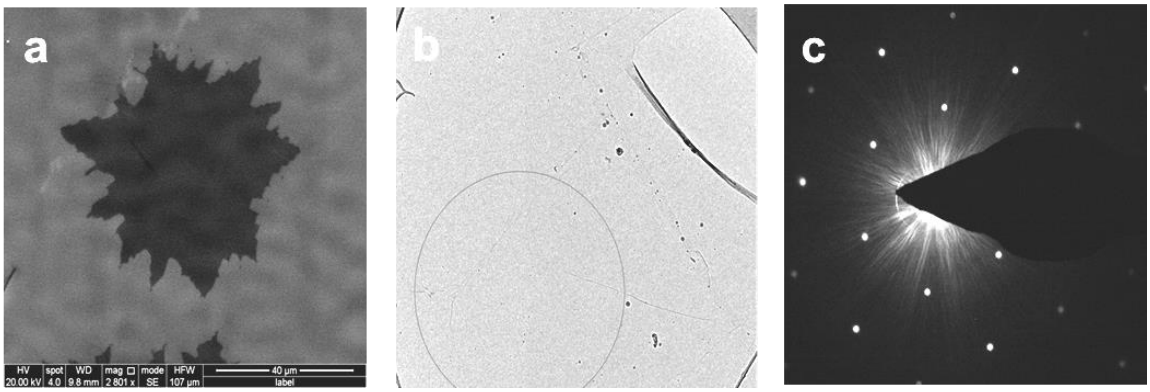

Figure 2.4. Electron microscope characterization of graphene: typical **a**) SEM image of as-grown graphene on Cu foil with an etched pattern at the edges of the graphene domain **b**) TEM image of graphene membrane on TEM-grid hole **c**) electron diffraction patterns from graphene membrane showing a single-crystalline structure.

AFM characterization: AFM (Bruker Veeco Dimension 3100 nanoscope-V) was used to determine the morphology and thickness of the CVD grown graphene film. We also used it to visualize the level of polymer residues on top of graphene flake after patterning by lithography steps. **Figure** 2.5 shows a typical AFM image of a) CVD graphene on SiO_2 substrate and b) graphene strip after device fabrication. Graphene folding and polymer residues can be easily distinguished in (**Figure** 2.5**a)** as well as the ripples on the graphene after device fabrication (**Figure** 2.5**b)**.

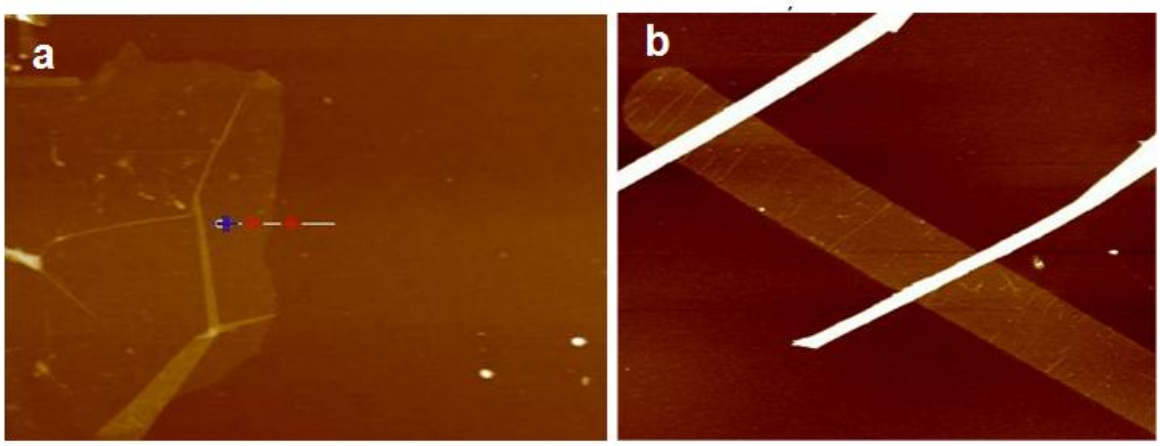

Figure 2.5. AFM image of graphene on **a**) transferred onto SiO_2 and **b**) strip of graphene after device fabrication (white strips are the metal electrodes).

Raman Characterization: We used Raman spectroscopy (Horiba T64000 Raman spectrometer, 532 nm laser) to determine the number of layers and defect density of graphene film by considering the three characteristic Raman peaks introduced in chapter 1. The Raman spectroscopy characterization was implemented after graphene was transferred onto SiO_2/Si using PMMA support transfer. As observed in **Figure** 2.6, the typical CVD grown graphene samples show characteristic peak positions and peak intensities for monolayer graphene with some defects which could be created during the transfer process.

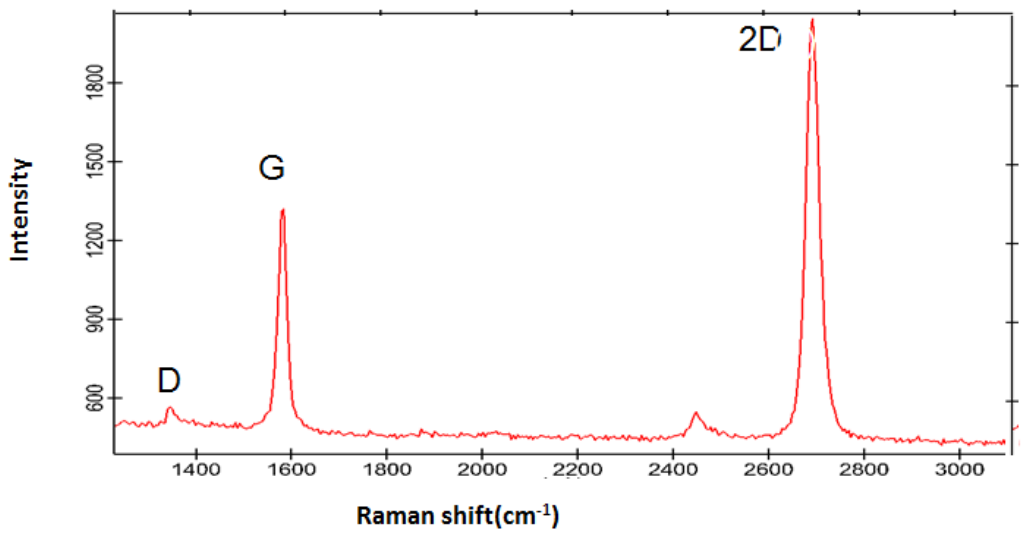

Figure 2.6. A typical Raman spectrum for monolayer graphene involving the three characteristic peaks (D, G, and 2D peaks).

XPS characterization: XPS with monochromatic AlKα radiation (1486.6 eV) and PHOIBOS150 hemispherical analyzer hosted in a UHV system with a base pressure of $5x10^{-10}$ mbar was used to determine the surface chemistry of Cu foils after photo-assisted thermal annealing and only thermal annealing processes. The XPS characterization was performed with *ex situ* XPS experiments in which the Cu foil was first annealed and then transported to the XPS system in ambient conditions. This experiment helped us understand the surface chemistry of the Cu foil during the annealing steps.

Briefly, the experiment was carried out by first cleaning the Cu foil in acetone and IPA followed by electropolishing. Then the Cu foil was annealed at 1000^0C in the presence of argon and hydrogen gases (without laser light) for 30 min followed by

another 30 min annealing in the presence of laser light. After 60 min annealing (30 min without and 30 min with laser) the system was cooled to room temperature under argon and hydrogen atmosphere. The same experiment was performed with only thermal annealing for comparison. Then, the photo-assisted thermal annealed and only thermal annealed Cu foils were placed into the XPS system for surface chemistry analysis. Specific procedures will be mentioned in the respective sections.

2.3.2 Fabrication of device from CVD graphene

CVD grown graphene film transferred onto SiO_2/Si was used to fabricate spintronic devices. The transferred graphene was cleaned with acetone and isopropanol. The cleanest regions were selected using an optical microscope. Then the graphene was spin-coated with MMA/PMMA (5000/2500 rpm, 40 sec 1min/5 min bake at 180 - 200 ^{0}C). Markers were patterned on the selected regions using EBL and then Ti/Au (4nm/35nm) was deposited using e-beam evaporation. Strips of graphene were patterned inside the marked regions using negative resist-based lithography. To expose the selected pattern, MMA was spin-coated (5000 rpm, 40s, and baked at 130 ^{0}C for 10 min) and then negative resist AR 7520.17 was spin-coated (4000 rpm, 60 s, and baked at 85^{0}C for 2 min) on top of the MMA coating. The resists located on the selected graphene strip were exposed using EBL (10 keV, 2.5 spot size, 0.3 dose factor, 5 aperture). The patterns were developed using a negative resist developer (AR-300-47, for 2 min and 30 sec, rinsed with DI water for 1 min). After developing the pattern, the rest of the graphene/MMA stack was removed using oxygen plasma with 200W power for about 40 s (10s X 4)

leaving only the pattern consisting of graphene/MMA/negative resist on the exposed strip. Then the resist layer on the exposed strip was removed by dipping the sample in acetone to get the free graphene strip. The resulting graphene strips were annealed in a furnace under high vacuum (10^{-8} Torr) for 3 hours at 500 ^{0}C to remove contaminations/residues leftovers from the transfer and lithography process. After that, ferromagnetic cobalt electrodes with tunnel barriers were defined by electron beam lithography using a PMMA/MMA bilayer mask. A 8 Å titanium oxide layer as a tunnel barrier was deposited prior to the evaporation of 30-nm thick cobalt to achieve efficient spin injection. **Figure** 2.7 shows the main steps of device fabrication.

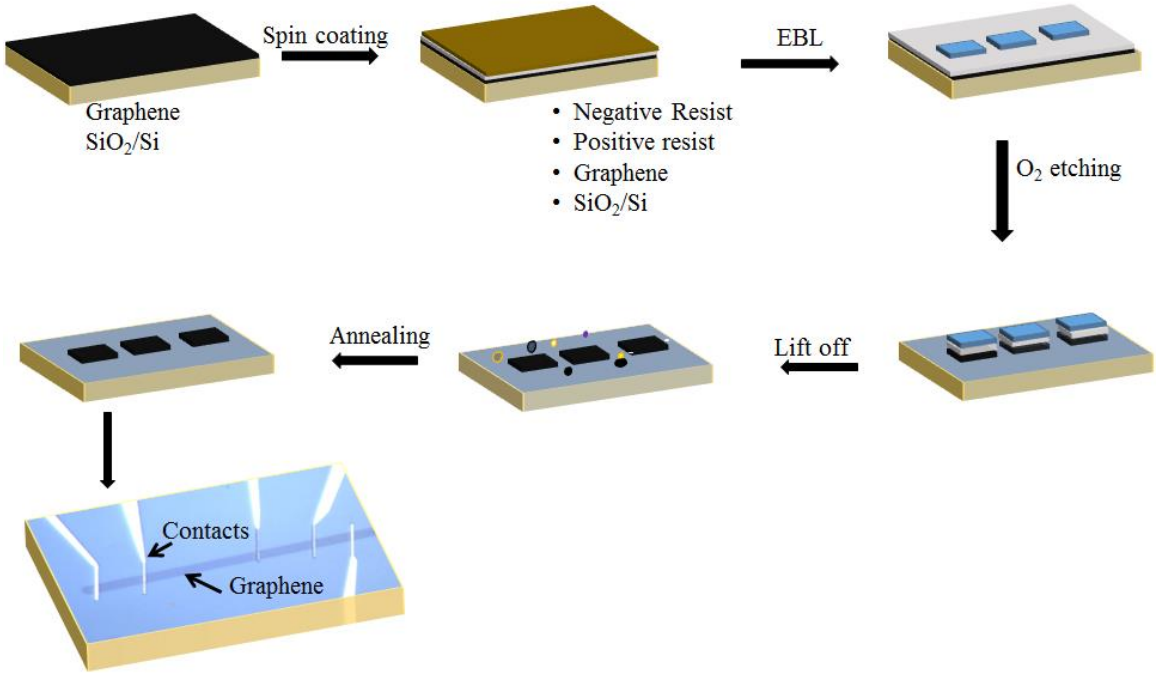

Figure 2.7. Scheme for the fabrication of graphene devices from CVD graphene.

2.3.3 Charge transport measurement

In order to characterize the electrical and spintronic properties, the contact pads of the fabricated device were wire-bonded to a gold-coated chip carrier with a 25 μm thin aluminum wire using a wire bonder (Westbound). The electrical resistance of graphene was recorded using four-probe measurements to acquire directly the resistance of the device without the involvement of the resistance of the contacts. In brief, the bias current was applied to the two outer electrodes and the voltage drop was measured on the other two inside electrodes as shown in the following figure. The process was repeated for all pairs of electrodes to characterize the variation of the resistance and doping along the graphene strip.

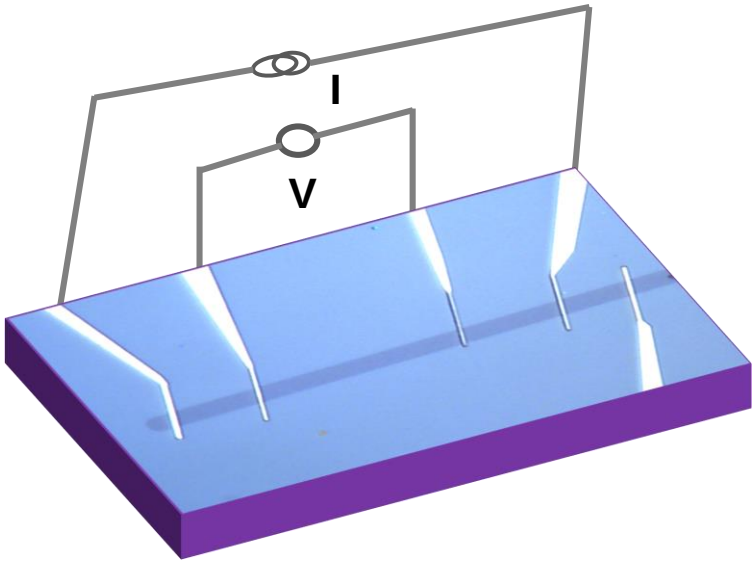

Figure 2.8. A typical four-probe configuration for the determination of the resistance of the graphene flake without the interference of the contacts.

2.3.4 Spin transport measurement

We have also measured the nonlocal spin valve (NLSV) and Hanle effect using four-point configurations. In these cases, the current was injected between the two electrodes on one side and the voltage was detected on the two electrodes of the other side. No current flows on the detector electrodes, rendering the measurement "nonlocal". In order to measure the NLSV, the magnetic field was swept along the ferromagnetic electrodes while for the Hanle experiments, the magnetic field was swept perpendicular to the graphene plane. A back gate voltage was applied to measure the mobility of the graphene at different carrier concentrations. We have used a Keithley K6221 AC/DC current source to apply current, a Keithley K2182 nanovoltmeter to read the voltage output and either a Keithley K2400 or Keithley 230 voltage source to apply the back gate voltage. A computer program written with Lab VIEW (National Instruments) was used for instrument control, data processing, and acquisition.

Chapter 3: Effect of the in-situ rise of hydrogen partial pressure on the CVD graphene growth

Under the context of achieving a controlled growth of high-quality graphene, this chapter aims at understanding the complex role of hydrogen as one of the key parameters in the CVD growth. In particular, we demonstrate the etching effect deriving from an *in-situ* rise of hydrogen partial pressure on the general morphology of the graphene domains. Indeed, we observe a change in the shape of the growing graphene from compact to dendritic with growth time. The takeover of the dendritic structure is ascribed to an increase of the residual hydrogen over time, which leads to a competing backward reaction (etching). The influence of the inverse reaction during growth has been normally disregarded but it is very important to establish the conditions at which this effect is promoted since it can be also a source of structural defects on the on-grown graphene. We have performed a systematic study as a function of growth time to identify the onset and gradual evolution of graphene shapes caused by etching and then demonstrated that the etching can be stopped by reducing the flow of hydrogen from the feed. In addition, we have found that the etching rate due to the *in-situ* rise in hydrogen is strongly dependent on the (geometrical) confinement of the Cu foil. Highly etched graphene with dendritic shapes was observed in unconfined Cu foil regions while no etching was found in graphene grown in a confined reaction region. This highlights

the effect of the dynamic reactant distribution in activating the etching process, which needs to be counteracted or controlled for large scale growth.

3.1 Introduction

As mentioned in the introduction, graphene is a very suitable material for long spin lifetime and long spin diffusion length. However, such applications require the production of high-quality single-crystal graphene film with extremely high reproducibility. Despite continuous progress, CVD grown graphene, covering wafer size areas, is typically polycrystalline comprising small grain sizes which cause deterioration of the physical and chemical properties. Considerable efforts have been made to grow single-crystal isolated graphene flakes with a variety of shapes [51], [58], [110]–[112]. The graphene domain shapes can be controlled by tuning the growth conditions. For example, compact and dendritic structures are determined by the growth pressure [113], the hydrogen/methane (H_2/CH_4) ratio [114], [115] and the growth temperature [49], [116]. Such intrinsic complexity of CVD growth has led to a large spread of experimental results, even when using similar nominal growth conditions.

In particular, dendritic structures have been reported by several groups under different growth conditions. The microscopic mechanism leading to these structures has been a subject of debate. They have been ascribed to the kinetics of carbon flux attachment to the carbon edges, the anisotropic surface diffusion due to the underlying crystallinity [116] or to the degree of roughness [117] of the Cu foil and to a surface

diffusion-controlled growth mechanism arising from the limited amount of carbon source [118]. Remarkably, similar dendritic shapes have been also achieved by etching the CVD grown graphene after growth (post-etching) [119], [120]. In those experiments, graphene was first grown following a standard procedure using a CH_4 in Ar/H_2 gas mixture, then the CH_4 was switched off and, finally, graphene was etched with Ar/H_2. In other reports, gaseous oxidants were considered to be the main responsible for graphene etching, giving place to lines and holes with hexagonal shapes [121].

All of the above reports, which focus primarily on either growth or etching mechanism of graphene, have been seemingly disconnected. However, the CVD growth of graphene actually involves a competition between growth and etching [122]. It is thus possible that the dendritic shapes might not be only the result of a surface diffusion-controlled growth mechanism but also of an etching takeover over time without modification of growth conditions. Therefore, understanding the origin of the dendritic shapes is critical to gain insight into the dynamic processes involving growth and etching during deposition, which has often been ignored, and can also lead to novel approaches to further develop CVD growth.

In this chapter, we demonstrate a distinct mechanism that gives place to dendritic shaped graphene, which has not been discussed before. We observe that the dendritic shape is formed within a given growth process promoted by the etching takeover at long growth times. We have studied systematically the shape evolution of the graphene flakes at shorter times under the same growth conditions. We have found that, indeed, after initial growth, the competing backward etching starts dominating, shaping the graphene

into dendritic structures. We have ascribed the etching and formation of dendrites to an *in-situ* rise of H_2 partial pressure during growth. We also show that the confinement of the Cu foil impacts on the growth/etching balance. The etching is selectively observed in unconfined regions. This is a very important finding since it can be an additional source of heterogeneity that must be taken into consideration for explaining the wide dispersion of results among research groups. In addition, by tuning the amount of H_2 after a standard growth period (before etching starts to dominate), we demonstrated that oxidative etching coexists with the reductive etching mediated by the *in-situ* rise of hydrogen partial pressure. The previously observed oxidative etching [121] becomes evident at low H_2 flow rates and is characterized by the formation of hexagonal holes carved into the graphene flakes.

3.2 Results and discussion

3.2.1 Investigation of growth mechanism

Figure 3.1 and **Figure** 3.1**b** show an optical microscope and scanning electron microscopy images of graphene on Cu foils grown during 60 minutes with the standard growth conditions specified in the experimental part. As seen in **Figure** 3.1**a** and **Figure** 3.1**b**, the graphene domains have a dendritic structure and cover an area with a hexagonal shape. These results were similar to those in previous reports, which were ascribed to an anisotropic growth [116]. The flakes were also similar to those reported in

post-growth hydrogen-assisted etching [119], [120]. The outcome of some selected reports is tabulated in Table 3.1.

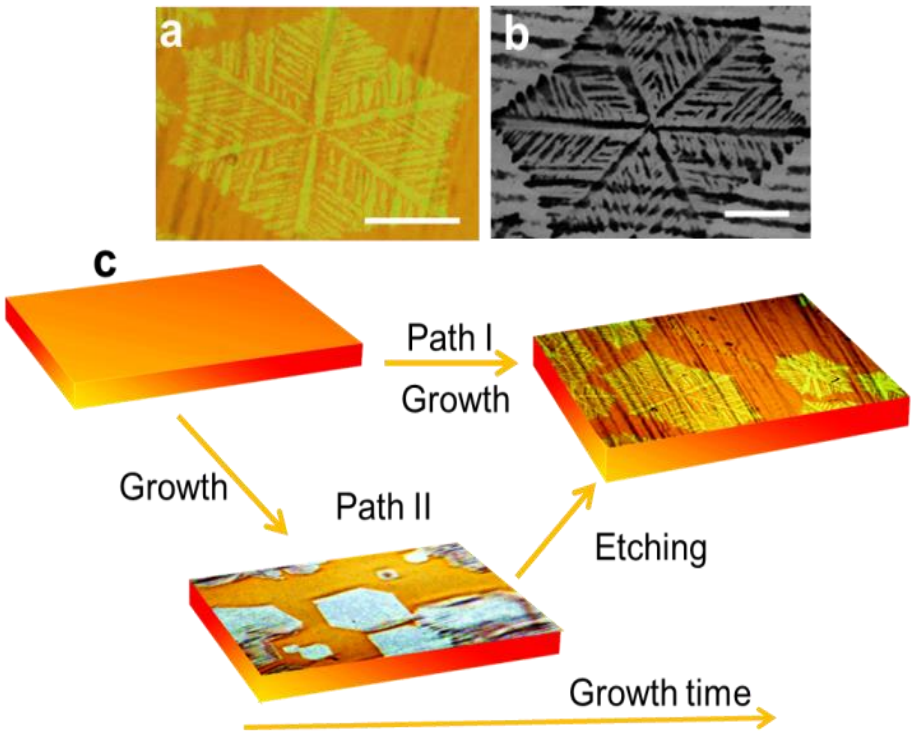

Figure 3.1. **a**) Optical and b) SEM image of graphene on a Cu foil grown for 60 min. c) Scheme showing the two possible pathways leading to the final graphene structure. In prior work, the direct growth of dendritic shapes was reported (Path I). We propose that the same structures can be obtained from a two-step mechanism (Path II) consisting of growth and subsequent etching. The scale bars are 50 μm.

As illustrated in **Figure** 3.1**c**, we propose two possible paths for the resulting dendritic graphene shape: growth or growth followed by etching. That is, the flake morphology could be:

I. the outcome of surface-diffusion limited growth (growth outcome) as in previous reports [116], [117] **Figure** 3.1**c** Path I) or

II. The result of a competing etching process (etching outcome) that dominates after a certain growth time under the same growth condition (**Figure** 3.1**c** Path II).

It is, therefore, important to discriminate these two mechanisms in order to gather a better understanding of the CVD graphene growth process. For this purpose, we performed a time-dependent growth experiment.

Table 3.1. Reported literature for dendritic flake outcome: dendritic flakes from surface-diffusion limited growth process (refs. [116]–[118], from hydrogen post-etching [17] and from growth to etching transformation due to an *in-situ* rise of H_2 at longer growth time (our result).

Morphology	Mechanism and process conditions	Size of flakes	Process time
Flakes with dendritic edge [116]	Growth with controlled CH_4/H_2 ratio	Not specified	Not specified
Flakes with dendritic edge [117]	Growth with controlled CH_4/H_2 ratio	70 μm	15 min growth
Flakes with dendritic edge [118]	Growth at low CH_4/H_2 ratio	100 μm	30 min growth
Flakes with etched edge[17]	H_2 post-etching (fractal etching) after growth	Not specified	30 min growth and 5 min post-etching
Flakes with a dendritic edge (Our result)	Growth to etching transformation due to *in-situ* rise of H2 with time	Few 100 microns	20 min growth followed by time-dependent etching

3.2.2 Time-dependent graphene shape evolution

In order to verify if path II was possible, we varied the growth times to determine the evolution of the graphene domain shape. **Figure** 3.2 and **Figure** 3.3, respectively present the optical and SEM image of the graphene grown for different growth times. **Figure** 3.2**a** and **Figure** 3.2**b** show optical microscope image of graphene grown at 10 min and 60 min, respectively. **Figure** 3.3**a** to **Figure** 3.3**e** show a series of SEM images of typical individual flakes on Cu foil for growth times of 10, 20, 25, 30 and 60 min.

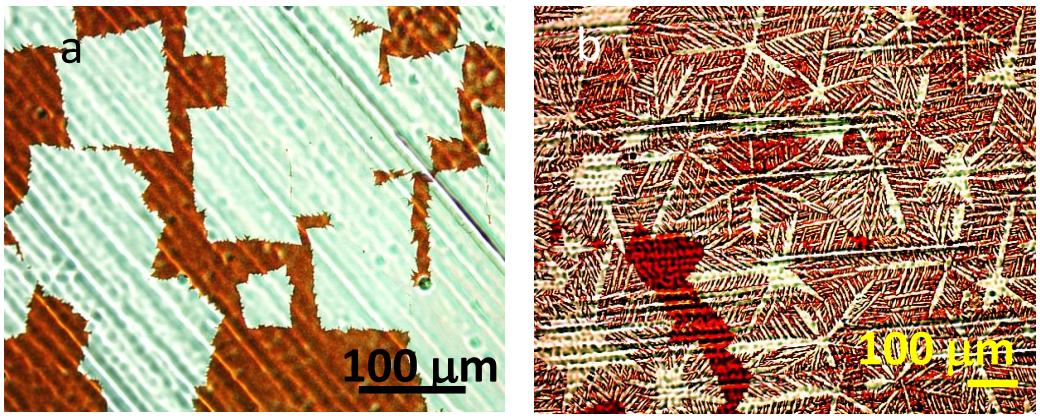

Figure 3.2. Typical optical microscope images of graphene (white color) on Cu foil showing the effect of growth times: a) graphene grown for 10 min showing unetched graphene and b) graphene grown for 60 min showing etched graphene.

The size and shape distributions of graphene were highly reproducible for independent growth experiments. We clearly observe that the flakes grow rapidly without dendritic shape for growth times of up to 10 min as observed by optical microscope (**Figure** 3.2**a**) and SEM (**Figure** 3.3**a**).

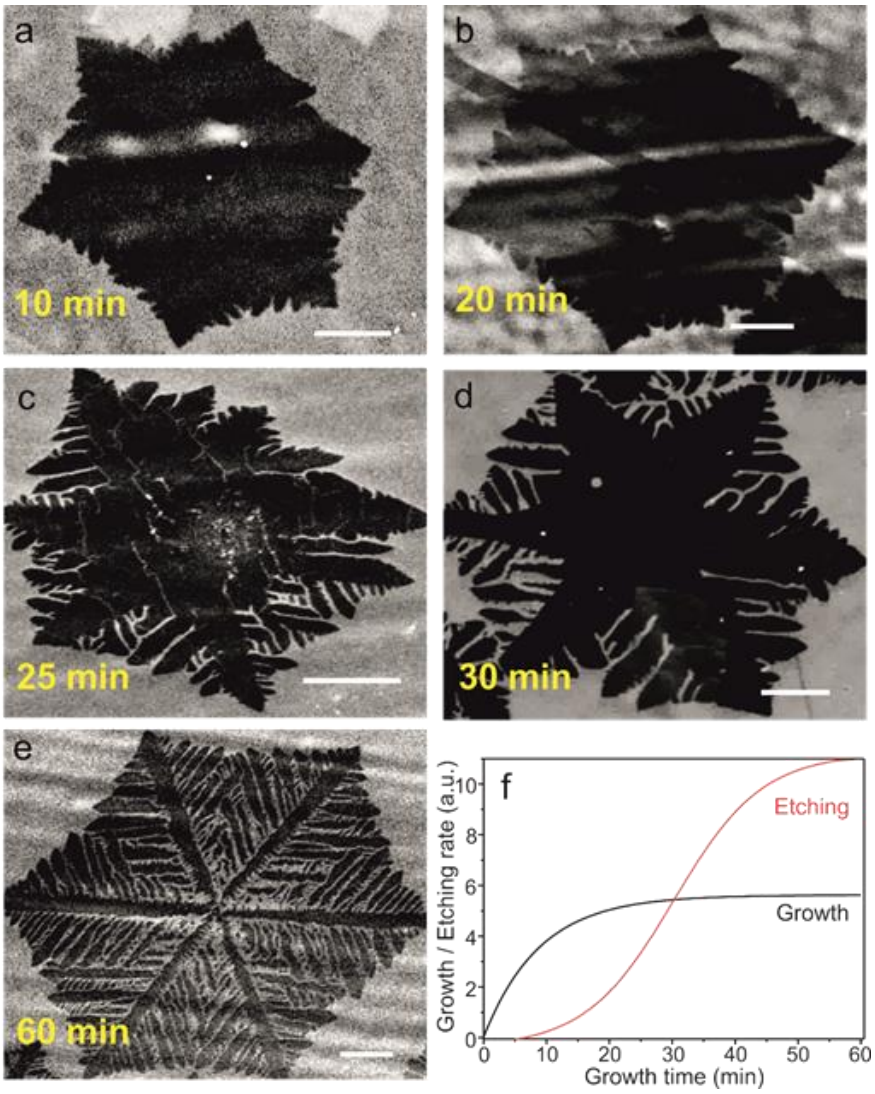

Figure 3.3. SEM images depicting the evolution of the graphene flake shapes (darker region for graphene) at different growth times **a**) 10 min **b**) 20 min, **c**) 25 min, **d**) 30 min, **e**) 60 min. The scale bars are 25 µm. **f**) Qualitative diagram showing the growth (black line) and etching (red line) profile, which explains the results in **a**)-**d**). At short times (<15 min), the flakes grow rapidly, as the etching process is slow. As the etching time increases, the growth slows down. The dendritic structure appears at times >20 min when the etching takes over.

Between 10 and 20 min, the growth slows down significantly. At 20 min, the size of the flakes barely increases (**Figure** 3.3**b**). Remarkably, at 25 min and longer times, a dendritic shape of the flakes becomes evident, which indicates a progressive takeover of an etching process **Figure** 3.3**c** to **Figure** 3.3**e**). The growth/etching competition is qualitatively represented in **Figure** 3.3**f**, where a growth zone and an etching zone are identified. In the initial growth zone, up to about 10 min, etching must be negligible, leading to a fast increase of the graphene domain size. However, at times beyond 10 min, the etching becomes significant enough to counteract the growth, as demonstrated by the small overall increase of the domain size. When the growth time exceeds 20 min, the etching takes over and the flakes start changing to dendritic shapes.

As advanced previously, our growth results (growth followed by etching) have similarities with previous studies in which graphene was carved after growth with the addition of external doses of hydrogen [119], [120]. Therefore, the gradual increase of the etching process with the resulting dendritic shape of the graphene domains suggests that the H_2 partial pressure exceeds the required amount for growth and the CVD dynamics is shifted to etching. Since the H_2 flows from the feed is constant, a non-negligible amount of H_2 must accumulate in the reaction path during growth. We ascribe this observation to an *in-situ* rise of hydrogen partial pressure resulting from the decomposition of methane and the difficulty to pump-out the light hydrogen molecules from the furnace. Indications of the local increase of H_2 with growth time have been also observed in a recent paper [123]. In our experiment, the excess H_2 enhances graphene

etching from the edges: because the chemical reactivity of carbon atoms at the edge of graphene is higher than the perfectly bonded carbon atoms in the basal plane [124].

3.2.3 Systematic control of hydrogen etching

We performed a series of experiments in the etching zone in which we reduced the external flow rate of H_2. The purpose was to compensate for the *in-situ* rise of the H_2 partial pressure during growth and thus reduce the etching that was induced by it. In each of the experiments, we first grew graphene for 20 min with the standard parameters, and then we decreased the H_2 flow rates from 50 sccm down to 30, 20, 10, 5, and 0 sccm for additional 10 min keeping the other parameters constant (Ar 450 sccm, CH_4 1 sccm). For further comparison, we performed an additional experiment in which the H_2 flow rate was increased to 60 sccm. **Figure** 3.4**a** to **Figure** 3.4**f** show typical SEM images of the resulting graphene flakes. These images should be compared with those in **Figure** 3.3**d** where the H_2 flow rate is kept constant for 30 min. For 60 sccm, we observe that the etching process is very aggressive leading to an almost complete disappearance of the flakes (**Figure** 3.4**a**). The etching appears to carve holes as in the case of high H_2 flow in Ref. [17]. As the H_2 flow decreases, we observe dendritic etching, which then decreases gradually as the flow rate of H_2 decreases further (**Figure** 3.4**b-e**). These findings demonstrate that the dendritic-like etching is driven by an *in-situ* rise of H_2.

At 10 sccm the etching process exhibits a combination of hexagonal hole-led and dendritic-type etching (**Figure** 3.4**e**), which suggests a transition in the etching mechanism. Notably, for a flow rate of 5 sccm and below, dendritic etching is no longer

present. In contrast, the graphene flakes exhibit hexagonal holes (**Figure** 3.4**f** and **Figure** 3.5**a**) that are reminiscent of the etching in an oxidant environment [120].

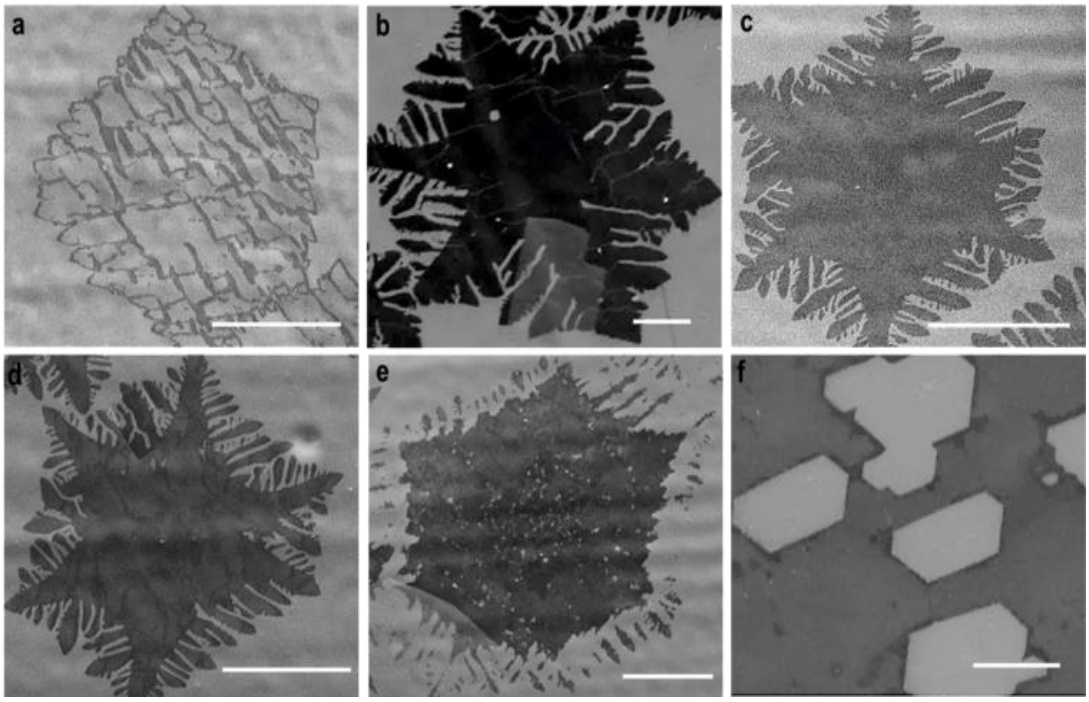

Figure 3.4. Etching profiles for 20 min with the standard growth method followed by an additional 10 min growth with reduced H_2 flows. The SEM images (darker region for graphene) depict the transition from high to low hydrogen flow. **a**) 60 sccm: graphene shape is strongly etched at high hydrogen flows. **b**) 50 **c**) 30 and **d**) 20 sccm: dendritic etching rate decreases gradually in the sequence, **e**) 10 sccm: hole etching starts to be observed in the entire part of the flake, **f**) 5 sccm purely oxidative etching. The scale bars are **b**-**e**) = 25 µm and **f**) = 10 µm**.**

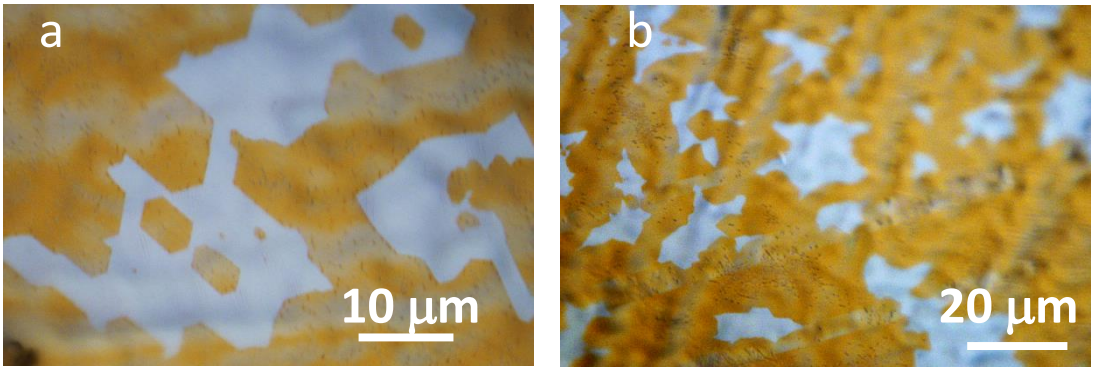

Figure 3.5. Optical images of oxidatively etched graphene. First, graphene is grown during 20 min with the standard protocol followed by an additional 10 min growth but at reduced hydrogen flow. **a**) 5 sccm H_2 showing an anisotropic etching with hexagonal holes and **b**) 0 sccm H_2, the graphene is aggressively etched with the oxidative environment but still has a sign of anisotropic etching. Whiter regions are graphene.

We interpret the transition to oxidative etching as follows. Besides acting as an activator of the surface-bound carbon and as an etching reagent, H_2 plays a role in neutralizing oxygen-based species, which could originate either from oxygen-based impurities in the feedstock gases or be already present in the furnace [120]. At low H_2 flows, the concentration of H_2 is not high enough to fulfill such a role, triggering the oxidative etching mechanism. At 0 sccm the etching is so aggressive that the graphene flakes are almost completely etched away from the Cu foil via hole-led etching (**Figure** 3.5**b**).

Interestingly, and in line with previous studies [120], the oxidative etching yields anisotropic hexagonal etched patterns that are aligned with each other, which could be used as evidence that the grown graphene features single crystalline structure [125],

[126]. The crystal structure of graphene domains was further confirmed by selected area electron diffraction (SAED), with a high-resolution TEM (HRTEM) as shown in **Figure** 3.6**.** For TEM measurement the graphene grown during 10 min was transferred onto TEM grid by the same procedure mentioned in chapter 2. **Figure** 3.6**a** shows an optical microscope image of the as-grown graphene on Cu foil. **Figure** 3.6**b** depicts a TEM image of hexagonal graphene flake after transferred onto the TEM grid with corresponding SAED at different regions of the flake. The electron diffraction patterns of the domain show single-crystalline nature, with the same orientation.

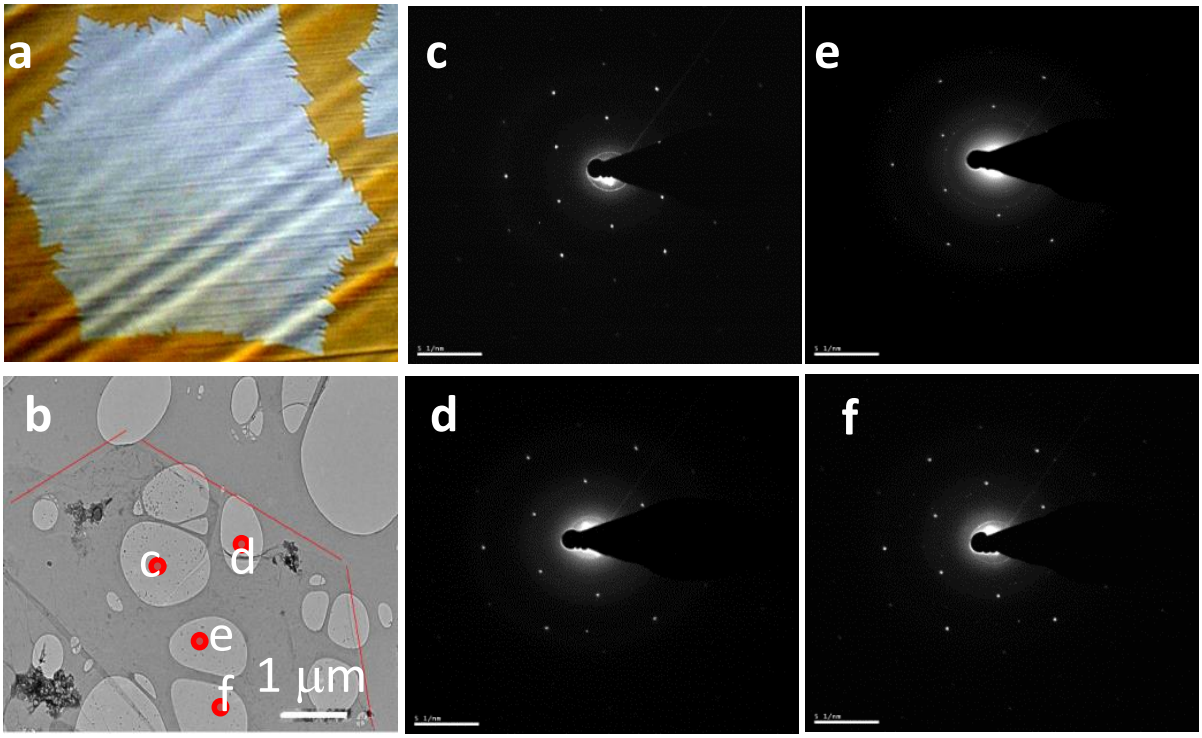

Figure 3.6. TEM analysis for typical graphene grown for 10 min. **a**) Optical microscope image of hexagonal graphene on Cu foil, **b**) TEM image on TEM grid and **c-f**) representative SAED patterns of single-domain graphene at the four different positions indicated in **b**).

Additionally, In order to characterize the graphene flake homogeneity, we performed Raman spectroscopy for a typical graphene flake grown at 20 min at three different flake locations. The Raman spectra showed similar profiles (**Figure** 3.7**a** and **Figure** 3.7**b**). We chose three points randomly on the flake **a**) and obtained the Raman G peaks at around 1585 cm^{-1} and the 2D peaks at around 2683 cm^{-1}. The presence of a small D peak below 1400 cm^{-1} could be associated with transfer related wrinkling.

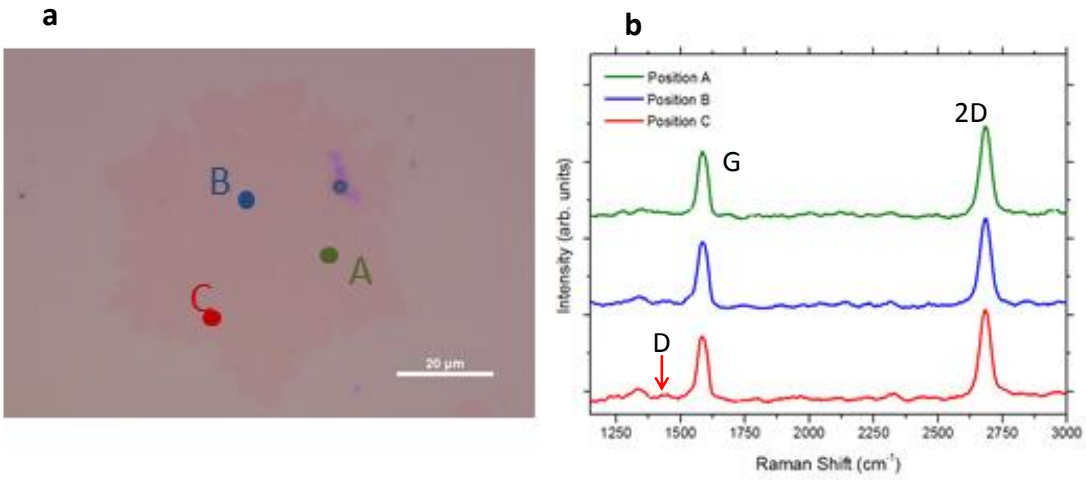

Figure 3.7**.** Raman spectra of a typical graphene flake. **a**) Optical image of a graphene flake grown during 20 min and transferred to SiO_2/Si (440 nm)), **b**) Raman spectra at 300 K for the graphene flake depicted in **a**) at points A,B,C showing the uniformity of the flake in the entire region.

3.2.4 Effect of confinement of the Cu foil on the induced etching

The confinement of the Cu foil is known to play a significant role in determining the local partial pressure of gasses species [50], [127], [128]. It is, therefore, likely that

confinement also impacts the growth/etching competition process. Considering this, we examined the inhomogeneities of the *in-situ* H_2 rise in different regions of the Cu foil by observing the local graphene etching level. We bent the Cu foil into two parts to make half part vertical (unconfined) and half part horizontal (confined). The horizontal part is sandwiched between a quartz glass slide and the quartz substrate holder (**Figure** 3.8**a**). Due to the difference in confinement and exposure to the gas flow, we expect differences in the etching process during the 60 min growth time. **Figure** 3.8**b** shows a large area SEM image that covers both vertical and sandwiched regions. Even in such large scale, it is readily observed that the growth is very different. The darker region (left) corresponds to sandwiched-horizontal portion and is fully covered with graphene. The brighter region (right) corresponds to the vertical Cu foil and only presents small islands of graphene (observed as dark spots). We have also found that the growth morphology of graphene differs in the two regions. In the confined region, graphene is featureless. In contrast, by zooming into the unconfined region, we find that graphene flakes are etched into dendritic shapes (**Figure** 3.8**c**).

In the confined region, the gas flow velocity is much slower due to the reduced space between the Cu foil surface and the sample holder, resulting in a thicker boundary layer where mass transport of carbon and H_2 to the Cu foil is slow [128]. Consequently, the growth rate and its accompanying H_2 production become slower. However, in the unconfined region, the boundary layer is thinner. There, the mass transport of the reactants to the Cu foil is fast, facing a higher concentration of carbon promoting growth [128] and a higher flow of H_2. The H_2 enrichment at the catalyst surface plus the local

rise of H_2 produced from the reaction as a byproduct favors the etching reaction. Consequently, the etching process ends up dominating over the growth leading to dendritic graphene shape. Hence, these findings indicate that etching can be suppressed by subjecting the catalyst in a confined reaction region.

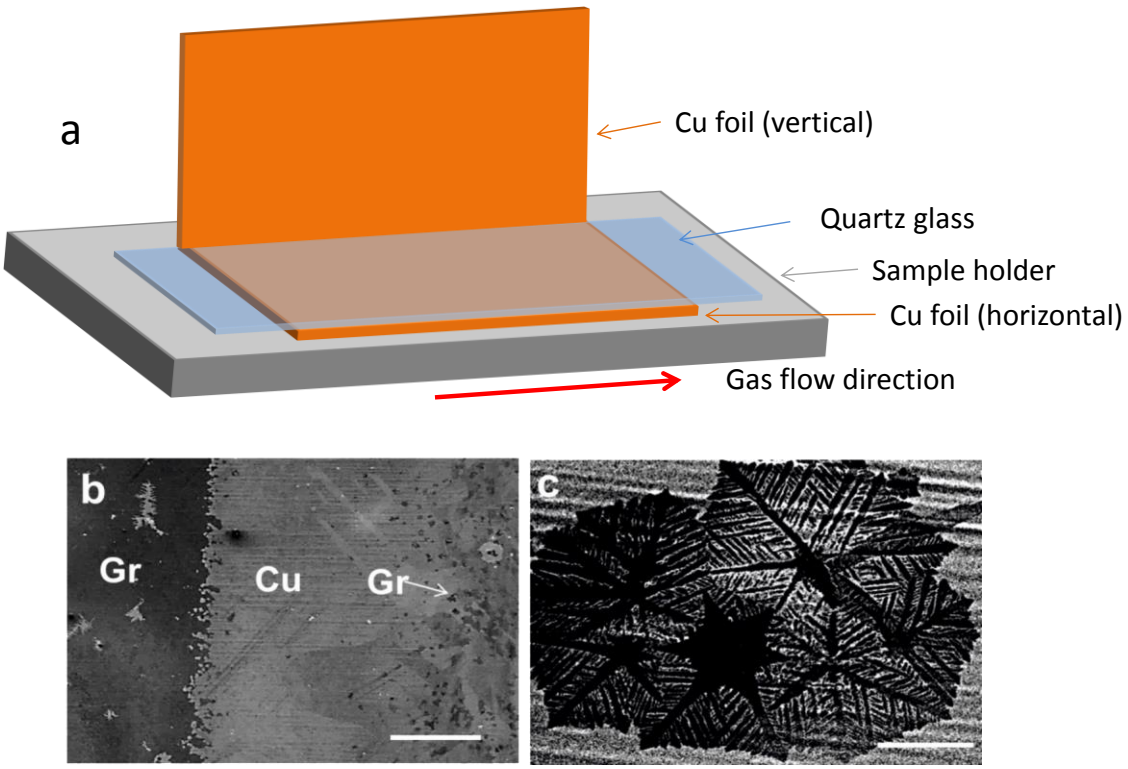

Figure 3.8. **a**) Schematics showing the geometrical configuration of the Cu foil during typical growth process (bent Cu foil), **b**) SEM image near the bent region containing both vertical (right) and sandwiched parts (left) and **c**) zoomed image of typical graphene islands in the unconfined Cu foil. The image in **c**) shows the dendritic shape structure due to etching caused by the *in-situ* rise of hydrogen partial pressure. The scale bars are **b**) 500 µm and **c**) 100 µm.

3.2.5 Electrical and spin transport measurement

In order to evaluate the graphene electronic/spintronics transport efficiency, we fabricated spintronic devices from graphene grown during 10 minutes. Briefly, the grown graphene was transferred onto 440 nm SiO_2/Si and patterned with electron beam lithography using MMA/negative resist (MMA/NR). After lift-off, the patterned graphene was chemically cleaned and annealed at high temperature in a vacuum. After that, the contacts were defined using positive resist-based electron beam lithography followed by evaporation of tunnel barriers (TiO_2) and ferromagnetic contacts (Co) (see Chapter 2: for detail fabrication steps).

Electrical characterization of the CVD graphene device was carried out by measuring the field-effect characteristics using a back-gate voltage V_g applied to 440 nm SiO_2/Si substrate. **Figure** 3.9 shows the fabricated device and plots of the electrical and spintronic transport characteristics. shows the graphene resistance (R) as a function of gate voltage V_g. The charge neutrality point (*CNP*) appears around 0 V which indicates that the doping level of graphene is very low in contrast to most of the graphene devices which exhibit right-shifted *CNP* (p-doping) due to adsorption of water from the air [129] or due to polymer residues **Figure** 3.9**a** shows an optical image of the device after the lift-off and chemical cleaning procedures. **Figure** 3.9**b** depicts the plot of the carrier mobility as a function of the carrier density of graphene. The carrier mobility of the devices was in the range of 3,000 cm^2/VS to 5,000 cm^2/VS at higher carrier concentrations. For

example, in this particular device, the electron mobility was about 3,300 cm^2/VS at n = 2x 10^{12} cm^{-2} which are typical values for CVD grown graphene.

The spin transport characteristics of the grown graphene were also evaluated by measuring the Hanle spin precession with the magnetic field $B_\perp$ applied perpendicular to the graphene plane. **Figure** 3.9**c** shows a room temperature Hanle spin precession measurement for the same device with the measured data (red curve) and the best fit (black curve)

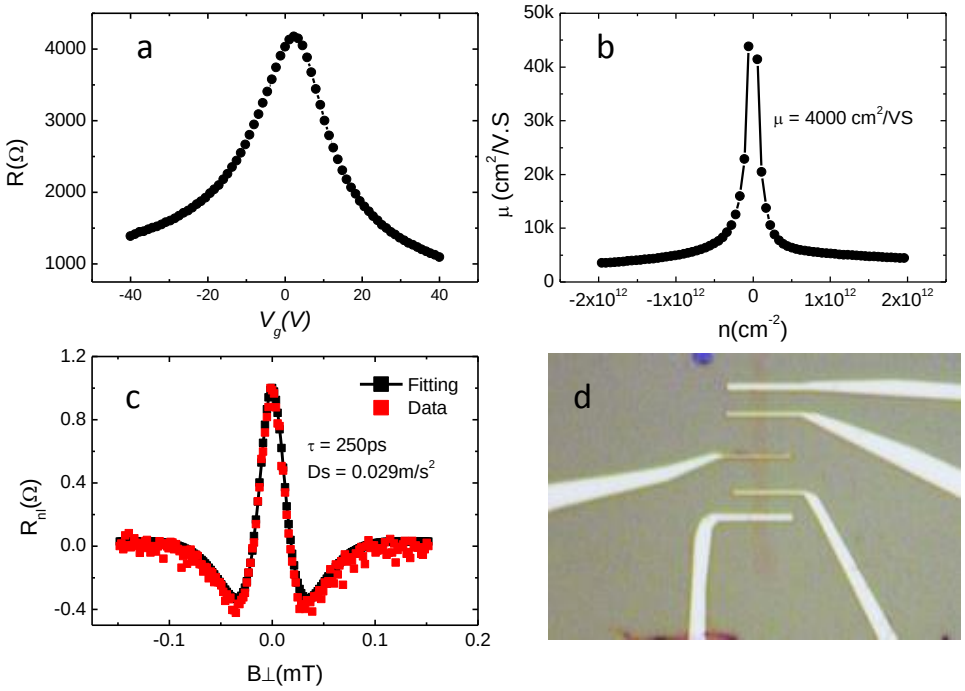

Figure 3.9. Electronic and spin transport measurements of a typical device fabricated from graphene grown for 10 min. **a**) Graphene resistance as a function of V_g. **b**) Mobility vs graphene carrier density. **c**) Room temperature Hanle spin precession measurement with the measured data (red curve) and best fit (black curve). **d**) Optical image of the fabricated device.

From the fitting of precession measurement results we obtained spin relaxation time τ_s = 250 ps, diffusion constant Ds = 0.029 m^2/s^2 and spin diffusion length λ_s = 2.7 μm which are typical values for CVD grown graphene on Cu foil. However, we have shown that the spin lifetime and spin diffusion length on CVD graphene can be further increased exceeding 3 ns and 10 μm, respectively by growing on Pt foils, by improving the graphene processing procedures and patterning long spin channels, as detailed in chapter 5.

3.3 Conclusions

We have demonstrated that the graphene morphology changes from a compact to a dendritic structure over the growth time without modifying the external growth conditions. The dendritic shape is a consequence of a competing backward etching reaction, which starts dominating over the growth at long times due to an *in-situ* hydrogen concentration increase. This contrasts with previous reports, which ascribed such dendritic structures to a surface diffusion-controlled growth. The results were further confirmed by decreasing the external flow of hydrogen, which led to a suppression of the etching. We found, however, that further growth at low hydrogen flows was slowed down due to the emergence of oxidizing etching, indicating that the concentration of gaseous oxidants also increased. Moreover, the etching induced by the *in-situ* increase of hydrogen concentration was also very dependent on the Cu foil geometrical arrangement, yielding highly etched graphene on unconfined Cu foil regions. These findings demonstrate that local fluctuations of the reactants during growth have a large impact on the resulting graphene morphology. They provide information on the etching process of graphene and highlight the critical importance of confinement aspects and the balance of gases as a source of heterogeneities, which can account for the wide dispersion of results among research groups. Finally, the spin transport measurement of the device fabricated from our graphene shows similar values typical for CVD graphene grown on Cu foil. However, more optimization is needed on the quality of graphene to improve the spintronic parameters.

Chapter 4: Photocatalysis-assisted suppression of graphene nucleation density during CVD growth

The aim of this chapter is to introduce a novel approach to reduce graphene nucleation density for the growth of large size single-crystal graphene to improve the performance of electronic/spintronic devices. A new and efficient strategy to drastically reduce the nucleation density of graphene by using photocatalysis-assisted thermal annealing of Cu foil is presented. We found that high-temperature thermal annealing of the Cu foil in the presence of visible light can remove ab/adsorbed hydrocarbon contaminants from Cu foil. The removal of contamination is ascribed to the in-situ production of reactive oxygen species (ROS) mediated by semiconductor Cu oxides. The photo-activated oxygen species can, in turn, trigger highly efficient degradation reaction pathways with the residual carbonaceous contaminants to finally be decomposed into CO or CO_2. With this simple annealing strategy, a much lower nucleation density was achieved as compared to the standard thermal annealing under similar growth parameters. These are the preliminary results of nucleation density reduction. Electrical and spintronic measurements are yet to be performed.

4.1 Introduction

One of the foremost challenges for the scalable integration of graphene technology is the difficulty of producing high-quality large-size single-crystal graphene [130]–[132]. As mentioned in the introduction, CVD is considered the most promising method to develop a suitable and scalable approach to synthesize “electronic-grade” graphene and related 2D materials [130], [133]. In general, CVD grown graphene features polycrystalline morphology due to the presence of multiple nucleation sites, which yield the formation of multiple graphene domains. The size of these domains and the characteristics of the grain boundaries [134] determine, to a great extent, the physical and chemical properties of the graphene film [135]–[138]. Therefore, a crucial aspect of CVD growth is the effective control of the graphene nucleation. Polycrystalline Cu foil is a cost-effective catalytic material and is widely adopted by the emerging industry, thus considerable efforts are being invested to gain insight into graphene nucleation processes in such foils. Given the limited understanding of CVD growth, deriving from the complexity of the chemical processes and of the Cu surface at high temperatures, progress has been achieved with great effort by engineering the growth conditions empirically.

It has been demonstrated that graphene nucleates at defects, steps, and impurities on the Cu surface [139]–[141]. However, a critical challenge is to reproducibly obtain a clean Cu substrate free of carbon residues before the growth. Methods to grow grain-boundary-free graphene thus aim at eliminating or passivating the nucleation sites and,

in this context, Cu surface pretreatment has become crucial. As mentioned in the main introduction of this thesis, several studies have been reported addressing the possible ways of reducing nucleation density resulting in single-crystal graphene as large as several millimeters of diameter [49], [51], [54], [128], [142], [142]–[145].

However, many of these approaches use arduous pretreatments, very extreme conditions such as very high temperatures or annealing pressures, very long annealing or growth times or hazardous procedures (such as dosing oxygen in the reactive CVD chamber prior to the growth step). Therefore, finding new practical and safer strategies is highly desirable provided that pretreatment conditions are a key prerequisite to ensure the ultimate control of graphene nucleation densities to grow mm sized-single crystal graphene.

In this study, we propose and demonstrate a robust yet scalable procedure that drastically reduces the graphene nucleation density by removing impurities using photocatalysis (photo-assisted annealing) process. It is found that pretreating the Cu foil with light in the visible range, while annealing at high temperature (1000 ^{o}C), can lead to the degradation of carbonaceous impurities. The removal of the impurities is ascribed to the production of oxygen species that react with them, assisted by Cu oxides as photo-catalyst. The relevance of photo-assisted annealing is established by changing the wavelength of the incident light and by thorough X-ray Photoelectron Spectroscopy (XPS) measurements of Cu foils, with and without photo-assisted annealing. In this way, a fast yet simple method is developed to control the synthesis of high-quality graphene, suitable for electronic, spintronic and photonic applications. With this simple cleaning

process, we achieved a much lower nucleation density than with the standard thermal annealing under similar growth parameters.

4.2 Experimental setup

The schematics of the experimental setup used to test the proposed photo-assisted suppression of impurities, and the subsequent reduction of graphene nucleation centers, is shown in **Figure** 4.1**a**. The tube furnace for graphene growth was adapted to anneal the Cu foil in the presence of an externally controlled light source. A T-shaped three-opening tube was installed to connect the gas lines with the growth quartz tube in the furnace. The T-adaptor had a glass window with a line of sight access to the Cu foil surface. A laser (wavelength 447 nm and power 0.5 W) was used as the light source. The beam spot of about 5 mm in diameter, which was smaller than the Cu foil, allowed us to directly compare the growth behavior inside the beam region and outside the beam region of the same Cu foil. Further, control of the light wavelength, by using specifically selected lasers, made it possible to address the influence of the photon energy in the photocatalytic process. Indeed, by selecting photon energy above or below the bandgap of the Cu oxide, it was possible to respectively activate or deactivate the photocatalytic process.

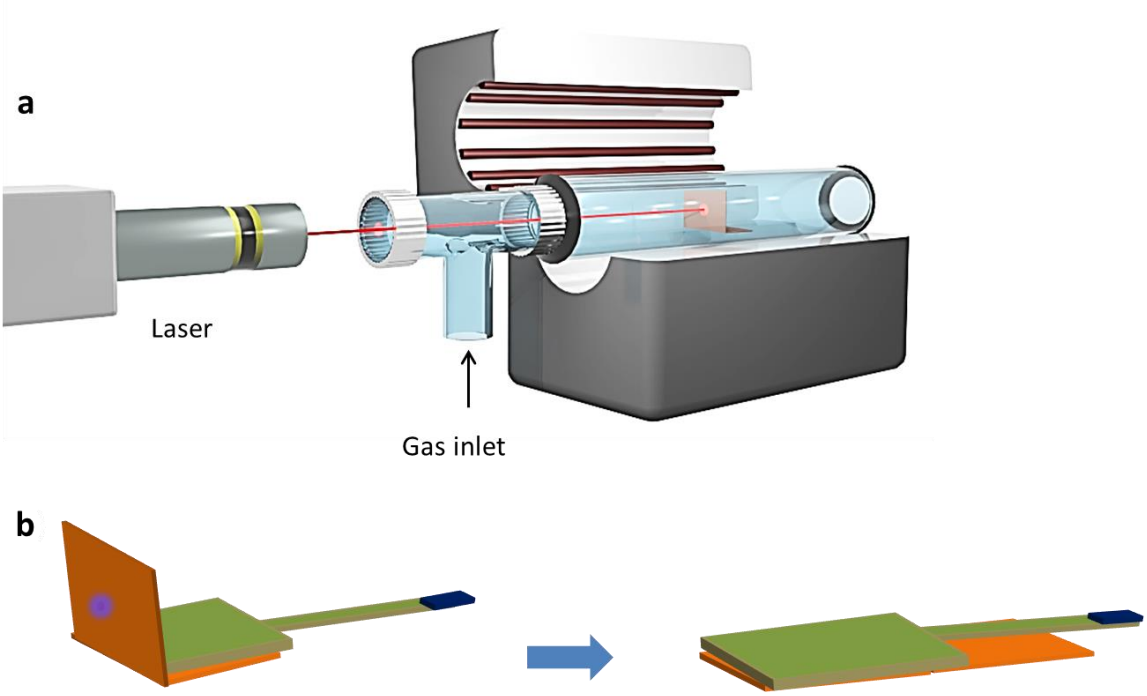

Figure 4.1. **a**) Schematics showing the photo-assisted annealing set-up. It contains a bent Cu foil at the center of the reactor and light passing through the transparent window of the three opening tube. **b**) Schematics showing the process of sandwiching the Cu foil after photo-assisted annealing. During the growth step, the photo-assisted cleaned side of the Cu foil was faced down to the sample holder.

Briefly, the Cu foil was positioned vertically inside the heating furnace and illuminated with light (**Figure** 4.1**a**) at 1000 °C in a reduced pressure containing Ar (450 sccm) and H_2 (50 sccm) for 30 min. The laser wavelength was 447 nm and had a power of 0.5 W. The wavelength is equivalent to photon energy ~2.77 eV, which exceeds the bandgap of the Cu oxide stable forms (see **Figure** 4.1 and discussion below). Immediately after annealing for 30 min, the laser-exposed side of the Cu foil was sandwiched between the sample holder and the quartz tube to place it in a confined

reaction region (**Figure** 4.1**b**). Sandwiching the Cu foil was carried out by two-magnet manipulation: one magnet was attached at the very end of the sample holder (the dark blue piece in **Figure** 4.1**b**) and a second one is operated from outside tube. Then, a standard growth process was carried out as detailed in chapter 2.1. The confinement favored a uniform distribution of reactant concentrations [46] and lead to homogeneous growth kinetics [146] over the entire Cu surface, both inside and outside the region exposed to the light beam.

4.3 Systematic study of nucleation density on photo catalytically cleaned Cu foil

In order to demonstrate the exclusive effect of the photo-assisted cleaning on reducing nucleation density, we grew graphene on two Cu foils having different surface treatment conditions, namely:

- **Photo-assisted annealed Cu foil**.
- **Photo-assisted annealed Cu foil after air exposure (post-exposed Cu foil).**

4.3.1 Nucleation density on photo-assisted annealed Cu foil

It is well established that Cu foil with purity level 99.8- 99.9999% has a range of surface and in-bulk impurities which together with Cu foil defects, steps and grain boundaries become active sites for graphene nucleation [147] [148]. **Figure** 4.2**a** shows SEM image of graphene nucleation densities at different regions of the photo-assisted

annealed Cu foil. **Figure** 4.2**b** depicts a large-scale image of the photoassisted-annealed Cu foil after a short growth time (10 min) in which a dramatic decrease of nucleation sites can be readily appreciated. The growth time was chosen to limit the graphene domain size and therefore avoid their coalescence, which allows us to directly determine the nucleation density as indicated in **Figure** 4.2**a**.

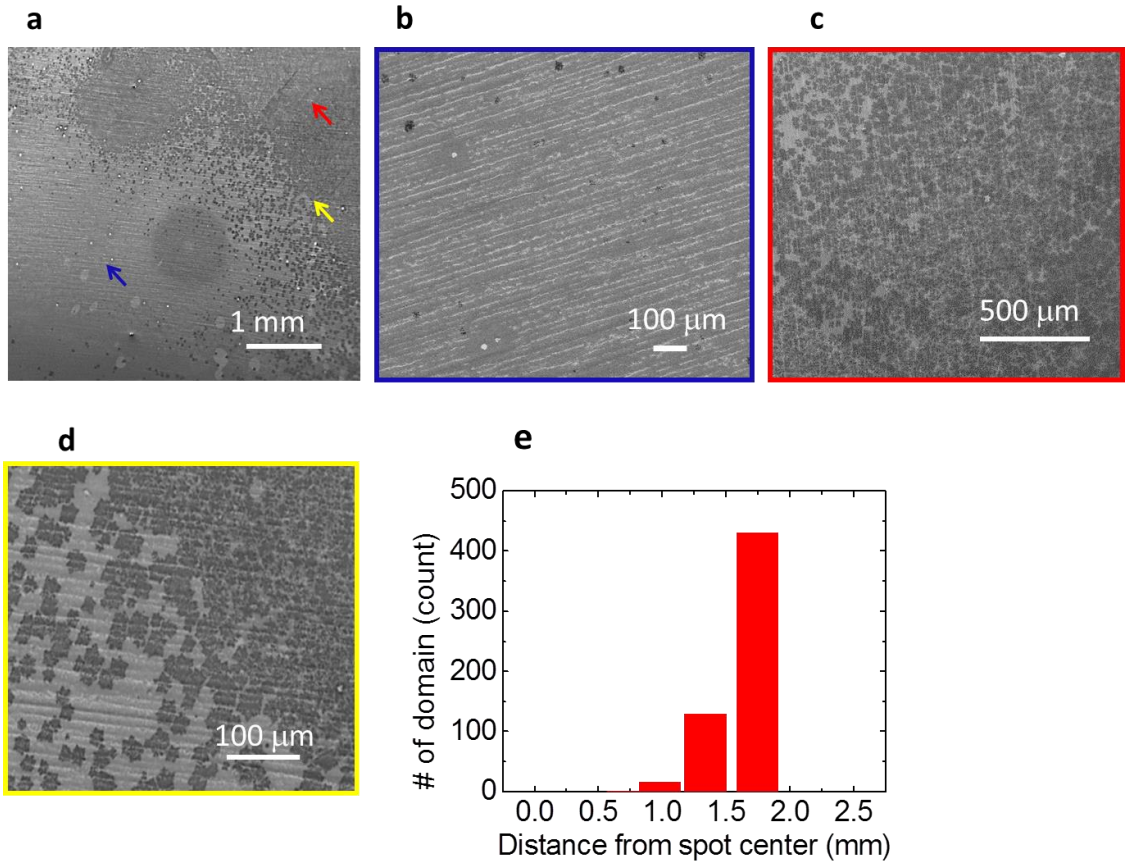

Figure 4.2. SEM images of graphene nucleation on photo-assisted annealed Cu foil: **a**) large scale SEM image of the nucleation density on a Cu foil. **b**) A zoom of the photo-assisted annealed region, where black spots are the graphene nucleation sites and the parallel striations are a consequence of the cold-rolling process used to fabricate Cu foils), **c**) outside the beam region and, **d**) at the boundary between the two regions. **e**) Position-dependent graphene nucleation density ρ_n.

Figure 4.2**c** shows details of the photoassisted-annealed Cu foil inside (**Figure** 4.2**b)** and outside of (**Figure** 4.2**c)** the laser beam and **Figure** 4.2**d** depict the nucleation density change at the boundary between the two regions. **Figure** 4.2**e** shows the position-dependent graphene nucleation density ρ_n, which is determined by quantifying the number of graphene domains. It was observed that ρ_n exceeds 400 mm^{-2} and decreases dramatically in the photo-assisted annealed region to values in the range of 1 mm^{-2}. Such a dramatic change in ρ_n is remarkable for a number of reasons. For instance, the growth results with the photo-assisted annealed Cu foil, suggest that additional pretreatments such as oxygen passivation might not be so necessary to reduce the nucleation density.

Having demonstrated the dramatic effect of photo-assisted annealing, we performed additional experiments to investigate its origin. As described above, the photocatalytic degradation of contaminants via Cu oxides might be the reason. Cu oxide appears in two stable forms: cupric oxide (CuO) and cuprous oxide (Cu_2O). CuO and Cu_2O are both *p*-type semiconductors with a narrow band-gap of 1.2 eV and 2.1 eV, respectively [149]. Both oxides have been exploited as visible-light-driven photocatalysts to convert hydrocarbons into carbon dioxide and to split water [150] [151]. It is also known that CuO decomposes to Cu_2O around 350 ^oC [152].

Therefore, CuO should be absent during the high-temperature annealing process and obviously could not contribute to the suppression of the nucleation sites by photocatalysis. In contrast, Cu_2O is stable above the melting point of Cu (1085 ^oC) [152] and should be the photocatalytic material at the annealing temperature (1000 ^oC).

In order to establish if the photocatalytic process is initiated by Cu_2O, a second experiment was carried out using a laser source with a wavelength of 808 nm and 2W in-power. The laser wavelength is now equivalent to *E* ~1.5 eV, an energy that is in between the CuO and Cu_2O bandgaps. This implies that electron-hole pairs would only be created in CuO (energy gap 1.2 eV) but not in Cu_2O (energy gap 2.1 eV); therefore, the photocatalysis in Cu_2O would be deactivated. The results of the 808 nm laser treatment inside and outside of the beam region are shown in **Figure** 4.3**a** and **b**. In agreement with the results obtained from a Cu foil treated without photo-assisted annealing (only thermal annealing), no significant variation in the graphene nucleation density was observed. This finding confirms that Cu_2O is the active material that mediates the photocatalytic process showing a significant capability to reduce nucleation sites by removing carbonaceous impurities from the Cu foil.

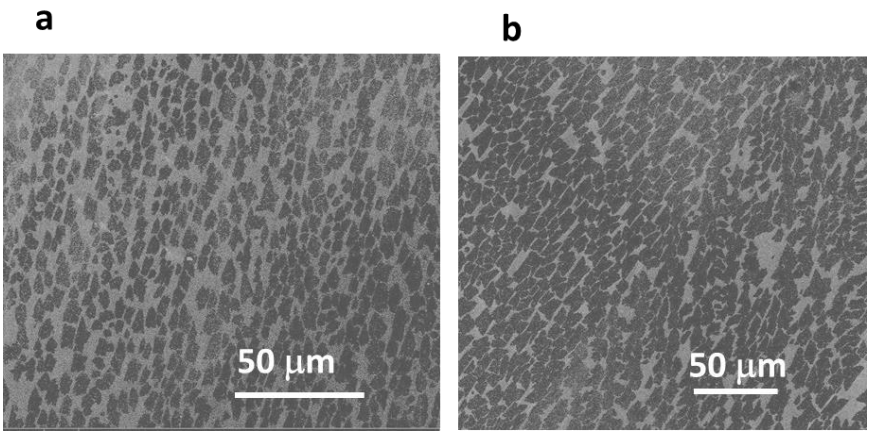

Figure 4.3. SEM images of graphene nucleation on red-laser treated Cu foil: **a**) inside and **b**) outside the beam region, showing no difference in the nucleation density of graphene. (Dark grains are graphene domains).

4.3.2 Nucleation density on photo-assisted annealed Cu foil after air-exposure

In order to further understand the effectiveness of light-assisted cleaning, we compare the nucleation density on the "re-contaminated" Cu foil inside and outside of the beam regions. Recontamination occurs through the adsorption of contaminants from the air. To do so, we cleaned the Cu foil with photo-assisted annealing following the same procedure, fast cooled and then exposed to ambient. Then, the exposed Cu foil was loaded back to the furnace followed by 10 min graphene growth. The nucleation density was observed on the Cu foil inside and outside the beam region. **Figure** 4.4**a** and **b** show optical images of graphene nucleation on the "re-contaminated" Cu foil inside and outside of the beam region, respectively. In contrast to the result observed in **Figure** 4.2, the nucleation density inside the beam region (**Figure** 4.4**a**) was higher than outside of the beam region (**Figure** 4.4**b**). This reveals that the photo-assisted process leaves a cleaner Cu surface which is very prone to be contaminated when it is exposed to air. It is known that a clean metallic Cu surface adsorbs carbonaceous contaminants upon air exposure because of its high surface energy (1850 $mJ/m^2$for clean Cu). Hydrocarbons have the lowest surface energy (25 mJ/m^2) and can cover a metallic surface in a dynamic process [153]. Thus, the extent of adsorption depends on the cleanness of the metal surface. Photo-assisted cleaning is more effective than the only thermal annealing one. Thus the carbonaceous contaminants will adsorb more effectively on the photo-

activated Cu foil surface leading to more nucleation sites during the subsequent growth steps (**Figure** 4.4**a**).

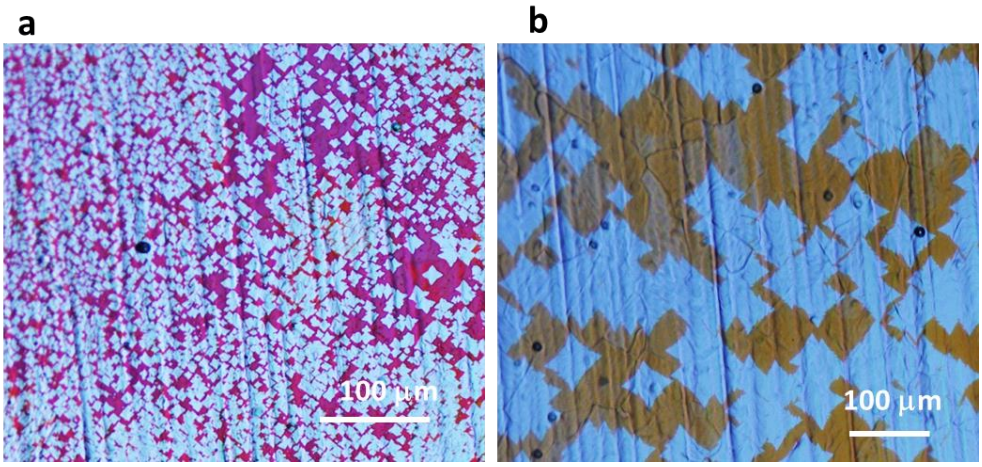

Figure 4.4**.** Selected optical images of graphene nucleation sites grown on air-exposed photo-assisted annealed Cu foil. Graphene nucleation densities **a**) inside the beam region, and **b**) outside of the beam region.

4.4 XPS characterization

In order to gain further insight into the effect of the photo-assisted annealing on the surface chemistry of Cu foil, we carried out *ex situ* X-Ray Photoelectron Spectroscopy (XPS) measurements on Cu foils with different surface conditions: as-received Cu foil (without any annealing) and Cu foil after photo-assisted annealing. The XPS of as-received Cu foil was measured as a reference to better assess the pretreatment effects on Cu. The XPS spectra of photo-assisted annealed Cu foil were recorded inside the laser beam and outside of the laser beam region to compare the nature of the two regions.

Here the photoassisted-annealed sample is exposed to air during the sample transport to the XPS system; hence the conditions are similar to those of samples in section 4.3.2.

Figure 4.5 shows the high-resolution XPS spectra of C1s and O1s core level on as-received Cu foil (without any annealing) and after photo-assisted annealing. **Figure** 4.5**a** shows the C1s core level spectrum for as-received Cu foil containing mainly three components at 284.8, 286.2 and 288.8 eV. The high intense peak at 284.8 eV corresponds to the expected adventitious carbon contaminants, which can be ascribed to C-C signal containing a mixture of *sp2*, and sp3 bonded amorphous carbon. The higher binding energy peaks can be ascribed to C-O and C=O. **Figure** 4.5**b** shows C1s XPS spectra of photo-assisted annealed Cu foil both inside and outside the beam region. **Figure** 4.5**c** shows comparatively the C1s signal for these regions together with the one of the as-received Cu foil. We observe three distinctive features by comparing the spectra of all these samples:

I. A shift of the C1s peak towards the lower binding region is observed inside the beam region **(Figure** 4.5**b)**. The C1s peak shifts to 284.5 eV on the beam region (correlated more with *sp2* bonding). Instead, the C1s peak corresponding to the outside of the beam regions is shifted to 285 eV, that is, towards the signature of sp3 bonding. The inset of **Figure** 4.5**c** shows the normalized spectra of the C1s for the different samples together with the XPS spectrum of a pure *sp2* graphite system for comparison.
II. A remarkable increase of the C 1s signal inside the beam region after exposure to the ambient atmosphere as compared to the C 1s signal on the outside of the beam region

and to the C 1s signal of the as-received Cu foil sample. The high amount of carbon content on the photo-assisted annealed Cu foil can be ascribed to the high proneness of Cu to adsorb species as a consequence of the higher degree of cleanliness and higher surface energy of the metal provided by the photo-assisted annealing. The carbon contamination on the clean Cu sample is triggered during fast cooling [154], [155] and during air exposure when transported from the CVD furnace to the XPS system. This finding is in agreement with the higher graphene nucleation density found on the photo-assisted annealed region when the sample was first exposed to air and then subjected to a growth (section 4.3.2). On the region outside of the beam, which is equivalent to the standard thermal annealing, the degree of cleanliness is relatively lower and "recontamination" is also lower providing a lower C 1s signal. Quite remarkable is the selective adsorption towards *sp2* moieties that are observed inside the beam region. That might be also related to the high surface energy of the clean Cu foil surface [153] which could catalyze more *sp2* bond formation.

III. The contributions corresponding to the oxygenated carbon species (C-O and C=O), quite well observed on the as-received Cu foil, decrease considerably on the photo-assisted annealed samples outside of the beam region but become undetectable inside the beam region. Such a trend is also observed when evaluating the O1s XPS line. **Figure** 4.5**d** shows the O 1s XPS spectra of the as-received Cu foil and the photo-assisted annealed Cu foil on both regions (inside and outside of the beam). A very intense and broad signal is observed on the as-received Cu foil at 531.3 eV corresponding to C-O, C-

OH, C=O, and metallic bonds (e.g. Cu-O, Cu_2O). The figure shows the dramatic decrease of such signal under the photo-assisted/thermal annealing. A closer look at the low oxygen response of the photo-assisted annealed sample is depicted in the inset. Interestingly, the oxygen peak signal outside of the beam region is shifted towards higher binding energies, more compatible with low traces of oxygenated carbon bonds (C-O and C=O whose binding energies range from 531.5-533 eV). Instead, the small O 1s peak recorded at the beam region is shifted towards lower binding energies (530.5 eV) and therefore it seems free from C-O bonds and more compatible with very low traces of metallic oxides (e.g. Cu_2O).

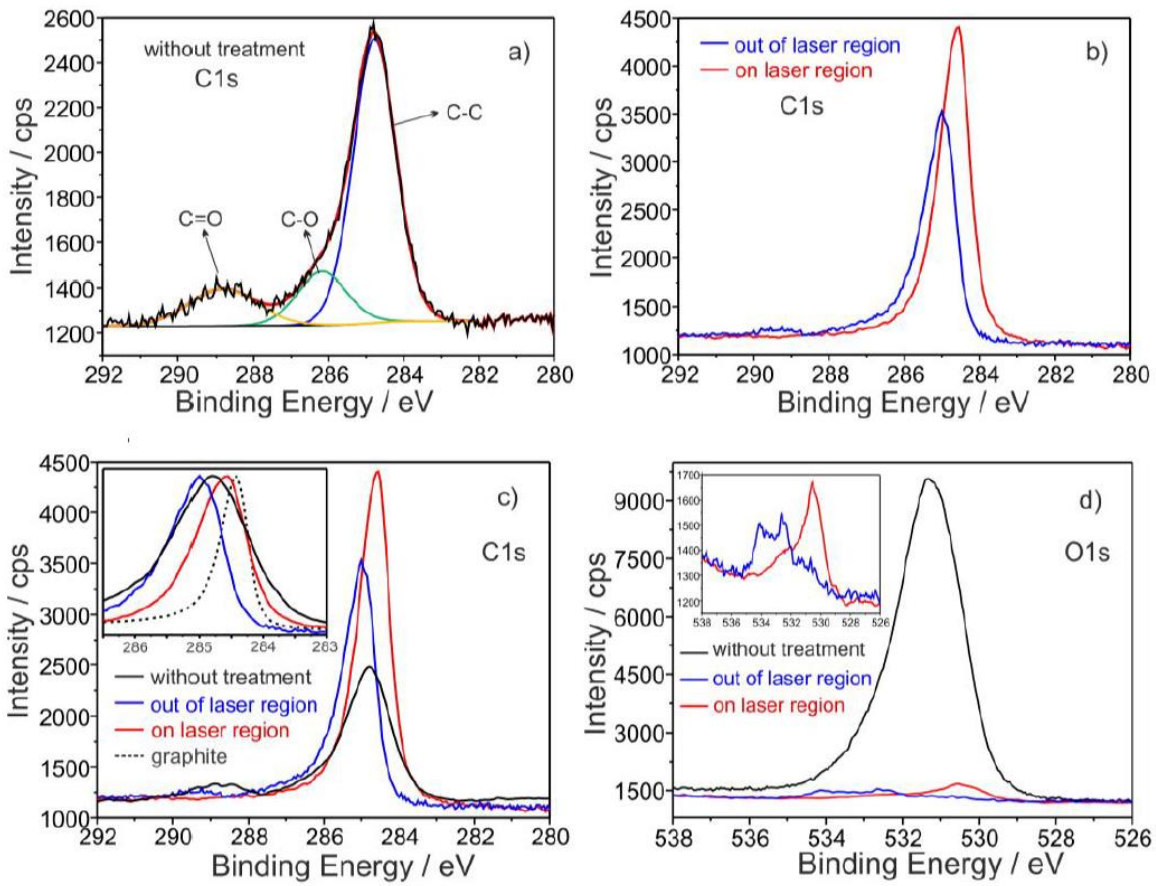

Figure 4.5. C 1s and O 1s core-level XPS spectra of Cu foils. **a**) C 1s on as-received Cu foil showing peaks ascribed to C-C, C-O and C=O bonds. **b**) C 1s on Cu foil after photo-assisted thermal annealing on the beam region (red line) and outside of the beam (blue line). **c**) C 1s for the combined spectra of as-received and annealed (inside the beam and outside of the beam). The inset corresponds to the normalized spectra of the different samples. A spectrum for graphite is included for comparison. **d**) O 1s on as-received Cu foil for outside (black) and inside of the photo-assisted annealed Cu foil (on the beam region (red line) and outside of the beam (blue line)). The inset shows details of the O 1s spectra of the photo-assisted annealed samples.

As a future task we are planning to perform *in-situ* and in operando XPS measurements during the photoassisted/thermal annealing process using synchrotron radiation with Near-Ambient Pressure Photoemission (NAPP) conditions. These measurements have the advantage of being very surface sensitive, as well as allowing for an easy selection of the incident x-ray photon intensity. At the same time, the smaller X-ray spot size probe will allow us to follow better spatial local changes when inspecting the regions inside/outside the laser beam region. In this way, we expect to achieve a more precise evolution of the metal foil surface chemistry in operando photoassisted/thermal annealing process.

4.5 Profilometer measurements

In order to evaluate the surface texture of the Cu foil after the photo-assisted annealing, we calculated the root-mean-squared (RMS or Rq) roughness on annealed Cu foil at different regions using an optical profilometer. This helps us to determine if there is a change in the surface roughness of the Cu foil due to the laser power during the photo-assisted annealing. The measurement was done on three regions, namely, inside the beam, outside the beam, and opposite side to the beam, as shown in **Figure** 4.6**a** with corresponding Rq values of 155, 157 and 156 nm, respectively. From these values, we clearly observe that the roughness does not vary significantly on the sample positions, revealing that the photo-assisted annealing has no effect on the texture of Cu foil.

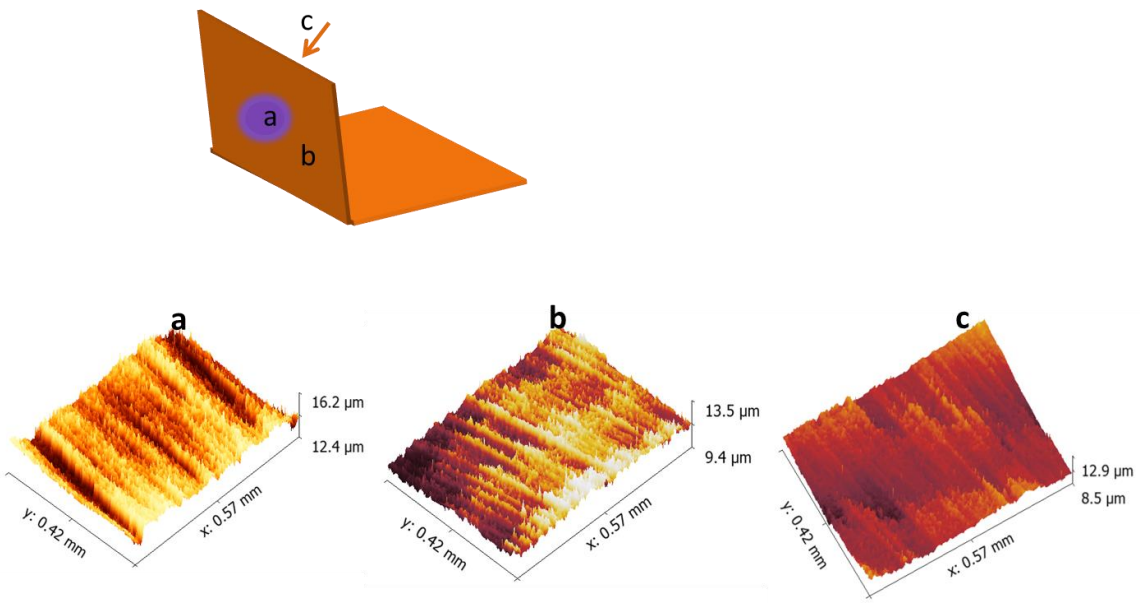

Figure 4.6. profilometric measurements at different Cu foil positions after photo-assisted annealing process. **a**) On the beam (155nm), **b**) far from the beam (157 nm) and **c**) opposite side of the beam (156 nm).

4.6 Discussion

As previously described, the experimental findings suggest a photocatalytic degradation of contaminants on Cu substrate as the mechanism behind the photo-assisted thermal annealing, which results in a suppression of the graphene nucleation density. Light incidence with a characteristic photon energy *E* above the metal oxide bandgap promotes the generation of electron-hole pairs, which become reducing and oxidizing agents. These redox agents initiate the formation of powerful intermediate species the so-called reactive oxygen species (ROS) around the catalyst surface which are

capable of degrading carbonaceous contaminants. In the CVD process, ROS can arise from residual oxygen in the reaction chamber or from the decomposition of Cu oxide [152]. As shown in **Figure** 4.7, the redox process of such molecules generates ROS in the form of O_2^- or radicals OH^- which can then easily react with carbon contaminants on the surface or even penetrate into bulk Cu to scavenge carbon, which is ultimately degassed as CO or CO_2 [152]. The synergy of the combined photochemical and thermal activation can then trigger reaction pathways that are not accessible with just only thermal treatment, resulting in a faster in-depth removal of impurities from the Cu-foil surface. Therefore, annealing with light in the presence of appropriate photocatalyst can result in a very effective *in-situ* cleaning of the Cu foil by the photocatalysis process.

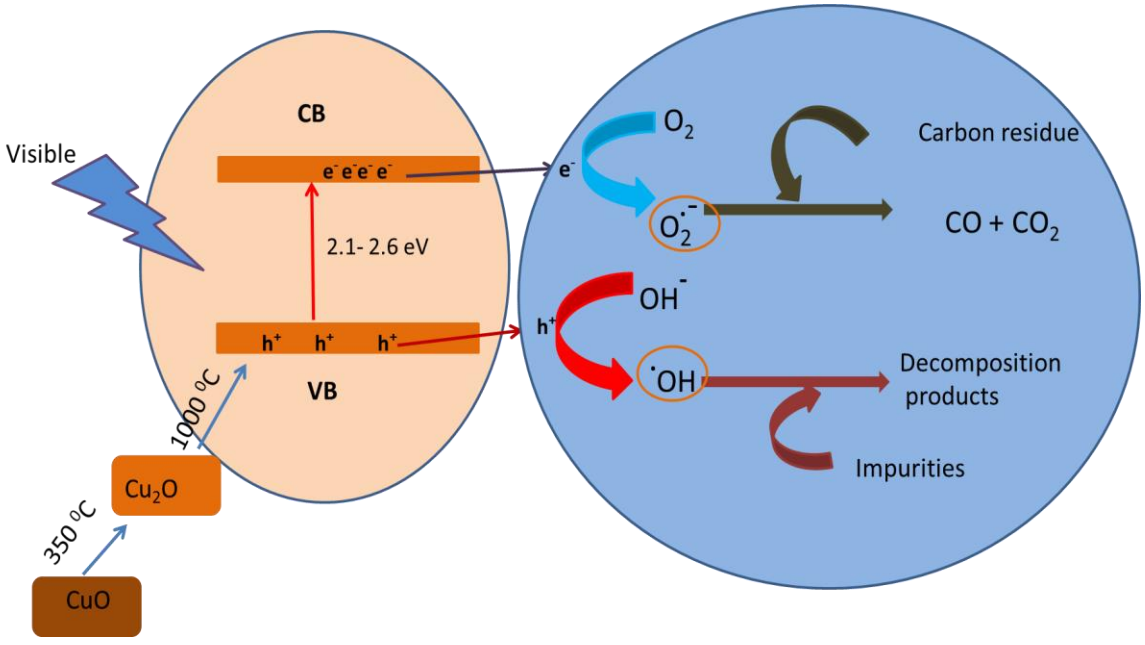

Figure 4.7. Plausible photoactivation mechanism for the removal of contaminants mediated by semiconducting Cu oxides.

4.7 Conclusions

Photo-assisted annealing is a powerful and practical pretreatment strategy that yields to the efficient removal of carbon/oxygen contaminants from Cu foils. We attribute these findings to the combined action of photocatalysis and thermal activation processes. Thermal annealing helps to segregate carbon contamination to the surface of Cu foil but its removal is not efficient enough. Instead, photocatalysis in combination with high temperature has the capability of generating reactive oxygen species-mediated by semiconducting Cu oxides. The photoactivated oxygen species can, in turn, trigger highly efficient degradation reaction pathways with the residual carbonaceous contaminants to finally decompose into CO or CO_2. Moreover, the reactive oxygen species could have the ability to easily penetrate through the bulk of Cu foil to scavenge carbon species, which could not be completely removed by thermal annealing alone.

Thus, this technique emerges as a very promising alternative strategy to other Cu pretreatments characterized by being tedious, arduous, lengthy or hazardous, and thus to contribute to the synthesis of large-size single-crystal graphene.

Chapter 5: Spin communication over 30-µm long channels of chemical vapor deposited graphene on SiO_2

Under the context of improving the spin transport properties of CVD grown graphene, we present in this chapter a modified device fabrication technique for spin transport measurement using CVD graphene grown on platinum (Pt-CVD). The interaction between graphene and Pt substrate is very low compared to the interaction between graphene and Cu foil, hence the electronic structure of monolayer graphene on Pt is close to that of isolated graphene [156]. With this graphene we demonstrate a high-yield fabrication of non-local spin valve devices with room-temperature spin lifetimes of up to 3 ns and spin relaxation lengths as long as *9* µm on SiO_2/Si substrates. The spin-lifetime systematically presents a marked minimum at the charge neutrality point, as typically observed in pristine exfoliated graphene. However, by studying the carrier density dependence beyond $n \sim 5 \times 10^{12}$ cm^{-2}, via electrostatic gating, it is found that the spin lifetime reaches a maximum and then starts decreasing, a behavior that is reminiscent of that predicted when the spin-relaxation is driven by spin-orbit interaction. The spin lifetimes and relaxation lengths compare well with state-of-the-art results using exfoliated graphene on SiO_2/Si, being a factor two-to-three larger than the best values reported at room temperature using the same substrate. As a result, the spin signal can be readily measured across 30 µm long graphene channels. These

observations indicate that Pt-CVD graphene is a promising material for large-scale spin-based logic-in-memory applications.

5.1 Introduction

As mentioned before, graphene has emerged as a tantalizing platform for spin electronics [98], [157], [158]; owing to its low spin-orbit coupling and lack of hyperfine interaction, spins in it can flow efficiently over very long distances. While exfoliated graphene has been used for fundamental studies, the small scale production limits its suitability for the realization of spintronic technology requiring long propagation channels or multiple devices. This can be overcome by using chemical vapor deposited (CVD) graphene [158]–[160]. However, although spin-lifetimes of up to 1.2 ns have been observed in CVD graphene on SiO_2, the results are often reported for a single device and are hardly reproducible. That sets serious limitations for testing (complex) circuit architectures with more than one device, which is one of the key requirements for any industrial application. Equally important, the lack of reproducibility precludes, for instance, exploring the spin properties of CVD graphene and the influence of grain boundaries, structural defects and vacancies, which are, for the most part, absent in the exfoliated counterpart. Reliable fabrication of CVD graphene spin devices would, therefore, help enable large-scale spintronic applications and the realization of systematic studies to identify the dominant spin relaxation mechanisms.

In this chapter, we demonstrate a high-yield fabrication of non-local spin-valve devices with long-distance spin transport at room temperature. The devices were patterned on platinum-based chemical vapor deposition (Pt-CVD) synthesized single-layer graphene on SiO_2/Si substrates [161]. Structural and spin transport characterization of devices were performed with channel lengths *L* varying from 4 to 30 μm. Spin lifetimes τ_s of up to 3 ns and spin relaxation lengths λ_s as long as ~9 μm were observed, which represent the highest values achieved so far for graphene, exfoliated or CVD, on a SiO_2/Si substrate. The record-large spin relaxation times and high yield represent a significant advance for spin communication via interconnects and lateral spin-logic technologies [162]. Furthermore, the reproducibility of the measurements allowed us to carry out a reliable and exhaustive comparison of the characteristics of the device as a function of *L* and graphene carrier density *n* and gather valuable information on the spin relaxation mechanisms. We found that contact-induced spin relaxation does not play a dominant role and that the dependence of τ_s on *n* agrees with the expectations for spin-relaxation driven by spin-orbit interaction.

5.2 Results

5.2.1 Device fabrication and characterization

A typical device is shown in **Figure** 5.1**a.** It consisted of an array of ferromagnetic (FM) contacts, attached to graphene, with variable distances between consecutive electrodes. Pairs of these contacts were used as spin injector and spin detector while

their separation defines the spin channel length *L.* We systematically studied the fabrication of the devices to optimize their quality in terms of the graphene source, electron-beam resists, and post-fabrication processing. The detail of the device fabrication process is presented in chapter 2. In short, the graphene was grown on Pt foils at temperatures up to 1100 ^{o}C by CVD [161]. It was then transferred using electrochemical delamination methods with tetraethylammonium hydroxide (0.1M) as electrolyte solution which assured ~100% coverage with good adhesion on SiO_2/Si (with 90 nm thick oxide layer) substrates [163], [164]. Large, clean and defect-free areas of graphene were identified and selected using an optical microscope after which long graphene stripes (of about 75 - 150 μm) were lithographically patterned using AR 7520.17 negative-resist based mask and subsequent oxygen-plasma etching. After etching and resist removal, the samples were annealed in a vacuum chamber (10^{-8} Torr) to eliminate resist residues. Ferromagnetic cobalt electrodes were then defined by means of electron beam lithography using a PMMA/MMA bilayer mask. Titanium oxide barriers were deposited prior to the evaporation of 30-nm thick cobalt to achieve efficient spin injection. Further details on the contact fabrication can be found in Refs. [12] and [13]. The contact arrays had characteristics distances *L* varying from 4 to 30 μm

The structural quality and electrical properties of graphene were firstly characterized at room temperature. **Figure** 5.1**b** and **c** show, respectively, a typical Raman spectrum and an atomic force microscope (AFM) micrograph of a finished device. The low intensity of the D peak in **Figure** 5.1**b** points to a low density of defects in graphene, while the AFM micrograph demonstrates the complete removal of resist

residues. In the Raman spectrum, the intensity of the 2D peak is larger than that of the G peak, revealing that graphene is in monolayer form. Raman measurements at different points of the stripe demonstrate that the graphene has uniform quality across the entire device.

5.2.2 Electrical transport measurement

Electrical characterization was carried out by determining the field-effect response with back-gate voltage V_{gate} applied to the (conductive) Si substrate, enabling the control of the graphene carrier density n. **Figure** 5.1**d** shows the graphene resistance R vs. V_{gate} using four-probe measurements for specific L, as defined in a single graphene stripe (see **Figure** 5.1**a**). In this stripe, the charge neutrality point (CNP) was found at V_{CNP} = 8 V indicating p-doped characteristics. Although all the devices exhibited p-doping with a spread of just 1 V in V_{CNP} along the stripe, the degree of doping may vary between different batches of samples, with V_{CNP} lying in the range of 8 to 20 V, which implies a residual doping n_r in between $2\text{x}10^{12}$ to $5\text{x}10^{12}$ cm^{-2}. The field-effect carrier mobility, reproducibly estimated from the slope of the conductivity curve was about $\mu \sim 1700$ $cm^2V^{-1}s^{-1}$ at $n = 5\text{x}10^{12}$ cm^{-2}. The contact resistance R_C between the Co-electrodes and graphene, as determined from a three-terminal configuration measurement, was in the range of R_C = 10 to 20 kΩ. As shown in **Figure** 5.1**e**, the peak resistance at the CNP, R_{CNP}, in four stripes scales linearly with L in the contact array, demonstrating the homogeneity of graphene along the length of the stripe. **Figure** 5.1**e** also shows small variations in

different regions of the SiO_2/Si substrate. Deviation in the slope could arise from a variable density of grain boundaries on different stripes in distant wafer locations [167].

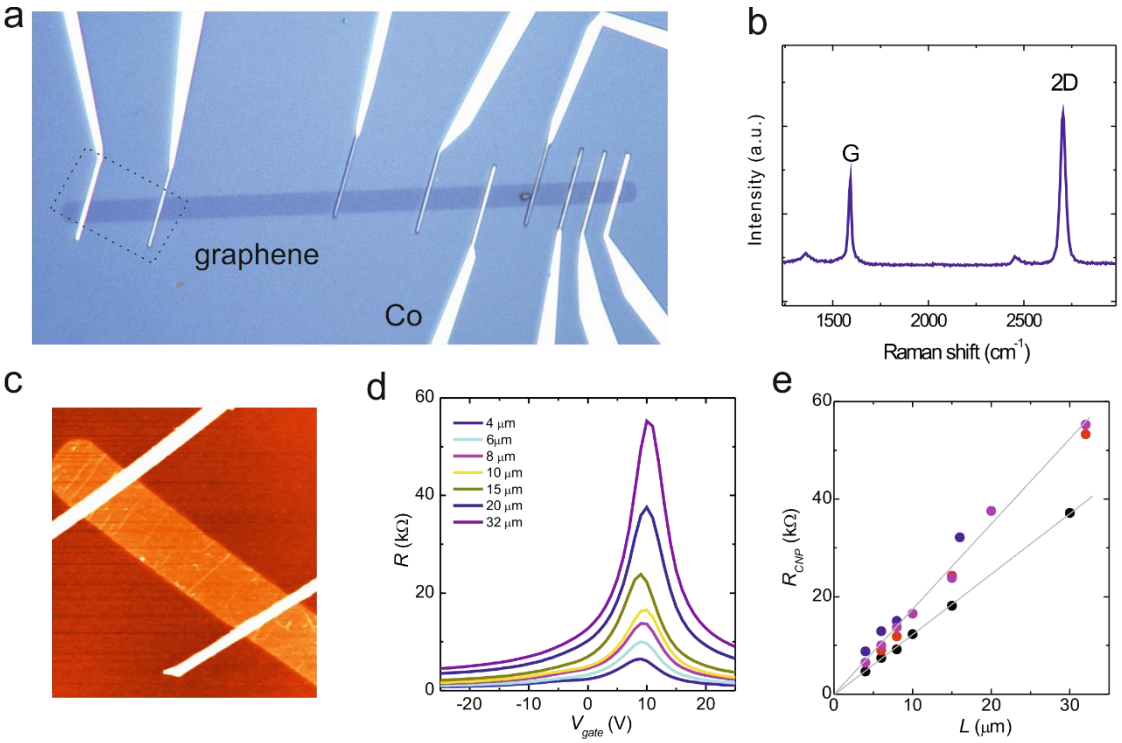

Figure 5.1. Characterization of Pt-CVD grown graphene devices. **a**) Optical image of a 100 μm long graphene stripe and Co-contact array conforming six non-local spin devices with channel lengths varying from 4 to 30 μm. The metal electrodes were made of 30 nm Co on 0.8 nm titanium oxide insulating barriers. **b**) Raman spectrum of the Pt-CVD grown graphene stripe, a.u: arbitrary units. **c**) Atomic Force Microscope micrograph of a region of the graphene stripe including two Co electrodes (first electrodes on the left in a); the scanning area is 5 x 5 μm^2. **d)** Resistance vs. back-gate voltage V_g measured in a four-probe configuration, for different channel lengths L. **e)** Resistance at the charge neutrality point (R_{CNP}) vs. L in four different contact arrays. The change in the slope from one array to the other indicates variations in the density of grain boundaries or defects in graphene.

5.2.3 Spin transport measurements

The spin transport properties were determined using the conventional non-local spin injection/detection scheme [168]. As represented in **Figure** 5.2**a**, spin accumulation in the graphene channel was created by injecting a current *I* from a FM tunnel contact (Co2), while a non-local voltage V_{nl} was detected remotely using a second FM contact (Co3) at a distance *L*. A change in the relative magnetization orientation of the injector and detector electrodes, from parallel to antiparallel, leads to a change of ΔV_{nl} in V_{nl} signal. ΔV_{nl} is a measure of the spin accumulation, or difference of electrochemical potential for spin-up and spin-down carriers, at the detector electrode. The widths of the FM electrodes determine their coercive fields, enabling to switch their magnetizations sequentially by applying an in-plane magnetic field $B_{||}$ along their long axis. The spin signal was characterized by the non-local resistance $R_{nl} = V_{nl}/I$. **Figure** 5.2**b** shows typical R_{nl} versus $B_{||}$ in a device with L = 20 μm. Spin signals at room temperature in such long graphene channels on any substrate were unprecedented. Previously reported nonlocal signals in graphene on SiO_2 were dominated by noise beyond L = 16 μm [160], while experiments on exfoliated graphene were done typically over shorter channels.

To extract the spin lifetime τ_s as well as the spin diffusion constant D_s (or the spin relaxation length λ_s. We performed Hanle spin precession measurements with the magnetic field $B_\perp$ applied perpendicular to the graphene plane. In the presence of $B_\perp$ the spins undergo Larmor precession while diffusing from the injector to detector. This leads

to a modulation of the spin signal, which can be described by the solution of the Bloch diffusion equation:

$$\Delta R_{NL} \propto \int_0^{\infty} \frac{1}{\sqrt{4\pi D_s t}} e^{-\frac{L^2}{4D_s t}} \cos(\omega_L t)\, e^{-\frac{t}{\tau_s}} dt$$

Where ω_L the Larmor frequency.

Figure 5.2**c** shows spin precession measurements for parallel and antiparallel magnetization configuration. By fitting the data to Eq. 1 we obtain τ_s = 3 ns, D_s = 0.03 m^2 s^{-1} and λ_s= 9.2 µm.

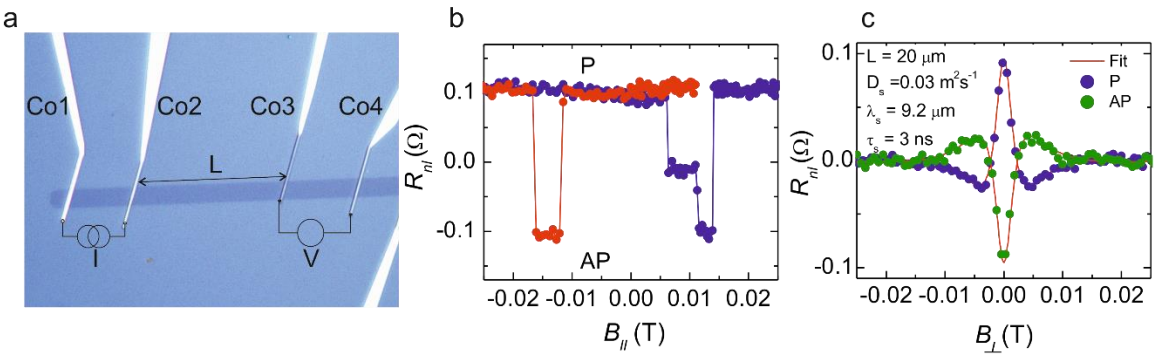

Figure 5.2. Non-local spin transport measurements. **a**) Optical image of a Pt-CVD grown graphene spin device. For spin transport experiments, the injected current *I* flows from Co2 to Co1 and the voltage V_{nl} is measured between Co3 and Co4. **b)** Non-local resistance $R_{nl} = V_{nl}/I$ as a function of an in-plane magnetic field $B_{\parallel}$ applied along the long axis of the ferromagnetic electrodes. **c)** Spin precession measurements with magnetic field $B_{\perp}$ applied out of the graphene plane for parallel (P) and antiparallel (AP) configuration of the injector/detector magnetizations. The red line represents the fit to the Bloch diffusion equation (Eq. 1). Data in **b** and **c** are acquired in a device with L = 20 µm at V_g = 0 V.

5.2.4 Channel-length dependence of the spin signal

The high yield and homogeneity of the Pt-CVD grown graphene-based devices provide the opportunity of studying the spin transport in nearly identical devices as a function of selected parameters, such as the spin channel length *L,* carrier density *n* or tunneling contact resistance. **Figure** 5.3**a** shows typical spin precession measurements at V_{gate} = 0 V for *L* ranging from 8 to 27 µm (array 1) with the corresponding fitting curves using Eq. 1. **Figure** 5.3**b** presents ΔR_{nl} as a function of *L*, which yields a linear dependence in a semi-logarithmic representation. **Figure** 5.3**c** to **e** show the extracted values for D_s (**Figure** 5.3**c**), λ_s (**Figure** 5.3**d**) and τ_s (**Figure** 5.3**e**) as a function of *L*. The spin parameters are in the range of $\tau_s \sim$ 2.1 - 3 ns, $D_s \sim$ 0.021 - 0.028 $m^2\ s^{-1}$ and $\lambda_s \sim$ 7 - 9 µm for all the devices, with no particular trend as a function of *L.*

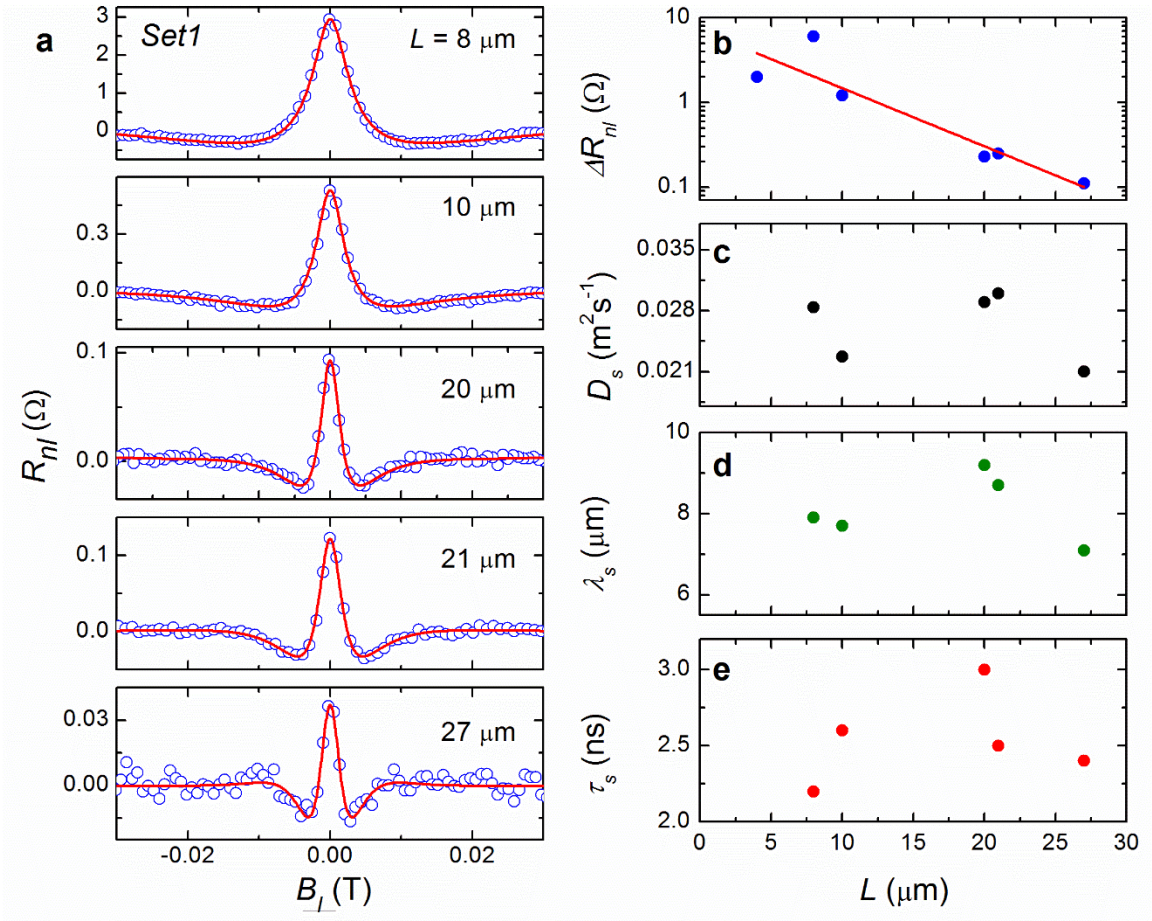

Figure 5.3. Channel length dependence of the spin transport. **a**) Spin precession measurements in a graphene stripe, using different pairs of contacts that define the channel lengths, *L*. Open circles correspond to experimental data and solid lines the associated fit to the solution of the Bloch diffusion equation, (Eq. 1.). **b)** Variation of the spin signal ΔR_{nl} with *L*, the solid line represents an exponential decay with effective spin diffusion length λ_s = 6.5 ± 1.5 μm. **c)** Spin diffusion constant (D_s). **d)** Spin diffusion length (λ_s) and **e)** spin lifetime (τ_s) vs. *L* as obtained for the fits in **a**.

5.2.5 Carrier-density dependence of the spin signal

The residual doping and the robustness of the devices warrant the generation of a hole carrier density n beyond 10^{13} cm^{-2}, which is about three times larger than the typically ones reached on similar devices [160]. **Figure** 5.4 shows ΔR_{nl} vs n up to $|n|$ ~ 1.1 x 10^{13} cm^{-2}. It was observed that ΔR_{nl} presents a pronounced minimum at the CNP, which is ascribed to a known reduction in τ_s. However, ΔR_{nl} reaches a maximum at n ~ - 6 x 10^{12} cm^{-2} and then starts decreasing.

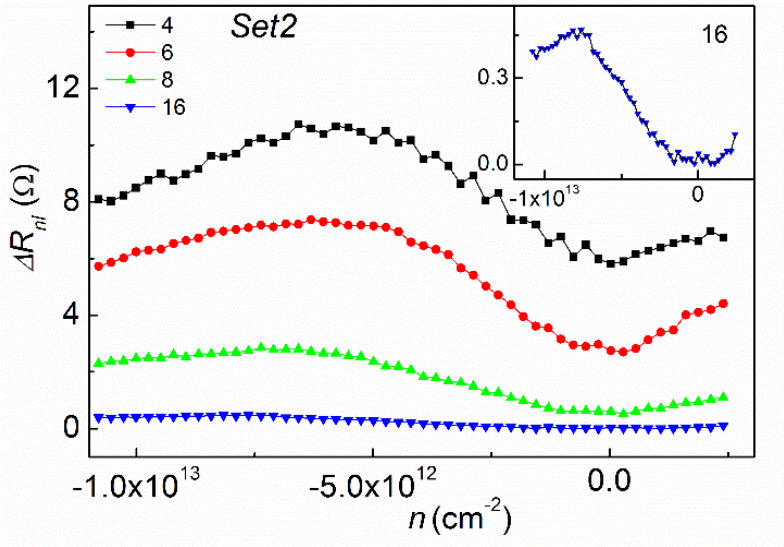

Figure 5.4. Spin signal ΔR_{nl} vs carrier concentration n for different channel lengths L. Regardless of L, ΔR_{nl} reaches a minimum at the CNP, increases with n up to n ~- 6 x 10^{12} cm^{-2}, beyond which a decrease is observed.

In order to indentify the origin of the maximum, we have carried out spin precession measurements as in **Figure** 5.3 using three additional graphene stripes and the corresponding sets of contact arrays. **Figure** 5.5 summarizes τ_s and λ_s as a function

of *n* as extracted from such measurements. As discussed previously, all the devices are *p*-doped, with the doping being homogeneous along each stripe. Both τ_s and λ_s are strongly dependent on *n*. In accordance with observations in ultra-clean graphene devices, originating from exfoliated graphite, τ_s and λ_s presented the characteristic minimum about the charge neutrality point (CNP), with τ_s increasing a factor 2 at $n \sim 10^{12}$ cm^{-2} [169], [170]. However, a remarkable decrease is τ_s and λ_s is found, systematically, for $|n| > 5 \times 10^{12}$ cm^{-2}, which has not been previously observed. The decrease is evident in all of the sets of contact arrays.

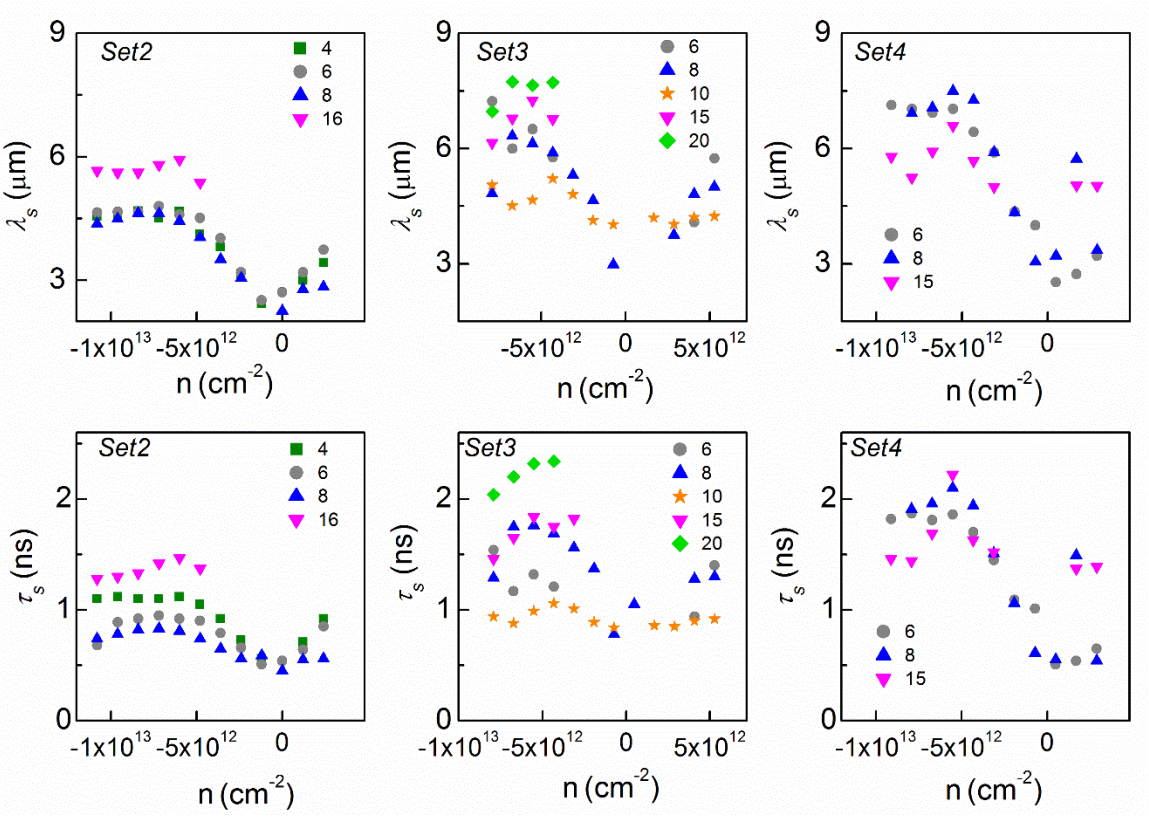

Figure 5.5. Dependence of the spin properties on three device arrays as a function of carrier density n. The spin diffusion length (top) and the spin lifetime (bottom) are shown for multiple

channel lengths L. The spin lifetime first increases (up to $n \sim -5 \times 10^{12}$ cm^{-2}) then decreases at larger carrier concentrations.

5.3 Discussion

The spin transport properties in general and the spin lifetime in particular, were determined by the influence of all the relaxation mechanisms available. Comprehensive measurements as those in **Figure** 5.3 and **Figure** 5.5 open alternative routes to determine dominant spin relaxation mechanisms. For example, it has been demonstrated that spin absorption by the contacting electrodes could play an important role in the spin relaxation process when the contacts are transparent [18]. However, it is difficult to assess the contact influence on the spin relaxation in experiments due to strong device-to-device variations. Therefore, it is usually estimated by theoretical modeling [172]–[174].

The results in **Figure** 5.3 allow us to directly address the contact influence on the spin relaxation. As *L* changes, the relative effect of the contacts should follow accordingly. If the contacts dominated the relaxation, their influence would be reflected in the spin transport characteristics. Specifically, as *L* decreases, τ_s should decrease. However, within our experimental resolution, we do not observe any trend on the spin parameters with L, thus we conclude that spin absorption in the electrodes is not a primary cause for spin relaxation in our devices.

The contact influence can be further assessed by plotting ΔR_{nl} vs L. For large enough contact resistances between the FM and graphene, the FMs do not significantly enhance the spin relaxation and ΔR_{nl} (L) is given by ΔR_{nl} (L) ~ exp[$-L/\lambda_s$], with λ_s an "effective" spin relaxation length. The consistency of the ΔR_{nl} measurements in **Figure** 5.3**b**, evidenced by the apparent linear dependence, confirms a substantial improvement over previous ones [160]. Here, we consider all the measured devices in the stripe with L ranging from 4 to 27 μm.

From the linear fitting (in the semi-log plot) we obtain λ_s ~ 6.5 μm. This value is somewhat smaller than λ_s in **Figure** 5.3**d,** as obtained from the Hanle fits. The difference derives from variations in the effective spin polarization P of the injectors and detectors. Indeed, the effective P for the 8-μm channel, $P \sim 12\%$, is unusually high when compared with the estimated value from the other measurements ($P \sim 7\%$). This explains the large spin signal for this specific L value (see **Figure** 5.3**b**); if that point was not considered in the fit, λ_s would be larger than 7 μm. Such observation implies that further enhancement on the device reproducibility should be achieved by improving the tunneling contacts, perhaps using insulating barriers that have shown to be more robust than TiO_x, such as SrO_x, amorphous carbon interfacial layers or hexagonal boron nitride [175]–[178].

The carrier density dependence of τ_s and λ_s (**Figure** 5.5) has been analyzed to discriminate between the proposed spin relaxation mechanisms in graphene. Initial studies aimed at identifying the relation between spin and momentum scattering times in order to establish whether the spin relaxation responded to an Elliot-Yafet or a

Dyakonov-Perel mechanisms, which exhibit opposite scaling. The results were inconclusive or even contradictory. One possible reason is that the scattering events that significantly alter the spin orientation represent only a fraction of all possible scattering events in momentum, rendering a small to null correlation between them. Such would be the case for resonant scattering with local magnetic moments. Calculations on hydrogenated graphene predicted spin lifetimes in the range of the experimental results with just ~ 1 ppm of hydrogen [179], [180]. They also showed a minimum at the CNP, as observed in experiments. This minimum has also been ascribed to spin relaxation mechanisms involving (Rashba) spin-orbit interaction and the ensued entanglement between spin and pseudo-spin degrees of freedom [99]. Measurements demonstrating isotropic spin lifetime suggested that the spin relaxation was driven by magnetic impurities or random spin-orbit or gauge field [170], [173]. However, the decrease at large *n* has only been reported for spin relaxation driven by spin-orbit interaction [99], [181] which adds valuable information to solve this puzzle**.**

5.4 Conclusions

The enhanced room-temperature spin parameters (τ_s = 3 ns and λ_s = 9.2 μm) in our Pt-CVD grown graphene devices represent a step forward in the field of graphene spintronics. These are the largest values reported so far for any kind of graphene on SiO_2. Furthermore, the spin signals at 15 μm are an order of magnitude larger than previously reported [160] while spin information can be transferred over distances of up to 30 μm.

The latter represents the longest graphene spin channel to date. Even though larger spin relaxation lengths have been reported in exfoliated graphene encapsulated by, or on, hexagonal boron nitride, the spin channel is much shorter, as it is limited by the exfoliated (random) crystal sizes.

Our devices presented unprecedentedly small variability within the same general region of the graphene. An exhaustive investigation of the spin properties as a function of the channel length and carrier density provided insight into the dominant spin relaxation mechanisms. We found no signs of spin relaxation owing to the contacts and observed for the first time, a decrease of the spin lifetimes at $n > 5 \times 10^{12}$ cm^{-2}. Such behavior has been predicted when the spin-relaxation is driven by spin-orbit interaction. That calls for further investigations of the spin lifetime at large n when the spin relaxation is driven by alternative mechanisms, such as resonant magnetic scattering. Beyond fundamental studies, the high-yield fabrication of our devices is expected to empower investigations of large-scale spintronic applications, such as spin-logic, logic-in-memory computation for beyond CMOS technologies which require multiple reliable ferromagnetic contacts and long graphene channel for spin-communication [182],[183].

Chapter 6: Conclusion and outlook

6.1 Conclusions

CVD growth of graphene using metal foils as the catalyst is one of the most promising methods for controllable and scalable synthesis of graphene film. Production of high-quality graphene with efficient performance is the requirement to better assess the fundamental physical properties and to establish future perspectives in the long-awaited technological applications. Reducing electron scattering centers of graphene by minimizing adsorbed contaminants, structural defects or grain boundaries are key aspects to enhance the performance of electronic/spintronic graphene devices. Accordingly, we have adjusted the CVD growth parameters as well as the graphene processing procedures (graphene transfer as well as the nanofabrication of graphene devices) to accomplish high-quality graphene and to ensure good device performance. Specifically, we have addressed:

1. the effect of the *in-situ* rise hydrogen concentration on the shape of the graphene domain and its quality using structural and electronic characterization,
2. the reduction of nucleation density using photocatalyst-assisted thermal cleaning of Cu foil and
3. the high-yield nanodevice fabrication from CVD graphene for spin transport measurements with enhanced spin parameters.

We have demonstrated that hydrogen partial pressure gradually increases with growth time and this causes a change in the graphene domain morphology during graphene growth. we have observed a morphological change from a compact to a dendritic structure. The dendritic shape is a consequence of etching domination over growth. This etching is caused by excess of hydrogen due to an *in situ* rise of hydrogen concentration from the decomposition of hydrocarbons. This result provides additional information on the influence of growth parameters on the shape-dependent properties of graphene.

Additionally, we have introduced a novel and efficient technique to reduce nucleation density during CVD growth of graphene-based on the photocatalyst-assisted thermal annealing of Cu foil. Exposing the commercial Cu foil with visible light in the presence of Cu_2O can generate reactive oxygen species. These reactive oxygen species can, in turn, initiate the decomposition reaction of the residual carbonaceous contaminants present on the Cu foil surface or in the bulk into CO or CO_2. *Ex-situ* XPS measurements of the adsorbed species on the surface of the Cu foil give further insights of the cleaning effect induced by the photo-assisted thermal annealing process.

Following graphene growth on Cu foil and its electrical characterization, we have fabricated devices based on monolayer CVD graphene grown on platinum foil (Pt-CVD) as a comparison. Using Pt-CVD graphene we achieved spin signals across record-long 30-μm channels at room temperature. We found room-temperature spin lifetimes (τ) of up to 3 ns and spin relaxation lengths (λ) of up to 10 μm on SiO_2/Si substrates. These values are a factor two-to-three larger than the best values reported to date using CVD

graphene on SiO_2/Si. The high-yield and homogeneity of our devices provide the opportunity to study spin transport as a function of device parameters and using complex device architectures. We show high-yield device fabrication techniques help to realize large-scale spintronic applications with complex multi-terminal device architectures.

6.2 Outlooks

Graphene growth on transition metal substrates has made a significant advancement in the last few years. A large number of scientific articles have been reported addressing the relation between growth parameters and graphene morphology. Tuning the growth parameters is crucial to control the growth of graphene with a specific shape for instance, hexagonal, flower shape, irregular shape, etc. We have shown that the changes in graphene morphology from a compact to a dendritic structure can be caused by etching due to *in-situ* rise of hydrogen. It has been reported in the literature that the dendritic structure of graphene is emerged either from growth mechanism or from hydrogen post etching. Here we understand that there is scattering of information on the mechanism of growth of graphene. Hence it would be very interesting to go deeper in understanding the root cause of these structural differences for controlled growth of high quality of graphene.

We have shown that the photocatalyst-assisted thermal annealing of Cu foil is a novel cleaning technique to drastically reduce the nucleation densities during CVD graphene. We observe a remarkable reduction of nucleation density using this cleaning procedure. However, because of the time limit, we could not explore the means of improving the size of the single-crystal graphene domain in the photo-assisted cleaned region. We have not also done detail spectroscopic and electrical characterization of the grown graphene. Hence, further work is needed to better optimize the technique to

grow large-size single-crystal graphene by combining with other techniques such as different copper foil geometrical arrangement (e.g. copper foil pocket). It would also be interesting to characterize the grown graphene both spectroscopically and electrically to determine the quality of graphene grown on the photo-assisted cleaned Cu foil region.

Our high-yield device fabrication strategy shows unprecedented enhancement on the spin transport parameters in a very long distance graphene channel. The property of long-distance spin communication enables the transmission and manipulation of spin signals within complex multi-terminal device architecture. this strategy could empower investigations of large-scale spintronic applications, such as spin-logic, logic-in-memory computation for beyond CMOS technologies. In this work, we have observed for the first time the decrease of a spin lifetime and spin diffusion length when the magnitude of the carrier density $|n| > 5 \times 10^{12}$ cm^{-2}. This result in combination with isotropic spin relaxation cannot be explained in the existing spin relaxation mechanisms. We, therefore, expect that our work will motivate theoretical studies to understand the root cause of this behavior of the spin parameters at very high carrier densities.

List of publications

1. **Z. M. Gebeyehu**, A. Arrighi, M. V. Costache, C. M. Sotomayor-Torres, M. J. Esplandiu, and S. O. Valenzuela, "Impact of the *in situ* rise in hydrogen partial pressure on graphene shape evolution during CVD growth of graphene," *RSC Adv.*, 8, 8234–8239, 2018.
2. **Z. M. Gebeyehu**, S. Parui, J. F. Sierra, M. Timmermans, M. J. Esplandiu, S. Brems, C. Huyghebaert, K. Garello, M. V. Costache, and S. O. Valenzuela "Spin communication over 30 µm long channels of chemical vapor deposited graphene on SiO2," 2D Mater., 6, 034003, 2019.
3. Natalie Briggs, **Zewdu M. Gebeyehu**, Alexander Vera, Tian Zhao, Ke Wang, Ana De La Fuente Duran, Brian Bersch, Timothy Bowen, Kenneth Knappenberger, Joshua A. Robinson, "Epitaxial graphene/silicon carbide intercalation: a minireview on graphene modulation and unique 2D materials", *Nanoscale*, **11**, 15440-15447, 2019.

   Zewdu M. Gebeyehu, *et al.* "Photocatalysis-assisted suppression of the graphene nucleation density for CVD growth of graphene," in preparation

Bibliography

[1] A. K. Geim and K. S. Novoselov, “The rise of graphene,” *Nat. Mater.*, vol. 6, pp. 183–191, 2007.

[2] P. R. Wallace, “The band theory of graphite,” *Phys. Rev.*, vol. 71, no. 9, pp. 622–634, May 1947.

[3] J. W. McClure, “Diamagnetism of Graphite,” *Phys. Rev.*, vol. 104, no. 3, pp. 666–671, Nov. 1956.

[4] J. C. Slonczewski and P. R. Weiss, “Band structure of graphite,” *Phys. Rev.*, vol. 109, no. 2, pp. 272–279, Jan. 1958.

[5] H. P. Boehm, R. Setton, and E. Stumpp, “Nomenclature and terminology of graphite intercalation compounds,” *Carbon N. Y.*, vol. 24, no. 2, pp. 241–245, Jan. 1986.

[6] H. P. Boehm, R. Setton, and E. Stumpp, “Nomenclature and terminology of graphite intercalation compounds (IUPAC Recommendations 1994),” *Pure Appl. Chem.*, vol. 66, no. 9, pp. 1893–1901, Jan. 1994.

[7] K. S. Novoselov, A. K. Geim, S. V Morozov, D. Jiang, Y. Zhang, S. V Dubonos, I. V Grigorieva, and A. A. Firsov, “Electric field effect in atomically thin carbon films.,” *Science*, vol. 306, no. 5696, pp. 666–9, Oct. 2004.

[8] K. I. Bolotin, K. J. Sikes, Z. Jiang, M. Klima, G. Fudenberg, J. Hone, P. Kim, and H. L. Stormer, “Ultrahigh electron mobility in suspended graphene,” *Solid State Commun.*, vol. 146, no. 9–10, p. 351, Jun. 2008.

[9] A. H. Castro Neto, F. Guinea, N. M. R. Peres, K. S. Novoselov, and A. K. Geim, “The electronic properties of graphene,” *Rev. Mod. Phys.*, vol. 81, no. 1, pp. 109–162, Jan. 2009.

[10] I.A. Ovid’ko, “Mechanical properties of graphene,” *Rev.Adv.Mater. sci*, vol. 34, pp.

1–11, 2013.

[11] C. Lee, X. Wei, J. W. Kysar, and J. Hone, “Measurement of the elastic properties and intrinsic strength of monolayer graphene,” *Science (80-.).*, vol. 321, no. 5887, pp. 385–388, Jul. 2008.

[12] M. D. Stoller, S. Park, Y. Zhu, J. An, and R. S. Ruoff, “Graphene-based ultracapacitors,” *Nano Lett.*, vol. 8, no. 10, pp. 3498–3502, Oct. 2008.

[13] R. R. Nair, P. Blake, A. N. Grigorenko, K. S. Novoselov, T. J. Booth, T. Stauber, N. M. R. Peres, and A. K. Geim, “Fine structure constant defines visual transparency of graphene,” *Science (80-.).*, vol. 320, p. 1308, 2008.

[14] S. Bae, H. Kim, Y. Lee, X. Xu, J.-S. Park, Y. Zheng, J. Balakrishnan, T. Lei, H. Ri Kim, Y. Il Song, Y.-J. Kim, K. S. Kim, B. Özyilmaz, J.-H. Ahn, B. H. Hong, and S. Iijima, “Roll-to-roll production of 30-inch graphene films for transparent electrodes,” *Nat. Nanotechnol.*, vol. 5, no. 8, pp. 574–578, Aug. 2010.

[15] M. Ruan, Y. Hu, Z. Guo, R. Dong, J. Palmer, J. Hankinson, C. Berger, and W. A. De Heer, “Epitaxial graphene on silicon carbide: Introduction to structured graphene,” *MRS Bull.*, vol. 37, no. 12, pp. 1138–1147, 2012.

[16] Y. Hernandez, V. Nicolosi, M. Lotya, F. M. Blighe, Z. Sun, S. De, I. T. McGovern, B. Holland, M. Byrne, Y. K. Gun’Ko, J. J. Boland, P. Niraj, G. Duesberg, S. Krishnamurthy, R. Goodhue, J. Hutchison, V. Scardaci, A. C. Ferrari, and J. N. Coleman, “High-yield production of graphene by liquid-phase exfoliation of graphite,” *Nat. Nanotechnol.*, vol. 3, no. 9, pp. 563–568, Sep. 2008.

[17] H. C. Lee, W.-W. Liu, S.-P. Chai, A. R. Mohamed, A. Aziz, C.-S. Khe, N. M. S. Hidayah, and U. Hashim, “Review of the synthesis, transfer, characterization and growth mechanisms of single and multilayer graphene,” *RSC Adv.*, vol. 7, p. 15644, 2017.

[18] K. S. Novoselov, V. I. Fal’ko, L. Colombo, P. R. Gellert, M. G. Schwab, and K. Kim, “A roadmap for graphene,” *Nature*, vol. 490, no. 7419, pp. 192–200, Oct. 2012.

[19] P. Blake, P. D. Brimicombe, R. R. Nair, T. J. Booth, D. Jiang, F. Schedin, L. A.

Ponomarenko, S. V. Morozov, H. F. Gleeson, E. W. Hill, A. K. Geim, and K. S. Novoselov, “Graphene-based liquid crystal device,” *Nano Lett.*, vol. 8, no. 6, pp. 1704–1708, Jun. 2008.

[20] S. Stankovich, D. A. Dikin, G. H. B. Dommett, K. M. Kohlhaas, E. J. Zimney, E. A. Stach, R. D. Piner, S. T. Nguyen, and R. S. Ruoff, “Graphene-based composite materials,” *Nature*, vol. 442, no. 7100, pp. 282–286, Jul. 2006.

[21] K. V. Emtsev, A. Bostwick, K. Horn, J. Jobst, G. L. Kellogg, L. Ley, J. L. McChesney, T. Ohta, S. A. Reshanov, J. Röhrl, E. Rotenberg, A. K. Schmid, D. Waldmann, H. B. Weber, and T. Seyller, “Towards wafer-size graphene layers by atmospheric pressure graphitization of silicon carbide,” *Nat. Mater.*, vol. 8, no. 3, pp. 203–207, Mar. 2009.

[22] W. A. De Heer, C. Berger, M. Ruan, M. Sprinkle, X. Li, Y. Hu, B. Zhang, J. Hankinson, and E. Conrad, “Large area and structured epitaxial graphene produced by confinement controlled sublimation of silicon carbide,” *PNAS*, vol. 108, pp. 16900–16905, 2011.

[23] J. Robinson, X. Weng, K. Trumbull, R. Cavalero, M. Wetherington, E. Frantz, M. LaBella, Z. Hughes, M. Fanton, and D. Snyder, “Nucleation of epitaxial graphene on SiC(0001),” *ACS Nano*, vol. 4, no. 1, pp. 153–158, Jan. 2010.

[24] X. Li, W. Cai, J. An, S. Kim, J. Nah, D. Yang, R. Piner, A. Velamakanni, I. Jung, E. Tutuc, S. K. Banerjee, L. Colombo, and R. S. Ruoff, “Large-area synthesis of high-quality and uniform graphene films on copper foils,” *Science.*, vol. 324, no. 5932, pp. 1312–1314, Jun. 2009.

[25] S.-J. Byun, H. Lim, G.-Y. Shin, T.-H. Han, S. H. Oh, J.-H. Ahn, H. C. Choi, and T.-W. Lee, “Graphenes converted from polymers,” *J. Phys. Chem. Lett.*, vol. 2, no. 5, pp. 493–497, Mar. 2011.

[26] B. Zhang, W. H. Lee, R. Piner, I. Kholmanov, Y. Wu, H. Li, H. Ji, and R. S. Ruoff, “Low-temperature chemical vapor deposition growth of graphene from toluene on

electropolished copper foils," *ACS Nano*, vol. 6, no. 3, pp. 2471–2476, Mar. 2012.

[27] G. Ruan, Z. Sun, Z. Peng, and J. M. Tour, "Growth of graphene from food, insects, and waste," *ACS Nano*, vol. 5, no. 9, pp. 7601–7607, Sep. 2011.

[28] Johann Coraux, Alpha T. N'Diaye, A. Carsten Busse, and T. Michely, "Structural coherency of graphene on Ir(111)," *Nano Lett. 2008,* vol. 8, pp. 565–570, 2008.

[29] A. Reina, S. Thiele, X. Jia, S. Bhaviripudi, M. S. Dresselhaus, J. A. Schaefer, and J. Kong, "Growth of large-area single- and Bi-layer graphene by controlled carbon precipitation on polycrystalline Ni surfaces," *Nano Res.*, vol. 2, pp. 509–516, 2009.

[30] T. Fujita, W. Kobayashi, and C. Oshima, "Novel structures of carbon layers on a Pt(111) surface," *Surf. Interface Anal.*, vol. 37, no. 2, pp. 120–123, Feb. 2005.

[31] Q. Yu, J. Lian, S. Siriponglert, H. Li, Y. P. Chen, and S.-S. Pei, "Graphene segregated on Ni surfaces and transferred to insulators," *Appl. Phys. Lett.*, vol. 93, no. 11, p. 113103, Sep. 2008.

[32] A. Reina, X. Jia, J. Ho, D. Nezich, H. Son, V. Bulovic, M. S. Dresselhaus, and J. Kong, "Large area, few-layer graphene films on arbitrary substrates by chemical vapor deposition," *Nano Lett.*, vol. 9, no. 1, pp. 30–35, Jan. 2009.

[33] N. Liu, L. Fu, B. Dai, K. Yan, X. Liu, R. Zhao, Y. Zhang, and Z. Liu, "Universal segregation growth approach to wafer-size graphene from non-noble metals," *Nano Lett.*, vol. 11, no. 1, pp. 297–303, 2011.

[34] R. Addou, A. Dahal, P. Sutter, and M. Batzill, "Monolayer graphene growth on Ni(111) by low temperature chemical vapor deposition," *Appl. Phys. Lett.*, vol. 100, no. 2, pp. 109–112, 2012.

[35] C. Mattevi, H. Kim, and M. Chhowalla, "A review of chemical vapour deposition of graphene on copper," *J. Mater. Chem.*, vol. 21, no. 10, pp. 3324–3334, Feb. 2011.

[36] X. Li, W. Cai, J. An, S. Kim, J. Nah, D. Yang, R. Piner, A. Velamakanni, I. Jung, E. Tutuc, S. K. Banerjee, L. Colombo, and R. S. Ruoff, "Large area synthesis of high

quality and uniform graphene films on copper foils," *Science*, vol. 324, no. 5932, pp. 1312–1314, 2009.

[37] X. Li, W. Cai, L. Colombo, and R. S. Ruoff, "Evolution of graphene growth on Ni and Cu by carbon isotope labeling," *Nano*, vol. 12, no. 1, pp. 4268–72, 2009.

[38] M. H. Ani, M. A. Kamarudin, A. H. Ramlan, E. Ismail, M. S. Sirat, M. A. Mohamed, and M. A. Azam, "A critical review on the contributions of chemical and physical factors toward the nucleation and growth of large-area graphene," *J. Mater. Sci.*, vol. 53, no. 10, pp. 7095–7111, May 2018.

[39] R. Muñoz and C. Gómez-Aleixandre, "Review of CVD synthesis of graphene," *Chem. Vap. Depos.*, vol. 19, no. 10-11–12, pp. 297–322, Dec. 2013.

[40] R. K. A. Bansal, "A text book of fluid mechanics and hydraulic machines." Laxmi Publications Limited: New Delhi, India, p. 607−632, 2005.

[41] I. Vlassiouk, M. Regmi, P. Fulvio, S. Dai, P. Datskos, G. Eres, and S. Smirnov, "Role of hydrogen in chemical vapor deposition growth of large single-crystal graphene," *ACS Nano*, vol. 5, no. 7, pp. 6069–6076, Jul. 2011.

[42] X. Zhang, J. Ning, X. Li, B. Wang, L. Hao, M. Liang, M. Jin, and L. Zhi, "Hydrogen-induced effects on the CVD growth of high-quality graphene structures," *Nanoscale*, vol. 5, no. 18, p. 8363, Aug. 2013.

[43] H.-M. Gao, Libo; Ren, Wencai; Zhao, Jinping; Ma, Lai-Peng; Chen, Zongping; Cheng, "Efficient growth of high-quality graphene films on Cu foils by ambient pressure chemical vapor deposition," *Appl. Phys. Lett.*, vol. 97, no. 18, p. 183109, Nov. 2010.

[44] L. Liu, H. Zhou, R. Cheng, W. J. Yu, Y. Liu, Y. Chen, J. Shaw, X. Zhong, Y. Huang, and X. Duan, "High-yield chemical vapor deposition growth of high-quality large-area AB-stacked bilayer graphene," *ACS Nano*, vol. 6, no. 9, pp. 8241–8249, Sep. 2012.

[45] Q. Yu, L. A. Jauregui, W. Wu, R. Colby, J. Tian, Z. Su, H. Cao, Z. Liu, D. Pandey, D. Wei, T. F. Chung, P. Peng, N. P. Guisinger, E. A. Stach, J. Bao, S.-S. Pei, and Y. P. Chen,

"Control and characterization of individual grains and grain boundaries in graphene grown by chemical vapour deposition," *Nat. Mater.*, vol. 10, no. 6, pp. 443–449, Jun. 2011.

[46] Z. M. Gebeyehu, A. Arrighi, M. V. Costache, C. M. Sotomayor-Torres, M. J. Esplandiu, and S. O. Valenzuela, "Impact of the *in situ* rise in hydrogen partial pressure on graphene shape evolution during CVD growth of graphene," *RSC Adv.*, vol. 8, no. 15, pp. 8234–8239, 2018.

[47] I. Vlassiouk, P. Fulvio, H. Meyer, N. Lavrik, S. Dai, P. Datskos, and S. Smirnov, "Large scale atmospheric pressure chemical vapor deposition of graphene," *Carbon N. Y.*, vol. 54, pp. 58–67, 2013.

[48] O. V. Yazyev and S. G. Louie, "Electronic transport in polycrystalline graphene," *Nat. Mater.*, vol. 9, no. 10, pp. 806–809, Oct. 2010.

[49] Y. Hao, M. S. Bharathi, L. Wang, Y. Liu, H. Chen, S. Nie, X. Wang, H. Chou, C. Tan, B. Fallahazad, H. Ramanarayan, C. W. Magnuson, E. Tutuc, B. I. Yakobson, K. F. McCarty, Y. Zhang, P. Kim, J. Hone, L. Colombo, and R. S. Ruoff, "The role of surface oxygen in the growth of large single-crystal graphene on copper.," *Science*, vol. 342, no. 6159, pp. 720–3, 2013.

[50] X. Li, C. W. Magnuson, A. Venugopal, R. M. Tromp, J. B. Hannon, E. M. Vogel, L. Colombo, and R. S. Ruoff, "Large-area graphene single crystals grown by low-pressure chemical vapor deposition of methane on copper," *J. Am. Chem. Soc.*, vol. 133, no. 9, pp. 2816–2819, 2011.

[51] T. Wu, X. Zhang, Q. Yuan, J. Xue, G. Lu, and Z. Liu, "Fast growth of inch-sized single-crystalline graphene from a controlled single nucleus on Cu–Ni alloys," *Nat. Mater.*, vol. 15, no. 1, pp. 43–47, 2016.

[52] A. T. Murdock, C. D. van Engers, J. Britton, V. Babenko, S. S. Meysami, H. Bishop, A. Crossley, A. A. Koos, and N. Grobert, "Targeted removal of copper foil surface impurities for improved synthesis of CVD graphene," *Carbon N. Y.*, vol. 122, pp.

207–216, Oct. 2017.

[53] Z. Luo, Y. Lu, D. W. Singer, M. E. Berck, L. A. Somers, B. R. Goldsmith, and A. T. C. Johnson, “Effect of substrate roughness and feedstock concentration on growth of wafer-scale graphene at atmospheric pressure,” *Chem. Mater.*, vol. 23, no. 6, pp. 1441–1447, Mar. 2011.

[54] S. Chen, H. Ji, H. Chou, Q. Li, H. Li, J. W. Suk, R. Piner, L. Liao, W. Cai, and R. S. Ruoff, “Millimeter-size single-crystal graphene by suppressing evaporative loss of Cu during low pressure chemical vapor deposition,” *Adv. Mater.*, vol. 25, no. 14, pp. 2062–2065, 2013.

[55] D. R. Gabe, “Toward a universal electropolishing solution,” *Metallography*, vol. 5, no. 5, pp. 415–421, Oct. 1972.

[56] K. L. Chavez and D. W. Hess, “A novel method of etching copper oxide using acetic acid,” *J. Electrochem. Soc.*, vol. 148, no. 11, p. G640, Nov. 2001.

[57] M. P. Levendorf, C. S. Ruiz-Vargas, S. Garg, and J. Park, “Transfer-free batch fabrication of single layer graphene transistors,” *Nano Lett.*, vol. 9, no. 12, pp. 4479–4483, Dec. 2009.

[58] X. Xu, Z. Zhang, J. Dong, D. Yi, J. Niu, M. Wu, L. Lin, R. Yin, M. Li, J. Zhou, S. Wang, J. Sun, X. Duan, P. Gao, Y. Jiang, X. Wu, H. Peng, R. S. Ruoff, Z. Liu, D. Yu, E. Wang, F. Ding, and K. Liu, “Ultrafast epitaxial growth of metre-sized single-crystal graphene on industrial Cu foil,” *Sci. Bull.*, vol. 62, no. 15, p. 1074, Aug. 2017.

[59] L. Zhang, Z. Shi, Y. Wang, R. Yang, D. Shi, and G. Zhang, “Catalyst-free growth of nanographene films on various substrates,” *Nano Res.*, vol. 4, no. 3, pp. 315–321, Mar. 2011.

[60] A. Ismach, C. Druzgalski, S. Penwell, A. Schwartzberg, M. Zheng, A. Javey, J. Bokor, and Y. Zhang, “Direct chemical vapor deposition of graphene on dielectric surfaces,” *Nano Lett.*, vol. 10, no. 5, pp. 1542–1548, May 2010.

[61] Y. Chen, X.-L. Gong, and J.-G. Gai, “Progress and challenges in transfer of large-area

graphene films," *Adv. Sci.*, vol. 3, no. 8, p. 1500343, Aug. 2016.

[62] X. Li, Y. Zhu, W. Cai, M. Borysiak, B. Han, D. Chen, R. D. Piner, L. Colomba, and R. S. Ruoff, "Transfer of large-area graphene films for high-performance transparent conductive electrodes," *Nano Lett.*, vol. 9, no. 12, pp. 4359–4363, 2009.

[63] K. S. Kim, Y. Zhao, H. Jang, S. Y. Lee, J. M. Kim, J.-H. Ahn, P. Kim, J.-Y. Choi, and B. H. Hong, "Large-scale pattern growth of graphene films for stretchable transparent electrodes," *Nature*, vol. 457, no. 7230, pp. 706–710, 2009.

[64] Y. Wang, Y. Zheng, X. Xu, E. Dubuisson, Q. Bao, J. Lu, and K. P. Loh, "Electrochemical delamination of cvd-grown graphene film: toward the recyclable use of copper catalyst," *ACS Nano*, vol. 5, no. 12, pp. 9927–9933, Dec. 2011.

[65] P. Gupta, P. D. Dongare, S. Grover, S. Dubey, H. Mamgain, A. Bhattacharya, and M. M. Deshmukh, "A facile process for soak-and-peel delamination of CVD graphene from substrates using water.," *Sci. Rep.*, vol. 4, p. 3882, Jan. 2014.

[66] K. S. Kim, Y. Zhao, H. Jang, S. Y. Lee, J. M. Kim, K. S. Kim, J.-H. Ahn, P. Kim, J.-Y. Choi, and B. H. Hong, "Large-scale pattern growth of graphene films for stretchable transparent electrodes," *Nature*, vol. 457, no. 7230, pp. 706–710, Feb. 2009.

[67] Z. Chen, X. Ge, H. Zhang, Y. Zhang, Y. Sui, G. Yu, Z. Jin, and X. Liu, "High pressure-assisted transfer of ultraclean chemical vapor deposited graphene," *Appl. Phys. Lett.*, vol. 108, no. 13, p. 132106, Mar. 2016.

[68] L. Banszerus, M. Schmitz, S. Engels, J. Dauber, M. Oellers, F. Haupt, K. Watanabe, T. Taniguchi, B. Beschoten, and C. Stampfer, "Ultrahigh-mobility graphene devices from chemical vapor deposition on reusable copper," *Sci. Adv.*, vol. 1, no. 6, pp. 1–6, Jul. 2015.

[69] P. Blake, E. W. Hill, A. H. Castro Neto, K. S. Novoselov, D. Jiang, R. Yang, T. J. Booth, and A. K. Geim, "Making graphene visible," *Appl. Phys. Lett.*, vol. 91, no. 6, p. 063124, Aug. 2007.

[70] V. C. Tung, M. J. Allen, Y. Yang, and R. B. Kaner, "High-throughput solution

processing of large-scale graphene," *Nat. Nanotechnol.*, vol. 4, no. 1, pp. 25–29, Jan. 2009.

[71] P. Nemes-Incze, Z. Osváth, K. Kamarás, and L. P. Biró, "Anomalies in thickness measurements of graphene and few layer graphite crystals by tapping mode atomic force microscopy," *Carbon N. Y.*, vol. 46, pp. 1435–1442, 2008.

[72] H. Shioyama, "The interactions of two chemical species in the interlayer spacing of graphite," *Synth. Met.*, vol. 114, no. 1, pp. 1–15, Jul. 2000.

[73] C. J. Shearer, A. D. Slattery, A. J. Stapleton, J. G. Shapter, and C. T. Gibson, "Accurate thickness measurement of graphene," *Nanotechnology*, vol. 27, no. 12, p. 125704, Mar. 2016.

[74] P. Cao, K. Xu, J. O. Varghese, and J. R. Heath, "Atomic force microscopy characterization of room-temperature adlayers of small organic molecules through graphene templating," *J. Am. Chem. Soc.*, vol. 133, no. 8, pp. 2334–2337, Mar. 2011.

[75] O. Ochedowski, B. K. Bussmann, and M. Schleberger, "Graphene on mica - intercalated water trapped for life.," *Sci. Rep.*, vol. 4, p. 6003, Aug. 2014.

[76] A. C. Ferrari and D. M. Basko, "Raman spectroscopy as a versatile tool for studying the properties of graphene," *Nat. Nanotechnol.*, vol. 8, no. 4, pp. 235–246, Apr. 2013.

[77] R. Saito, M. Hofmann, G. Dresselhaus, A. Jorio, and M. S. Dresselhaus, "Raman spectroscopy of graphene and carbon nanotubes," *Adv. Phys.*, vol. 60, no. 3, pp. 413–550, Jun. 2011.

[78] P. Ikonen, C. Simovski, S. Tretyakov, P. Belov, and Y. Hao, "Magnification of subwavelength field distributions at microwave frequencies using a wire medium slab operating in the canalization regime," *Appl. Phys. Lett.*, vol. 91, no. 10, p. 104102, Sep. 2007.

[79] Y. Liu, Z. Liu, W. Lew, and Q. Wang, "Temperature dependence of the electrical

transport properties in few-layer graphene interconnects," *Nanoscale Res. Lett.*, vol. 8, no. 1, p. 335, Jul. 2013.

[80] A. H. Castro Neto, F. Guinea, N. M. R. Peres, K. S. Novoselov, and A. K. Geim, "The electronic properties of graphene," *Rev. Mod. Phys.*, vol. 81, no. 1, p. 109, Jan. 2009.

[81] J.-H. Chen, C. Jang, S. Xiao, M. Ishigami, and M. S. Fuhrer, "Intrinsic and extrinsic performance limits of graphene devices on SiO_2," *Nat. Nanotechnol. 2008 34*, vol. 3, no. 4, p. 206, Mar. 2008.

[82] K. S. Novoselov, V. I. Fal'ko, L. Colombo, P. R. Gellert, M. G. Schwab, and K. Kim, "A roadmap for graphene," *Nature*, vol. 490, no. 7419, pp. 192–200, 2012.

[83] F. Chen, J. Xia, D. K. Ferry, and N. Tao, "Dielectric screening enhanced performance in graphene FET," *Nano Lett.*, vol. 9, no. 7, p. 2571, Jul. 2009.

[84] L. Banszerus, T. Sohier, A. Epping, F. Winkler, F. Libisch, F. Haupt, K. Watanabe, T. Taniguchi, K. Müller-Caspary, N. Marzari, F. Mauri, B. Beschoten, and C. Stampfer, "Extraordinary high room-temperature carrier mobility in graphene-WSe$_2$ heterostructures," *arXiv:1909.09523*, Sep. 2019.

[85] Y.-C. Lin, C.-C. Lu, C.-H. Yeh, C. Jin, K. Suenaga, and P.-W. Chiu, "Graphene annealing: how clean can it be?," *Nano Lett.*, vol. 12, no. 1, pp. 414–419, Jan. 2012.

[86] J. Moser, A. Barreiro, and A. Bachtold, "Current-induced cleaning of graphene," *Appl. Phys. Lett.*, vol. 91, no. 16, p. 163513, Oct. 2007.

[87] S. Fratini and F. Guinea, "Substrate-limited electron dynamics in graphene," *Phys. Rev. B*, vol. 77, no. 19, p. 195415, May 2008.

[88] M. I. Katsnelson and A. K. Geim, "Electron scattering on microscopic corrugations in graphene," *Philos. Trans. R. Soc. A Math. Phys. Eng. Sci.*, vol. 366, no. 1863, pp. 195–204, Jan. 2008.

[89] C. R. Dean, A. F. Young, I. Meric, C. Lee, L. Wang, S. Sorgenfrei, K. Watanabe, T. Taniguchi, P. Kim, K. L. Shepard, and J. Hone, “Boron nitride substrates for high-quality graphene electronics,” *Nat. Nanotechnol.*, vol. 5, pp. 722–726, 2010.

[90] K. Watanabe, T. Taniguchi, and H. Kanda, “Direct-bandgap properties and evidence for ultraviolet lasing of hexagonal boron nitride single crystal,” *Nat. Mater.*, vol. 3, no. 6, pp. 404–409, Jun. 2004.

[91] G. Giovannetti, P. A. Khomyakov, G. Brocks, P. J. Kelly, and J. van den Brink, “Substrate-induced band gap in graphene on hexagonal boron nitride: *Ab initio* density functional calculations,” *Phys. Rev. B*, vol. 76, no. 7, p. 073103, Aug. 2007.

[92] N. Petrone, C. R. Dean, I. Meric, A. M. van der Zande, P. Y. Huang, L. Wang, D. Muller, K. L. Shepard, and J. Hone, “Chemical vapor deposition-derived graphene with electrical performance of exfoliated graphene,” *Nano Lett.*, vol. 12, no. 6, pp. 2751–2756, Jun. 2012.

[93] I. Žutić, J. Fabian, and S. Das Sarma, “Spintronics: Fundamentals and applications,” *Rev. Mod. Phys.*, vol. 76, no. 2, pp. 323–410, Apr. 2004.

[94] S. Datta and B. Das, “Electronic analog of the electro-optic modulator,” *Appl. Phys. Lett.*, vol. 56, no. 7, pp. 665–667, Feb. 1990.

[95] G. Binasch, P. Grünberg, F. Saurenbach, and W. Zinn, “Enhanced magnetoresistance in layered magnetic structures with antiferromagnetic interlayer exchange,” *Phys. Rev. B*, vol. 39, no. 7, pp. 4828–4830, Mar. 1989.

[96] F. J. Jedema, A. T. Filip, and B. J. van Wees, “Electrical spin injection and accumulation at room temperature in an all-metal mesoscopic spin valve,” *Nature*, vol. 410, no. 6826, pp. 345–348, Mar. 2001.

[97] T. Kimura and Y. Otani, “Large spin accumulation in a permalloy-silver lateral spin valve,” *Phys. Rev. Lett.*, vol. 99, no. 19, p. 196604, Nov. 2007.

[98] W. Han, R. K. Kawakami, M. Gmitra, and J. Fabian, “Graphene spintronics,” *Nat. Nanotechnol.*, vol. 9, no. 10, p. 794, Oct. 2014.

[99] D. Van Tuan, F. Ortmann, D. Soriano, S. O. Valenzuela, and S. Roche, “Pseudospin-driven spin relaxation mechanism in graphene,” *Nat. Phys.*, vol. 10, no. 11, p. 857, Nov. 2014.

[100] P. J. Zomer, M. H. D. Guimarães, N. Tombros, and B. J. van Wees, “Long-distance spin transport in high-mobility graphene on hexagonal boron nitride,” *Phys. Rev. B*, vol. 86, no. 16, p. 161416, Oct. 2012.

[101] D. Pesin and A. H. MacDonald, “Spintronics and pseudospintronics in graphene and topological insulators,” *Nat. Mater.*, vol. 11, no. 5, pp. 409–416, May 2012.

[102] M. Popinciuc, C. Józsa, P. J. Zomer, N. Tombros, A. Veligura, H. T. Jonkman, and B. J. van Wees, “Electronic spin transport in graphene field-effect transistors,” *Phys. Rev. B*, vol. 80, no. 21, p. 214427, Dec. 2009.

[103] W. Han, K. Pi, W. Bao, K. M. McCreary, Y. Li, W. H. Wang, C. N. Lau, and R. K. Kawakami, “Electrical detection of spin precession in single layer graphene spin valves with transparent contacts,” *Appl. Phys. Lett.*, vol. 94, no. 22, p. 222109, Jun. 2009.

[104] W. Han, K. Pi, K. M. McCreary, Y. Li, J. J. I. Wong, A. G. Swartz, and R. K. Kawakami, “Tunneling spin injection into single layer graphene,” *Phys. Rev. Lett.*, vol. 105, no. 16, p. 167202, Oct. 2010.

[105] W. Han, R. K. Kawakami, M. Gmitra, and J. Fabian, “Graphene spintronics,” *Nat. Nanotechnol.*, vol. 9, no. 10, pp. 794–807, Oct. 2014.

[106] R. J. Elliott, “Theory of the effect of spin-orbit coupling on magnetic resonance in some semiconductors,” *Phys. Rev.*, vol. 96, no. 2, pp. 266–279, Oct. 1954.

[107] M. I. D’yakonov and V. I. Perel’, “Spin orientation of electrons associated with the interband absorption of light in semiconductors,” *J. Exp. Theor. Phys.*, vol. 33, no. 5, pp. 1053–1059, 1971.

[108] J. Seo, J. Lee, A.-R. Jang, Y. Choi, U. Kim, H. S. Shin, and H. Park, “Study of cooling rate on the growth of graphene via chemical vapor deposition,” *Chem. Mater.*, vol.

29, no. 10, p. 4202, May 2017.

[109] W. Regan, N. Alem, B. Alemán, B. Geng, Ç. Girit, L. Maserati, F. Wang, M. Crommie, and A. Zettl, “A direct transfer of layer-area graphene,” *Appl. Phys. Lett.*, vol. 96, no. 11, p. 113102, Mar. 2010.

[110] H. Wang, G. Wang, P. Bao, S. Yang, W. Zhu, X. Xie, and W.-J. Zhang, “Controllable synthesis of submillimeter single-crystal monolayer graphene domains on copper foils by suppressing nucleation,” *J. Am. Chem. Soc.*, vol. 134, no. 8, pp. 3627–3630, Feb. 2012.

[111] B. Wu, D. Geng, Y. Guo, L. Huang, Y. Xue, J. Zheng, J. Chen, G. Yu, Y. Liu, L. Jiang, and W. Hu, “Equiangular hexagon-shape-controlled synthesis of graphene on copper surface,” *Adv. Mater.*, vol. 23, no. 31, pp. 3522–3525, Aug. 2011.

[112] A. W. Robertson and J. H. Warner, “Hexagonal single crystal domains of few-layer graphene on copper foils,” *Nano Lett.*, vol. 11, no. 3, pp. 1182–1189, Mar. 2011.

[113] S. Bhaviripudi, X. Jia, M. S. Dresselhaus, and J. Kong, “Role of kinetic factors in chemical vapor graphene using copper catalyst,” *Nano Lett.*, vol. 10, pp. 4128–4133, 2010.

[114] X. Zhang, J. Ning, X. Li, B. Wang, L. Hao, M. Liang, M. Jin, and L. Zhi, “Hydrogen-induced effects on the CVD growth of high-quality graphene structures.,” *Nanoscale*, vol. 5, no. 18, pp. 8363–6, 2013.

[115] I. Vlassiouk, M. Regmi, P. Fulvio, S. Dai, P. Datskos, G. Eres, and S. Smirnov, “Role of hydrogen in chemical vapor deposition growth of large single-crystal graphene,” *ACS Nano*, vol. 5, no. 7, pp. 6069–6076, 2011.

[116] E. Meca, J. Lowengrub, H. Kim, C. Mattevi, and V. B. Shenoy, “Epitaxial graphene growth and shape dynamics on copper: phase- field modeling and experiments,” *Nano Lett.*, vol. 13, p. 5692−5697, 2013.

[117] W. Fei, J. Yin, X. Liu, and W. Guo, “Dendritic graphene domains: Growth, morphology and oxidation promotion,” *Mater. Lett.*, vol. 110, pp. 225–228, 2013.

[118] Y. Zhang, L. Zhang, P. Kim, M. Ge, Z. Li, and C. Zhou, “Vapor trapping growth of single-crystalline graphene flowers: Synthesis, morphology, and electronic properties,” *Nano Lett.*, vol. 12, no. 6, pp. 2810–2816, 2012.

[119] D. Geng, B. Wu, Y. Guo, B. Luo, Y. Xue, J. Chen, G. Yu, and Y. Liu, “Fractal etching of graphene,” *J. Am. Chem. Soc.*, vol. 135, no. 17, pp. 6431–6434, 2013.

[120] A. Thangaraja, S. M. Shinde, G. Kalita, R. Papon, S. Sharma, R. Vishwakarma, K. P. Sharma, M. Tanemura, A. Thangaraja, S. M. Shinde, G. Kalita, and R. Papon, “Structure dependent hydrogen induced etching features of graphene crystals Structure,” *Appl. Phys. Lett.*, vol. 106, no. 2015, p. 253106, 2016.

[121] W. Guo, F. Jing, J. Xiao, C. Zhou, Y. Lin, and S. Wang, “Oxidative-etching-assisted synthesis of centimeter-sized single-crystalline graphene,” *Adv. Mater.*, vol. 28, no. 16, pp. 3152–3158, 2016.

[122] B. Luo, E. Gao, D. Geng, H. Wang, Z. Xu, and G. Yu, “Etching-controlled growth of graphene by chemical vapor deposition,” *Chem. Mater.*, vol. 29, p. 1022−1027, 2017.

[123] S. Chaitoglou, E. Pascual, E. Bertran, and J. L. Andujar, “Effect of a balanced concentration of hydrogen on graphene CVD growth,” *J. Nanomater.*, no. 1, 2016.

[124] X. Wang, S. M. Tabakman, and H. Dai, “Atomic layer deposition of metal oxides on pristine and functionalized graphene,” *Jacs*, vol. 130, no, pp. 8152–8153, 2008.

[125] Y. Zhang, Z. Li, P. Kim, L. Zhang, and C. Zhou, “Anisotropic hydrogen etching of chemical vapor deposited graphene,” *ACS Nano*, vol. 6, no. 1, pp. 126–132, 2012.

[126] J. Li, D. Wang, and L.-J. Wan, “Unexpected functions of oxygen in a chemical vapor deposition atmosphere to regulate graphene growth modes,” *Chem. Commun.*, vol. 51, no. 85, pp. 15486–15489, 2015.

[127] K. M. Subhedar, I. Sharma, and S. R. Dhakate, “Control of layer stacking in CVD graphene under quasi-static condition,” *Phys. Chem. Chem. Phys.*, vol. 17, pp. 22304–22310, 2015.

[128] C.-C. Chen, C.-J. Kuo, C.-D. Liao, C.-F. Chang, C.-A. Tseng, C.-R. Liu, and Y.-T. Chen, “Growth of lage-area graphene single crystals in confined reaction space with diffusion-driven chemical vapor deposition,” *Chem. Mater.*, vol. 27, no. 18, pp. 6249–6258, 2015.

[129] T. O. Wehling, A. I. Lichtenstein, and M. I. Katsnelson, “First-principles studies of water adsorption on graphene: The role of the substrate,” *Appl. Phys. Lett.*, vol. 93, no. 20, p. 202110, Nov. 2008.

[130] X. Li, W. Cai, J. An, S. Kim, J. Nah, D. Yang, R. Piner, A. Velamakanni, I. Jung, E. Tutuc, S. K. Banerjee, L. Colombo, and R. S. Ruoff, “Large-area synthesis of high-quality and uniform graphene films on copper foils.,” *Science (80-.).*, vol. 324, no. 5932, pp. 1312–1314, 2009.

[131] F. H. L. Koppens, T. Mueller, P. Avouris, A. C. Ferrari, M. S. Vitiello, and M. Polini, “Photodetectors based on graphene, other two-dimensional materials and hybrid systems,” *Nat. Nanotechnol.*, vol. 9, no. 10, pp. 780–793, 2014.

[132] A. H. Castro Neto, F. Guinea, N. M. R. Peres, K. S. Novoselov, and A. K. Geim, “The electronic properties of graphene,” *Rev. Mod. Phys.*, vol. 81, no. 1, pp. 109–162, 2009.

[133] S. Bae, H. K. Kim, Y. Lee, X. Xu, J.-S. Park, Y. Zheng, J. Balakrishnan, D. Im, T. Lei, Y. Il Song, Y. J. Kim, K. S. Kim, B. Özyilmaz, J.-H. Ahn, B. H. Hong, and S. Iijima, “30 inch roll-based production of high-quality graphene films for flexible transparent electrodes,” vol. 5, no. June, pp. 1–5, 2009.

[134] C.-M. Seah, S.-P. Chai, and A. R. Mohamed, “Mechanisms of graphene growth by chemical vapour deposition on transition metals,” *Carbon N. Y.*, vol. 70, pp. 1–21, 2014.

[135] O. V Yazyev and S. G. Louie, “Electronic transport in polycrystalline graphene.,” *Nat. Mater.*, vol. 9, no. 10, pp. 806–809, 2010.

[136] J. Červenka and C. F. J. Flipse, “Structural and electronic properties of grain

boundaries in graphite: Planes of periodically distributed point defects," *Phys. Rev. B - Condens. Matter Mater. Phys.*, vol. 79, no. 19, pp. 1–5, 2009.

[137] Q. Yu, L. A. Jauregui, W. Wu, R. Colby, J. Tian, Z. Su, H. Cao, Z. Liu, D. Pandey, D. Wei, T. F. Chung, P. Peng, N. P. Guisinger, E. A. Stach, J. Bao, S. S. Pei, and Y. P. Chen, "Control and characterization of individual grains and grain boundaries in graphene grown by chemical vapour deposition," *Nat Mater*, vol. 10, no. 6, pp. 443–449, 2011.

[138] R. Grantab, V. B. Shenoy, and R. S. Ruoff, "Anomalous strength characteristics of tilt grain boundaries in graphene," *Science (80-.).*, vol. 330, no. 6006, pp. 946–948, 2010.

[139] S. Nie, J. M. Wofford, N. C. Bartelt, O. D. Dubon, and K. F. McCarty, "Origin of the mosaicity in graphene grown on Cu(111)," *Phys. Rev. B*, vol. 84, no. 15, p. 155425, Oct. 2011.

[140] M. H. Griep, E. Sandoz-Rosado, T. M. Tumlin, and E. Wetzel, "Enhanced graphene mechanical properties through ultrasmooth copper growth substrates," *Nano Lett.*, vol. 16, no. 3, pp. 1657–1662, Mar. 2016.

[141] G. H. Han, F. Güneş, J. J. Bae, E. S. Kim, S. J. Chae, H.-J. Shin, J.-Y. Choi, D. Pribat, and Y. H. Lee, "Influence of copper morphology in forming nucleation seeds for graphene growth," *Nano Lett.*, vol. 11, no. 10, pp. 4144–4148, Oct. 2011.

[142] X. Li, C. W. Magnuson, A. Venugopal, R. M. Tromp, J. B. Hannon, E. M. Vogel, L. Colombo, and R. S. Ruo, "Large-area graphene single crystals grown by low-pressure."

[143] H. Zhou, W. J. Yu, L. Liu, R. Cheng, Y. Chen, X. Huang, Y. Liu, Y. Wang, Y. Huang, and X. Duan, "Chemical vapour deposition growth of large single crystals of monolayer and bilayer graphene.," *Nat. Commun.*, vol. 4, p. 2096, 2013.

[144] Z. Yan, J. Lin, Z. Peng, Z. Sun, Y. Zhu, L. Li, C. Xiang, E. L. Samuel, C. Kittrell, and J. M. Tour, "Toward the synthesis of wafer-scale single-crystal graphene on copper

foils," *ACS Nano*, vol. 6, no. 10, pp. 9110–9117, 2012.

[145] L. Lin, J. Li, H. Ren, A. L. Koh, N. Kang, H. Peng, H. Q. Xu, and Z. Liu, "Surface engineering of copper foils for growing centimeter-sized single-crystalline graphene," *ACS Nano*, vol. 10, no. 2, pp. 2922–2929, 2016.

[146] C. C. Chen, C. J. Kuo, C. Da Liao, C. F. Chang, C. A. Tseng, C. R. Liu, and Y. T. Chen, "Growth of lage-area graphene single crystals in confined reaction space with diffusion-driven chemical vapor deposition," *Chem. Mater.*, vol. 27, no. 18, pp. 6249–6258, 2015.

[147] P. Ghosh, S. Kumar, G. Ramalingam, V. Kochat, M. Radhakrishnan, S. Dhar, S. Suwas, A. Ghosh, N. Ravishankar, and S. Raghavan, "Insights on defect-mediated heterogeneous nucleation of graphene on copper," *J. Phys. Chem. C*, vol. 119, no. 5, pp. 2513–2522, Feb. 2015.

[148] A. T. Murdock, C. D. van Engers, J. Britton, V. Babenko, S. S. Meysami, H. Bishop, A. Crossley, A. A. Koos, and N. Grobert, "Targeted removal of copper foil surface impurities for improved synthesis of CVD graphene," *Carbon N. Y.*, vol. 122, pp. 207–216, 2017.

[149] M. Abdel Rafea and N. Roushdy, "Determination of the optical band gap for amorphous and nanocrystalline copper oxide thin films prepared by SILAR technique," *J. Phys. D. Appl. Phys.*, vol. 42, no. 1, p. 015413, Jan. 2009.

[150] P. E. de Jongh, D. Vanmaekelbergh, and J. J. Kelly, "Cu2O: a catalyst for the photochemical decomposition of water?," *Chem. Commun.*, no. 12, pp. 1069–1070, Jan. 1999.

[151] M. Singh, D. Jampaiah, A. E. Kandjani, Y. M. Sabri, E. Della Gaspera, P. Reineck, M. Judd, J. Langley, N. Cox, J. van Embden, E. L. H. Mayes, B. C. Gibson, S. K. Bhargava, R. Ramanathan, and V. Bansal, "Oxygen-deficient photostable Cu_2O for enhanced visible light photocatalytic activity," *Nanoscale*, vol. 10, no. 13, pp. 6039–6050, Mar. 2018.

[152] C. W. Magnuson, X. Kong, H. Ji, C. Tan, H. Li, R. Piner, C. A. Ventrice, and R. S. Ruoff, “Copper oxide as a ‘self-cleaning’ substrate for graphene growth,” *J. Mater. Res.*, vol. 29, no. 03, pp. 403–409, 2014.

[153] M. Taborelli, “"Cleaning and surface properties, Techical Report,” 2006.

[154] J. Kraus, L. Böbel, G. Zwaschka, and S. Günther, “Understanding the reaction kinetics to optimize graphene growth on Cu by chemical vapor deposition,” *Ann. Phys.*, vol. 1700029, pp. 1–16, 2017.

[155] S. G. Jürgen Kraus, Magdalene Bobel, “Suppressing graphene nucleation during CVD on polycrystalline Cu by controlling the carbon content of the support foils,” *Carbon N. Y.*, vol. 96, pp. 153–165, 2016.

[156] P. Sutter, J. T. Sadowski, and E. Sutter, “Graphene on Pt(111): Growth and substrate interaction,” *Phys. Rev. B*, vol. 80, no. 24, p. 245411, Dec. 2009.

[157] S. Roche, J. Åkerman, B. Beschoten, J.-C. Charlier, M. Chshiev, S. Prasad Dash, B. Dlubak, J. Fabian, A. Fert, M. Guimarães, F. Guinea, I. Grigorieva, C. Schönenberger, P. Seneor, C. Stampfer, S. O. Valenzuela, X. Waintal, and B. van Wees, “Graphene spintronics: the european flagship perspective,” *2D Mater.*, vol. 2, no. 3, p. 030202, Jul. 2015.

[158] D. Sander, S. O. Valenzuela, D. Makarov, C. H. Marrows, E. E. Fullerton, P. Fischer, J. McCord, P. Vavassori, S. Mangin, P. Pirro, B. Hillebrands, A. D. Kent, T. Jungwirth, O. Gutfleisch, C. G. Kim, and A. Berger, “The 2017 magnetism roadmap,” *J. Phys. D. Appl. Phys.*, vol. 50, no. 36, p. 363001, Sep. 2017.

[159] A. Avsar, T.-Y. Yang, S. Bae, J. Balakrishnan, F. Volmer, M. Jaiswal, Z. Yi, S. R. Ali, G. Güntherodt, B. H. Hong, B. Beschoten, and B. Özyilmaz, “Toward wafer scale fabrication of graphene based spin valve devices,” *Nano Lett.*, vol. 11, no. 6, p. 2363, Jun. 2011.

[160] M. V. Kamalakar, C. Groenveld, A. Dankert, and S. P. Dash, “Long distance spin communication in chemical vapour deposited graphene,” *Nat. Commun.*, vol. 6,

no. 1, p. 6766, Dec. 2015.

[161] K. Verguts, Y. Defossez, A. Leonhardt, J. De Messemaeker, K. Schouteden, C. Van Haesendonck, C. Huyghebaert, S. De Gendt, and S. Brems, “Growth of millimeter-sized graphene single crystals on Al2O3 (0001)/Pt(111) template wafers using chemical vapor deposition,” *ECS J. Solid State Sci. Technol.*, vol. 7, no. 12, p. M195, Dec. 2018.

[162] X. Lin, L. Su, Z. Si, Y. Zhang, A. Bournel, Y. Zhang, J.-O. Klein, A. Fert, and W. Zhao, “Gate-driven pure spin current in graphene,” *Phys. Rev. Appl.*, vol. 8, no. 3, p. 034006, Sep. 2017.

[163] Y. Wang, Y. Zheng, X. Xu, E. Dubuisson, Q. Bao, J. Lu, and K. P. Loh, “Electrochemical delamination of cvd-grown graphene film: Toward the recyclable use of copper catalyst,” *ACS Nano*, vol. 5, no. 12, p. 9927, Dec. 2011.

[164] K. Verguts, K. Schouteden, C.-H. Wu, L. Peters, N. Vrancken, X. Wu, Z. Li, M. Erkens, C. Porret, C. Huyghebaert, C. Van Haesendonck, S. De Gendt, and S. Brems, “Controlling water intercalation is key to a direct graphene transfer,” *ACS Appl. Mater. Interfaces*, vol. 9, no. 42, p. 37484, Oct. 2017.

[165] J. F. Sierra, I. Neumann, J. Cuppens, B. Raes, M. V. Costache, and S. O. Valenzuela, “Thermoelectric spin voltage in graphene,” *Nat. Nanotechnol.*, vol. 13, no. 2, p. 107, Feb. 2018.

[166] W. Savero Torres, J. F. Sierra, L. A. Benítez, F. Bonell, M. V Costache, and S. O. Valenzuela, “Spin precession and spin Hall effect in monolayer graphene/Pt nanostructures,” *2D Mater.*, vol. 4, no. 4, p. 041008, Sep. 2017.

[167] F. Xia, V. Perebeinos, Y. Lin, Y. Wu, and P. Avouris, “The origins and limits of metal–graphene junction resistance,” *Nat. Nanotechnol.*, vol. 6, no. 3, p. 179, Mar. 2011.

[168] N. Tombros, C. Jozsa, M. Popinciuc, H. T. Jonkman, and B. J. van Wees, “Electronic spin transport and spin precession in single graphene layers at room temperature,” *Nature*, vol. 448, no. 7153, p. 571, Aug. 2007.

[169] M. Drögeler, C. Franzen, F. Volmer, T. Pohlmann, L. Banszerus, M. Wolter, K. Watanabe, T. Taniguchi, C. Stampfer, and B. Beschoten, “Spin lifetimes exceeding 12 ns in graphene nonlocal spin valve devices,” *Nano Lett.*, vol. 16, no. 6, p. 3533, Jun. 2016.

[170] B. Raes, J. E. Scheerder, M. V. Costache, F. Bonell, J. F. Sierra, J. Cuppens, J. Van de Vondel, and S. O. Valenzuela, “Determination of the spin-lifetime anisotropy in graphene using oblique spin precession,” *Nat. Commun.*, vol. 7, no. 1, p. 11444, Dec. 2016.

[171] W. Han, K. Pi, K. M. Mccreary, Y. Li, J. J. I. Wong, A. G. Swartz, and R. K. Kawakami, “Tunneling spin injection into single layer graphene,” *Phys Rev Lett.*, vol. 105, no. 16, p. 167202, 2010.

[172] T. Zhu and R. K. Kawakami, “Modeling the oblique spin precession in lateral spin valves for accurate determination of the spin lifetime anisotropy: Effect of finite contact resistance and channel length,” *Phys. Rev. B*, vol. 97, no. 14, p. 144413, Apr. 2018.

[173] B. Raes, A. W. Cummings, F. Bonell, M. V. Costache, J. F. Sierra, S. Roche, and S. O. Valenzuela, “Spin precession in anisotropic media,” *Phys. Rev. B*, vol. 95, no. 8, p. 085403, Feb. 2017.

[174] T. Maassen, I. J. Vera-Marun, M. H. D. Guimarães, and B. J. Van Wees, “Contact-induced spin relaxation in hanle spin precession measurements,” *Phys. Rev. B*, vol. 86, no. 23, p. 235408, 2012.

[175] M. Gurram, S. Omar, and B. J. van Wees, “Bias induced up to 100% spin-injection and detection polarizations in ferromagnet/bilayer-hBN/graphene/hBN heterostructures,” *Nat. Commun.*, vol. 8, no. 1, p. 248, Dec. 2017.

[176] M. V. Kamalakar, A. Dankert, P. J. Kelly, and S. P. Dash, “Inversion of spin signal and spin filtering in ferromagnet|hexagonal boron nitride-graphene van der waals heterostructures,” *Sci. Rep.*, vol. 6, no. 1, p. 21168, Aug. 2016.

[177] I. Neumann, M. V. Costache, G. Bridoux, J. F. Sierra, and S. O. Valenzuela, “Enhanced spin accumulation at room temperature in graphene spin valves with amorphous carbon interfacial layers,” *Appl. Phys. Lett.*, vol. 103, no. 11, p. 112401, Sep. 2013.

[178] S. Singh, J. Katoch, T. Zhu, R. J. Wu, A. S. Ahmed, W. Amamou, D. Wang, K. A. Mkhoyan, and R. K. Kawakami, “Strontium oxide tunnel barriers for high quality spin transport and large apin accumulation in graphene,” *Nano Lett.*, vol. 17, no. 12, p. 7578, Dec. 2017.

[179] D. Kochan, M. Gmitra, and J. Fabian, “Spin relaxation mechanism in graphene: resonant scattering by magnetic impurities,” *Phys. Rev. Lett.*, vol. 112, no. 11, p. 116602, Mar. 2014.

[180] D. Soriano, D. Van Tuan, S. M.-M. Dubois, M. Gmitra, A. W. Cummings, D. Kochan, F. Ortmann, J.-C. Charlier, J. Fabian, and S. Roche, “Spin transport in hydrogenated graphene,” *2D Mater.*, vol. 2, no. 2, p. 022002, May 2015.

[181] D. Van Tuan, F. Ortmann, A. W. Cummings, D. Soriano, and S. Roche, “Spin dynamics and relaxation in graphene dictated by electron-hole puddles,” *Sci. Rep.*, vol. 6, no. January, p. 1, 2016.

[182] J. Wang and C. Binek, “Dispersion of electric-field-induced Faraday effect in magnetoelectric Cr2O3,” *Phys. Rev. Appl.*, vol. 5, no. 3, p. 031001, Mar. 2016.

[183] H. W. Hanan Dery, B. Ciftcioglu, M. Huang, Y. Song, R. Kawakami, J. Shi, I. Krivorotov, and I. Ž. and L. J. Sham, “Nanospintronics based on magnetologic gates,” *IEEE Trans. Electron Devices*, vol. 59, no. 1, p. 259, 2012.